Optimization and Analysis of UAV Wing for Medical Delivery

Douglas Rodriguez

Master Dissertation

FEUP Supervisor:

Prof. Dr. Volnei Tita

Prof. Dr. Carolina Silva

Prof. Dr. Federico Danzi

U.PORTO
FEUP FACULDADE DE ENGENHARIA
UNIVERSIDADE DO PORTO

Master in Mechanical Engineering

July/2023

To my mother, who spared no effort in supporting me throughout this journey, I am forever grateful for your unwavering love and dedication.

Optimization and Analysis of UAV Wing for Medical Delivery

Abstract

This work was conducted within the context of developing a fixed-wing UAV for item delivery in challenging terrain locations in Asia. The scope of the work involved the complete development of a first aircraft (prototype), comprising a succinct overview of the sizing process, design, manufacturing, and flight tests. The insights gained from this initial aircraft development proved invaluable for producing a more optimized final product. Consequently, the final aircraft is expected to perform its task with greater efficiency, improved endurance, and increased payload capacity.

In the context of weight efficiency optimization, the focus of this work lies in the development and application of a highly customizable computational tool. The objective of this tool is to minimize the structural weight of the composite material wing for the second aircraft (Medical UAV). The tool was built around a tailored genetic algorithm, designed to explore the search space, while the constraints were based on the Tsai-Hill failure index. To incorporate these constraints, a surrogate model was created, integrating ABAQUS finite element software with Python. The surrogate model utilized the Latin Hypercube sampling technique to generate the training set and employed the Gaussian process to establish the regression model. This enabled the evaluation part of the genetic algorithm to predict failure through the regression model. A significant advantage of the developed computational tool is its high customizability. It allows for flexibility in choosing the type of composite failure analysis and ply orientations. Furthermore, the tool facilitates the easy inclusion of constraints to the optimization problem, enhancing its versatility and applicability.

After completing the development of the computational tool, it was applied to the carbon fiber reinforced plastic wing of the second aircraft. The optimization process was carried out separately for the structural elements. The optimization started with the skins in four different sections, followed by the spars in four independent sections, and finally, the ribs in two different sections. Once the optimization for one of the load cases from the aircraft's V-n diagram was completed, all the obtained layups were integrated into a final finite element model. Through this process, it was ensured that no composite failure occurred, as indicated by the Tsai-Hill failure index, and an optimal weight-efficient layup was obtained for the wing of the Medical UAV, considering the studied load case. Moreover, the successful application of the developed computational tool validates its effectiveness for future analyses and optimization tasks.

Acknowledgements

First, I would like to express my sincere gratitude to Prof. Dr. Volnei Tita for his invaluable guidance, unwavering support, and expert knowledge, which he imparted in a clear and didactic manner, and for his continuous availability throughout the master's thesis and the UAV projects.

I wish to extend my sincere thanks to Prof. Dr. Carolina Silva and Prof. Dr. Federico Danzi for their invaluable contributions and insights throughout this work and the UAV projects. Their expertise, teaching approach, and willingness to share knowledge have significantly enriched this endeavor. The successful development of this work is indebted to their guidance, support, and availability in introducing new ideas and helping to overcome challenges.

I extend my gratitude to Prof. Dr. Pedro Aguiar and the SYSTEC Lab, where the entire Medical UAV project is hosted. Professor Aguiar managed to provide all the encouragement and resources necessary for the creation of a space in FEUP that is capable of developing many types of UAVs.

I would like to express my appreciation to Anuj Regmi, who included me in the UAV project, where I acquire invaluable knowledge and experience. Additionally, the Medical UAV project in the SYSTEC Lab which was extended in this work.

I extend my heartfelt gratitude to my colleague and partner in the Medical UAV project, Dilki Dias, for her unwavering commitment, dedication, and exceptional insights that have been instrumental to the triumph of this UAV project. Without her active participation and contributions across all facets, achieving this project's success would have been an insurmountable task. I am genuinely thankful for her steadfast support and partnership throughout this remarkable journey.

A special acknowledgment for Prof. Dr. Pedro Gamboa and colleagues from University of Beira Interior for assisting with expert knowledge, manufacturing process and the flight testing.

I would like to extend my gratitude to my family in Brazil and the friends I made in Portugal, who have become an extension of my family here. I am deeply thankful to my uncle Gelson for his valuable insights and expertise in parts design throughout my academic journey.

Finally, I am grateful to my mother and my deceased father for their unwavering dedication in providing essential support at every stage of my life. Their boundless efforts have made it possible for me to reach this significant milestone, and I am deeply thankful for their love and guidance.

This work was financially supported by: Base (UIDB/00147/2020) and Programmatic (UIDP/00147/2020) funding of the SYSTEC – Center for Systems and Technologies; ARISE - Associate Laboratory Advanced Production and Intelligent Systems (LA/P/0112/2020), both funded by national funds through the FCT/MCTES (PIDDAC) and DynamiCITY: Fostering Dynamic Adaptation of Smart Cities to Cope with Crises and Disruptions (NORTE-01-0145-FEDER-000073), supported by Norte Portugal Regional Operational Programme (NORTE 2020), under the PORTUGAL 2020 Partnership Agreement, through the European Regional Development Fund (ERDF).

Contents

List of Figures

List of Tables

1. Introduction

1.1 Motivation

In some parts of the world, the provision of medical assistance can be a daunting task, and this is mainly due to the lack of proper roads or transportation infrastructure. This problem is particularly prevalent in rural areas or places with difficult terrain, such as mountains or jungles, where the construction of roads is often challenging or even impracticable. In addition to the lack of proper roads or transportation infrastructure, poverty in some countries can exacerbate the problem of limited medical assistance. Poor communities often have limited access to healthcare facilities and resources, making it even more challenging for healthcare workers to provide medical assistance to those in need.

Without proper roads or transportation infrastructure to reach or receive supplies, healthcare workers face enormous difficulties in accessing remote communities and providing timely medical assistance to those in need. Medical emergencies can quickly turn into life-threatening situations, as patients are unable to receive the care they need in a timely manner. Moreover, patients who require specialized medical attention often have to travel long distances to reach hospitals or clinics to receive medical treatments and supplies. In such situations, alternative means of transportation, such as helicopters, can be used to provide medical assistance to remote communities, as it currently occurs in Nepal for accessing the mountains or by hybrid airplanes landing in rivers as it occurs in the Amazon Forest in Brazil. However, these options are not always feasible due to their high cost and limited availability. As a result, many people in remote areas of the world continue to suffer from preventable illnesses or injuries that could have been treated if proper medical care was accessible. [1]–[3]

To address this problem, there is a need for a concerted effort from governments, non-governmental organizations (NGOs), and the private sector to invest in building and improving transportation infrastructure in remote areas and in accelerating the technological advances for providing innovative solutions to help address this problem. Between them, it is possible to cite Unmanned Aerial Vehicles (UAVs), commonly known as drones, and have been increasingly used to provide medical assistance in remote or difficult-to-reach areas. These UAVs can transport medical supplies, vaccines, and even blood to remote communities, enabling healthcare workers to provide life-saving medical care to patients who would otherwise have limited or no access to healthcare facilities.

However, while UAVs can be a game-changer in providing medical assistance to remote areas, there are still challenges that need to be addressed, such as regulatory barriers, limited infrastructure, and cost-effectiveness. Nevertheless, with the right investment and planning, UAVs have the potential to make a significant difference in improving access to medical care in remote areas. [4]

It is known that, in Nepal, the environmental conditions at some periods of the year and in some mountain, regions are not favorable for aerial vehicles, putting in danger the life of their occupants or even making impracticable their flight. In this context and with the objective to provide more effective medical supplement to remote areas in Nepal, the optimization and analysis of the composite wing presented in this master thesis was developed being a part of the developing of a fixed wing UAV, Anuj Regmi's project in the SYSTEC Lab, C2SR Lab of the Electrical engineering department of FEUP, whose head is professor António Pedro Rodrigues Aguiar.

It is important to highlight that the payload capacity of this type of aircraft is of utmost importance as it directly influences the ability to deliver essential medical supplies to remote and distant locations. To enhance the effectiveness of these missions, it becomes imperative to optimize the structural components, thereby reducing the overall weight of the UAV. However,

it is crucial to emphasize that this optimization should not compromise the safety and structural integrity of the aircraft. By achieving a lightweight yet robust structure, it becomes possible to maximize the payload capacity and facilitate the delivery of a larger quantity of life-saving medicines to even the most remote areas.

The SYSTEC lab is a control system laboratory of the electrical department of the Faculdade de Engenharia da Universidade do Porto and the mechanical engineering projects that take place there are inserted in the context of creating hardware such as mechanical systems to insert the controllers developed, many times associate with humanitarian causes.

1.2 Objectives

The objectives of this work can be divided into three main parts. The first part involves presenting the complete development of the First Aircraft (prototype), which aims to validate methodologies, establish more realistic weight ratios, and gather flight data to produce a more optimized final aircraft, the Medical UAV. This includes a concise overview of the sizing, design, and manufacturing process, as well as the results of real test flights.

Afterward, the second main part of the work is to develop a highly customizable computational tool in Python to minimize the weight of the composite structure in the wing of the Medical UAV (Second Aircraft). This entails creating a Genetic Algorithm (GA) tailored to the application and integrating a surrogate model with ABAQUS finite element software, enabling the prediction of the Tsai-Hill failure index for solution. In the current approach, the Tsai-Hill failure criteria, relying on linear assumptions, are employed to assess composite structure failure in the Medical UAV wing. However, Tsai-Hill has limitations, notably when dealing with nonlinear materials and correlated failure modes. If more time were available, integrating alternative criteria like the Tsai-Wu, Puck, or Hashin methods would be advantageous. It is possible to point out that the Tsai-Wu criteria offer a more detailed analysis under various loading conditions, the Puck criteria are suitable for laminated composites and multiaxial loading, and the Hashin criteria provide a more comprehensive assessment, considering multiple failure modes and their interactions. These alternatives promise more accurate predictions of failure, enhancing the safety and performance of the aircraft.

The third main part is to develop the wing structure for the final Medical UAV, which involves applying the developed computational tool, using one selected load case from the V-n diagram to the wing structure. The application of the computational tool aims to optimize all the structural elements of the wing, including skin, spars, and ribs, with the goal of obtaining the lightest and most efficient layup for the final wing, ensuring no composite failure occurs. The decision to perform the optimization for one load case is influenced by the constraint of limited time and the expectation that this process will be similarly applied to the other load cases.

1.3 Structure of the Thesis

In alignment with the previously described objectives the chapters of this work follow the logical order of presenting the complete development of the First Aircraft (Prototype), development of the computational tool and application of the computational tool to the Medical UAV (Second aircraft) wing.

The 2nd chapter of this work presents a state of art and literature review of Unmanned Aerial Vehicles (UAVs), composite materials, composite failure, optimization algorithms, surrogate models, and regression models.

The 3rd chapter approaches the complete development of the First aircraft prototype, briefly describing the sizing process, design of parts, manufacturing, presentation of the final manufactured aircraft and flight test.

4th chapter presents the sizing results of the Second Aircraft (Medical UAV), the aerodynamic load distribution and the wing topology.

The 5th chapter is dedicated to the development of the computational tool, which includes the development of the genetic algorithm, the composition of the surrogate models, including the sampling and regression methods used and studies to validate the developed computational tool.

The 6th chapter includes the application of the computational tool to the Medical UAV wing, presenting the optimization process and results for the skin, spars and ribs.

The proposition of future work and conclusions are presented in 7th chapter.

2. State of Art and Literature Review

2.1 Unmanned Aerial Vehicles (UAVs)

Drones, also known as Unmanned Aerial Vehicles (UAVs), are becoming increasingly popular and versatile in a variety of industries. In recent years, advances in technology have made drones more affordable, more reliable, and more versatile, opening a wide range of new possibilities for their use. It is known that fixed-wing UAVs and multi-copters are the two main types of drones used for various purposes. Fixed-wing UAVs are more suitable for longer-range operations, while multi-copters are more effective for shorter-range missions. Fixed-wing UAVs are typically launched from a runway or catapult and use wings to provide lift, while multi-copters use multiple rotors to provide lift and maneuverability.[5]

One of the most common applications of drones is in aerial photography and videography. Drones equipped with high-resolution cameras have made it possible to capture stunning aerial footage that was previously only possible with expensive helicopters or airplanes. This has revolutionized the film and photography industries. Fixed-wing UAVs are particularly well-suited to this application, as they can cover large areas quickly and efficiently. In addition to photography and videography, drones are also being used for a wide range of commercial and industrial applications. Fixed-wing UAVs are particularly effective for agriculture, mapping, and surveying applications, where they can cover large areas quickly and efficiently. For example, drones equipped with infrared cameras can be used to detect crop health and identify areas of water stress and nutrient deficiency, enabling farmers to optimize their crop yields. Multi-copters, on the other hand, are more suitable for applications that require maneuverability and hovering capabilities. They are commonly used for inspections, search and rescue operations, and surveillance applications. Multi-copters are also used for delivery of goods and services. Tech companies are investing heavily in drone delivery technology, with the potential to revolutionize the way we receive goods and services. However, the use of drones also presents a number of challenges and concerns, particularly around safety and privacy. There have been incidents of drones interfering with commercial aircraft, and concerns about the potential for drones to be used for illegal activities. In addition, there are concerns about the privacy implications of drones equipped with high-resolution cameras, particularly in urban areas. [5]

In addition, for the described application the idea of having the availability of vertical take-off and landing would represent a wider use since it would be less restricted by terrain conditions. For this, and besides the idea of multi-rotor, it is possible to consider the idea of fixed-wing VTOL configuration. The Vertical Takeoff and Landing (VTOL) drones are a type of unmanned aerial vehicle (UAV) that have the ability to take off and land vertically, without the need for a runway. This makes them ideal for operations in urban areas or remote locations where there are no suitable runways available. One of the main advantages of VTOL drones is their ability to hover in one place. In addition, they can fly in a wider range of weather conditions than conventional fixed-wing drones, as they can remain stationary in high winds or hover over areas with limited access. Another advantage to be mentioned is their ability to take off and land from a variety of surfaces, including uneven terrain, water, and ships. This makes them versatile for various types of missions. However, this drone configuration also has some limitations that must be taken into consideration when choosing the appropriate drone for this particular mission. For example, they typically have shorter flight times and lower speeds than fixed-wing drones due to their design and power limitations. They also require more energy to hover, which can limit their range and payload capacity. In addition, VTOL drones are more complex than fixed-wing drones, requiring more components and maintenance. This can make them more expensive to produce and operate than conventional fixed-wing drones. [6]

Since the use of drones and Unmanned Aerial Vehicles (UAVs) has been growing steadily in the medical field, with the potential to revolutionize the way medical care is delivered, it is possible to find many state of art examples of the most diverse configurations being developed or in operation around the word. In recent years, researchers, healthcare professionals, and technology companies have been exploring the use of drones and UAVs in various medical applications, from transporting medical supplies to delivering blood and organs for transplantation.

One of the key advantages of using drones for medical purposes is the ability to transport medical supplies quickly and efficiently to remote or hard-to-reach areas. For example, in rural areas of Africa, where access to healthcare facilities is limited, drones have been used to transport medical supplies and samples to hospitals, clinics, and laboratories. This has helped to improve the speed and accuracy of medical testing and diagnosis, ultimately leading to better patient outcomes. In addition, for transporting medical supplies, drones have also been used to deliver life-saving medical care in emergency situations.

In 2016, a company called Zipline launched a drone delivery service in Rwanda that delivered blood to remote hospitals in the country. The service has been incredibly successful, with Zipline reporting that they have delivered more than 25,000 units of blood to hospitals in Rwanda since the service launched. Their catapulted fixed wing UAV (Figure 1) can fly up to 150 km round trip, carrying payloads of up to 1.8 kg to be parachuted in the destination. [7]

Figure 1 - Zipline delivery UAV [7]

Matternet is another company that uses quadcopter drones (Figure 2) to transport medical supplies, such as blood and medicine, in urban areas. Their drones can fly up to 20 km on a single charge and carry payloads of up to 2 kg. [8]

Figure 2 - Matternet's delivery UAV [8]

Wing is a company owned by Alphabet, Google's parent company, that uses vertical takeoff and landing (VTOL) drones (Figure 3) to deliver medicine, snacks, and other small items in Virginia and Australia. Their drones can fly up to 20 km round trip and carry payloads of up to 1.5 kg. [9]

Figure 3 - Wing's delivery UAV [9]

Vayu is a company that uses VTOL fixed-wing configuration drones (Figure 4) to transport medical supplies, such as vaccines and blood, in Madagascar. Their drones can fly up to 100 km round trip and carry payloads of up to 1.5 kg. [10]

Figure 4 - Vayu's delivery UAV [10]

Moreover, drones of the most various configurations have been used to deliver medical supplies and equipment to areas of difficult access, affected by natural disasters or humanitarian crises, where access to healthcare facilities is often severely limited. From the explained configurations and examples that currently apply their use and having into account the type of mission and balancing the pros and cons, for this specific project that aims the reduction of complexity and resources needed, allowing the easier reproductivity of the project. Also, it is possible to mention the necessity of carrying weight for long distances in the shortest period. The alignment of the mentioned arguments leads us to the use of conventional fixed-wing airplane for the development of the current UAV.

2.2 Composite Materials

Considering the objective of achieving a lighter weight and more weight-efficient structure to enable increased payload capacity, faster flight speeds, or extended flight distances, the utilization of composite materials becomes crucial. In this regard, it is noteworthy to mention the increasing popularity of carbon fiber composites in aircraft design and manufacturing. These composites exhibit an exceptional combination of high strength, stiffness, and lightweight properties. Carbon fibers themselves consist of highly aligned

graphite sheets, resulting in excellent mechanical properties when integrated into composite materials. Notably, the strength-to-weight ratio of carbon fiber composites surpasses that of traditional materials like aluminum and steel, making them an ideal choice for aircraft design applications.[11]

Certifying aerostructures made of composite materials under regulatory authorities poses significant challenges due to the unique characteristics of these materials. Although composites offer numerous advantages in terms of strength, weight reduction, and performance, their certification requires meticulous evaluation and validation to meet stringent safety regulations. Several factors contribute to the complexity of certifying composite aerostructures. Firstly, composite materials exhibit variability in properties such as fiber orientation, resin content, and fiber-to-resin ratio. These variations can affect the structural integrity of the aerostructure, necessitating consistent material properties and reliable manufacturing processes. The manufacturing quality control is another critical aspect. The intricate procedures involved in composite manufacturing, including layup, curing, bonding, and trimming, require rigorous quality control measures. Adhering to industry standards and ensuring compliance throughout the production process is vital for certification. Designing and analyzing composite aerostructures is more intricate than traditional metallic structures. Unique behaviors of composite materials, such as laminate stacking sequence, necessitate specialized expertise, advanced simulation techniques, and comprehensive testing to meet certification requirements. Moreover, the certification standards established by aviation authorities, such as the FAA or EASA, govern aerostructure certification [12], [13]. However, these standards evolve with advancing composite technology, making it challenging to keep up with the changing requirements. Still, it is possible to face additional challenges for damage tolerance and inspections. And considering that composite materials can be more susceptible to damage, requiring specialized inspection techniques to detect and assess issues such as delamination or impact damage. [14], [15]

Despite the mentioned difficulties, carbon fiber composites are more often present in various, most recent, aircraft components, such as wings, fuselages, and tail sections. For instance, Boeing's 787 Dreamliner uses carbon fiber composites for more than 50% of its structural weight [16]. It is important to mention that these difficulties are more potentialized for passenger aircrafts, while the UAVs can face less restrict regulation that allows their use exploratory and innovative way, which presents a favorable opportunity to facilitate the acceptance, by the certification authorities, of novelties in composite structures for passengers' aircrafts.

Even considering as main material for this project the CFRPs (Carbon Fiber Reinforced Polymers), it is worth mentioning the hybrid composite structures that have emerged as a significant development in the field of UAV design, offering a combination of materials to achieve specific performance characteristics. By combining carbon fiber composites with other materials such as glass fibers or Kevlar, engineers can leverage the unique properties of each material to optimize the design for specific requirements. One of the key advantages of hybrid composite structures is their ability to enhance impact resistance and vibration damping. While carbon fiber composites excel in providing high strength and stiffness, they can be brittle and prone to damage upon impact. By integrating materials like glass fibers or Kevlar, which have excellent impact resistance properties, the resulting hybrid structure can better absorb and dissipate energy during impacts, thereby increasing the overall durability and resilience of the UAV. Moreover, hybrid composite structures offer the opportunity for cost-effective solutions. Carbon fiber composites can be relatively expensive compared to other reinforcing materials. By strategically incorporating less costly fibers like glass or natural fibers in certain areas of the structure where high strength is not the primary requirement, it is possible to achieve a balance between performance and cost-effectiveness. Another advantage of these structures is that they also enable customization and optimization of properties for different regions of the

UAV. For example, in areas where flexibility and impact resistance are crucial, Kevlar or other aramid fibers can be incorporated. In regions where stiffness and strength are paramount, carbon fiber composites can be utilized. This flexibility allows for the creation of UAV structures that are optimized for weight reduction, performance, and reliability in specific areas.[16]–[18]

However, there are also challenges associated with hybrid composite structures. Ensuring proper bonding and compatibility between different materials can be complex, requiring careful consideration of manufacturing processes and material compatibility. Additionally, the optimization of hybrid structures requires advanced modeling and analysis techniques to determine the most effective combination of materials and their distribution within the UAV structure. Despite these challenges, the development of hybrid composite structures offers exciting opportunities for UAV designers and manufacturers. By combining the unique properties of different materials, engineers can create UAVs with improved impact resistance, vibration damping, cost-effectiveness, and tailored performance characteristics. The ongoing research and advancements in hybrid composites hold great potential for further enhancing the capabilities and applications of UAVs in various industries.

Despite the many advantages of these materials for structures, carbon fiber composites also have some limitations in this matter. Such as their heterogeneity and difficulty predicting the behavior. And one of the most significant is the difficulty of repairing damaged parts. Carbon fiber composites are highly sensitive to impact damage, and even small cracks or dents can compromise their integrity. Therefore, it is essential to inspect and repair damaged carbon fiber components regularly. In recent years, there has been an increasing focus on developing sustainable composite materials, including carbon fiber composites, that can be recycled or reused at the end of their lifespan. Researchers are exploring new ways to break down and reuse composite materials, such as using solvents to dissolve the resin material and recover the carbon fibers. The development of sustainable composite materials is critical to reducing the environmental impact of the aerospace industry.[11], [19]–[21]

About manufacturing processes, in recent years the advancements in composite manufacturing, such as the carbon fiber reinforced polymers, have led to stronger and more durable composites while simultaneously reducing production costs. The manufacturing process for carbon fiber composites typically involves layering the fibers in a specific orientation and then bonding them with a resin material, such as epoxy. This creates a highly customizable material with excellent mechanical properties, such as high stiffness, low weight, and resistance to corrosion and fatigue. For carbon fiber structures this step plays a critical role in producing high-quality and reliable components for various applications. These processes involve transforming carbon fiber reinforcements into composite structures with precise geometries and desired mechanical properties. It is possible to mention some of the most common manufacturing processes, such as follows:

- Hand Layup:

Hand layup is a manual process that involves the precise placement of carbon fiber materials onto a mold or tool (Figure 5). Layers of dry carbon fiber fabric or unidirectional tapes are individually applied to the mold, and epoxy resin is then manually brushed or rolled onto each layer. This process allows for flexibility and customization, as skilled operators can adjust fiber orientations and resin distribution. However, hand layup can be time-consuming and labor-intensive, posing challenges in maintaining consistent quality and ensuring uniform properties across multiple parts, which makes it better suited for low-volume production or prototype development. The advancements in hand layup techniques have focused on improving efficiency and consistency. Automated material cutting systems, such as computer-controlled fabric cutters, enable precise and repeatable fiber placement. Vacuum-assisted resin

infusion (VARI) or vacuum bagging techniques can be integrated with hand layup to enhance resin impregnation and reduce voids [11], [16].

Figure 5 - Hand Layup

- Layup Over Foam Method:

The technique of encasing reinforced materials around a pre-formed foam core offers a convenient means of replicating a part without the need for specialized tools, as the foam core itself acts as the tool. This method is commonly employed in the construction of home-built aircraft, presenting a highly cost-effective fabrication approach by eliminating the requirement for additional tooling. When producing a small quantity of parts, it proves advantageous to create a foam core and overlay the composite materials onto the precisely shaped core achieved using a hot-wire saw. The hot-wire saw consists of a taut stainless steel safety wire stretched between two tubular components. By passing an electric current through the wire, it becomes heated and effectively burns (melts and cuts) through the foam material. To achieve a smooth and precise cut, templates are employed, and the hot-wire is gently guided around these templates with light pressure. Excessive force applied against the template may cause it to shift or result in the foam block flexing, leading to an uneven cut of the foam core. Therefore, it is crucial to maintain appropriate wire tension and temperature for optimal cutting performance. Following the completion of the foam core cutting process, any surface irregularities are smoothed out using sandpaper. Prior to applying wet layup laminates, the surface is sealed with micro/epoxy resin. Subsequently, the laminates are cured at room temperature to achieve the desired structural integrity [11]. The described process is exemplified in Figure 6.

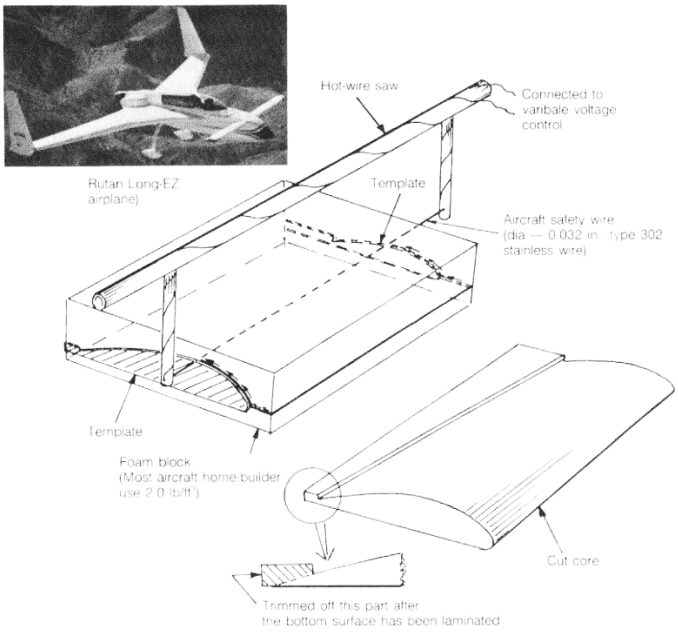

Figure 6 - Hot-wire Cut Method (Which has been successfully used on home-built Airplanes) [11]

- 3D Printing/Additive Manufacturing:

Additive manufacturing, or 3D printing, has gained significant attention in carbon fiber composite production. In this process, carbon fiber-reinforced filaments or powders are deposited layer by layer to build up the desired structure. Additive manufacturing offers the ability to create complex geometries, including internal channels or lattice structures, with reduced material waste. The studies in additive manufacturing have the objective of improving the strength and interfacial bonding between the carbon fibers and the matrix material. Methods such as continuous fiber reinforcement, where continuous carbon fibers are integrated into the printed part, can significantly enhance the mechanical properties. Additionally, the development of advanced multi-material or hybrid printing systems allows for the integration of different materials within a single component, further expanding the possibilities of carbon fiber additive manufacturing [22]. Figure 7 presents an example of addictive manufacturing.

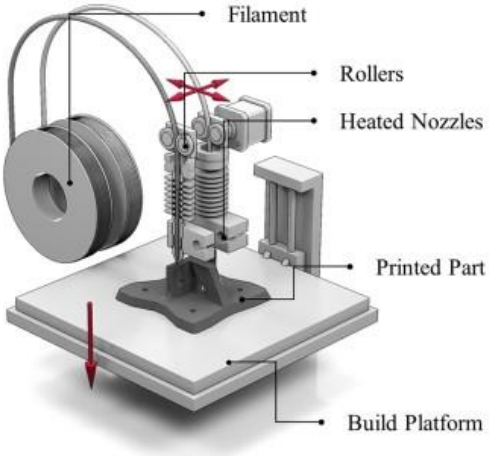

Figure 7 - Schematic representation of fused filament fabrication using two materials. [22]

- Resin Transfer Molding (RTM):

RTM is a closed-mold process where dry carbon fiber preforms are placed into a mold, and resin is injected under pressure. The resin flows through the preform, wetting out the fibers and filling the mold cavity. RTM offers better fiber control and repeatability compared to hand layup, resulting in more consistent composite properties. It is suitable for medium to high-volume production. Recent developments in RTM techniques have focused on reducing cycle times and improving resin flow control. Techniques such as vacuum-assisted resin transfer molding (VARTM) and pressure-assisted resin transfer molding (PARTM) have been developed to enhance resin flow and minimize void formation. Additionally, the use of advanced tooling materials, such as reusable silicone molds or carbon fiber composite molds, has improved the durability and efficiency of the RTM process (Figure 8**Error! Reference source not found.**) [11], [16].

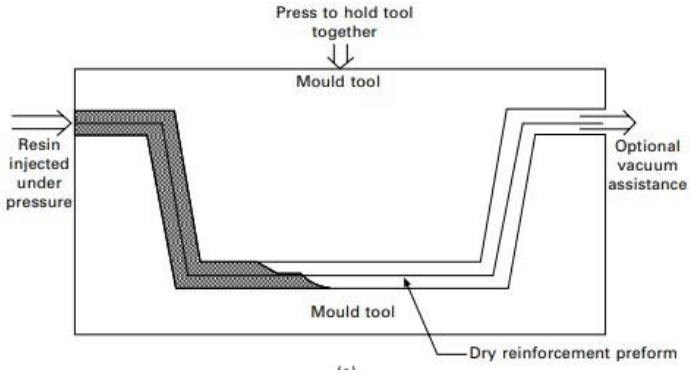

Figure 8 - Resin Transfer Molding [12]

- Resin film infusion (RFI):

The resin film infusion (RFI) process offers an effective method for producing relatively large structures, such as stiffened skins and rib-type structures. This process involves the use of an open mold, where layers of dry fabric and solid resin film are meticulously stacked. The resin film utilized is a B-stage cured resin, similar to the cure condition found in prepreg resin matrices. During the RFI process, the resin film is strategically placed either at the bottom, top, or between the layers of fabric. The entire assembly is then carefully sealed within a vacuum bag, and air is subsequently extracted using a vacuum pump. To facilitate the infusion, the assembly is subjected to both pressure and heat within an autoclave. The temperature is gradually raised to reduce the resin viscosity, enabling it to flow smoothly into the fabric layers under the applied pressure. This controlled infusion ensures that the resin adequately permeates the fabric, resulting in a uniform and well-consolidated structure. Once the infusion is complete, the pressure and temperature are further increased to promote full consolidation and curing of the component. The RFI process provides several advantages, including the ability to produce large and complex structures with high-quality resin distribution. The controlled application of pressure and heat ensures effective consolidation and curing, resulting in structurally sound and durable components. This process is particularly suitable for applications where stiffened skins and rib-type structures are required, offering a reliable and efficient manufacturing solution [16]. The schematic representation of this process is presented in Figure 9.

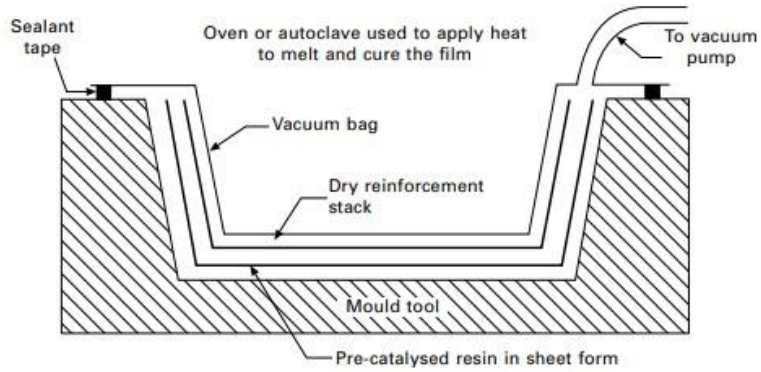

Figure 9 – Resin Film infusion [16]

Overall, the use of composite materials in aircraft design and manufacturing is a rapidly evolving field with significant potential for innovation and improvement. Ongoing research and development are focused on improving their properties, developing new manufacturing techniques, incorporating nanoparticles, and creating hybrid materials.

2.4 Composite materials failure analysis

Composite materials are widely used in the aeronautical industry due to their excellent strength-to-weight ratio and tailored mechanical properties. However, understanding and predicting the failure behavior of composites is essential for ensuring their safe and reliable performance. Composite failure can occur through different modes, for example, it is possible to mention the matrix and fiber failures. Matrix failure refers to the damage or failure of the polymer matrix that binds the reinforcement fibers in a composite material. The matrix can fail under various loading conditions, such as tension, compression, shear, or a combination of these. Matrix failure may include cracking, debonding, delamination, and plastic deformation of the polymer matrix. It can occur due to excessive stress, strain, or aging of the matrix material. In the other hand, fiber failure is the failure of the reinforcement fibers in a composite material. Fiber failure can happen in different ways, depending on the fiber type, such as carbon

fibers, glass fibers, or aramid fibers. It may include fiber breakage, pull-out, or fiber-matrix interface debonding. Fiber failure can occur under tensile, compressive, or shear loading, and it is often influenced by factors like fiber misalignment, fiber-matrix adhesion, and fiber strength. [16], [23]

For studying the occurrence of failure in a composite material structure, it is possible to use failure criterion such as Puck, Hashin, Tsai-Hill or Tsai-Wu. The Puck Failure Criteria is suitable for laminated composites and multiaxial loading scenarios, considering interaction between different material properties, and the Hashin Failure Criteria provides a comprehensive assessment by considering multiple failure modes and their interactions [24], [25].

Hill modified the von mises criterion for the case of ductile metals with anisotropy and later Tsai adapted this criterion for unidirectional composite laminae with transverse isotropy. This failure criterion, named Tsai-Hill (deviatoric strain energy) is expressed in terms of a single criterion, and it allows for considerable interaction among the stress components. The formulation involving Tsai-Hill is described by Equation 1 to Equation 3.

$$\frac{\sigma_1^2}{F_1^2}+\frac{\sigma_2^2}{F_2^2}+\frac{\tau_6^2}{F_6^2}-\frac{\sigma_1\sigma_2}{F_1^2}=1 \tag{1}$$

$$F_1=\begin{cases}F_{1t}\ when\ \sigma_1>0\\F_{1c}\ when\ \sigma_1<0\end{cases} \tag{2}$$

$$F_2=\begin{cases}F_{2t}\ when\ \sigma_2>0\\F_{2c} when\ \sigma_2<0\end{cases} \tag{3}$$

Where σ_1 and σ_2 represent the normal and transverse stresses, respectively, while τ_6 denotes the shear stress. F_{1t} and F_{1c} correspond to the maximum tensile and compressive stresses in the normal direction, respectively. Similarly, F_{2t} and F_{2c} represent the maximum tensile and compressive stresses in the transverse direction, respectively. Lastly, F_6 represents the maximum shear stress. It is worth mentioning that in this failure criteria, no distinction is made between tensile and compressive strengths. The strength parameters must be specified according to the signs of the normal stresses σ_1 and σ_2. [26], [27]

Besides, it is possible to present the Tsai-Wu failure criterion that is a modified tensor polynomial criterion for orthotropic or transversely isotropic laminae. In this case it is possible to have a distinction between tensile and compressive strengths, also accounting for the interaction between the normal stresses. The formulation for this criterion is presented by Equation 4.

$$\frac{\sigma_1^2}{F_{1c}F_{1t}}+\frac{2F_{12}^*\sigma_1\sigma_2}{\sqrt{F_{1c}F_{1t}*F_{2c}F_{2t}}}+\frac{\sigma_2^2}{F_{2c}F_{2t}}+\frac{\tau_6^2}{F_6^2}+\left[\frac{1}{F_{1c}}-\frac{1}{F_{1t}}\right]\sigma_1+\left[\frac{1}{F_{2c}}-\frac{1}{F_{2t}}\right]\sigma_2=1 \tag{4}$$

Where F_{12}^* is the interaction term. The admissible range of the normalized interaction term that ensures a closed envelope and acceptable inclinations of the tangents to the failure envelopes at the four anchor points changes from material to material, but it is generally between -1 and 0. It is also possible to note that when the normalized interaction term is -1/2, the classical von Mises failure criterion can be recovered if anisotropy is reduced to isotropy and the tensile and compressive strengths are equal.

The failure index in both the Tsai-Hill and Tsai-Wu criteria is used to evaluate whether a composite material is predicted to fail under a specific stress state. If the calculated value of the failure index exceeds a value of 1, it indicates that failure is likely to occur in the composite material under the given stress conditions. In other words, a failure index greater than 1 signifies that the applied stress state exceeds the material's failure strength and indicates a higher likelihood of failure. However, it's important to note that the Tsai-Hill and Tsai-Wu criteria do not provide information about the specific failure mode that will occur. They only predict the overall failure occurrence based on the combination of stress components. Being them

generalized failure criteria that consider a combined stress state and provide a conservative estimation of failure for composite materials.[26], [27]

2.3 Optimization

2.3.1 Structural Weight Optimization

Airplane wing weight optimization is a crucial area of research and development in the aerospace industry. Efficient wing design plays a significant role in achieving fuel efficiency, performance, and overall aircraft weight reduction. Wing weight optimization can be achieved through various approaches that touch on different areas of engineering, such as aerodynamics, structural, materials and manufacturing. Focusing on structural it is possible to mention the two most common approaches for composite material wings that coupled leads for the most weight optimized structure.

For starting, it is possible to briefly mention the topology optimization, that from structural analysis consists in determine the optimal layout and material distribution within a given design space. In this approach, the structural analysis will focus on identifying the load distribution and paths, reorganizing the structural components such as the spars and ribs, changing their spacing and positions. Another interesting part of this approach is related to material removal, that from the load distribution within the structural elements, it is possible to identify the regions where material can be removed without compromising the structural integrity [28]. For topology optimization there are many tools implemented directly in the finite element software platforms, mainly focusing on material removal. Figure 10 presents a graphical representation of the topology optimization.

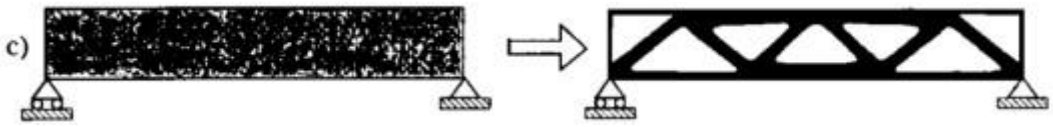

Figure 10 - Topology Optimization [28]

The approach that is the focus of this work is composite layup optimization. As previously mentioned, composite materials, such as CFRP, are highly customizable materials, where the number of layers and the orientation plays an important role in the final mechanical properties in each different direction. Normally, different fiber orientations, stacking sequences and laminate thickness are evaluated to determine the optimal arrangement that meets the structural requirements and loading conditions fulfilling the specific mechanical requirements. It is also important to mention that the manufacturing constraints must be respected during this phase, as an example, unconventional fiber orientations are difficult to implement in manual manufacturing processes [29], [30]. Another constraint for unusual fiber orientations is that they can face challenges when dealing with regulatory agencies, in this case, the authorities may require additional testing and analysis to demonstrate the structural integrity and reliability of the composite materials.[31].

Optimizing the layup of composite materials in aerostructures is a complex and time-consuming process that involves considering numerous variables and their influence on the overall structure. Each section of the structure plays a critical role in determining its performance, strength, and weight. The layup optimization process requires careful analysis of various factors, such as fiber orientation, ply thickness, stacking sequence, and the number of layers. These variables directly impact the structural integrity, stiffness, and weight of the mechanical structure. Achieving the optimal combination of these variables is essential to maximize structural efficiency while meeting the design requirements and regulatory standards. The optimization process involves iterating through different combinations of variables to

identify the most favorable layup configuration, with help of finite element software, like ABAQUS, that serves as a powerful tool for conducting in-depth analyses of composite structures. It enables the creation of accurate virtual models of aerostructures, allowing for the simulation of different loading conditions and the study of composite material behavior. This iterative process considers trade-offs between factors such as weight reduction, stiffness, strength, and manufacturing feasibility. It may involve adjusting the fiber orientation, changing the number of layers, or varying the ply thickness in different sections of the structure. Each change in the layup configuration has a ripple effect throughout the entire structure. For example, modifying the fiber orientation in one section may impact the load transfer and stress distribution in adjacent sections. Therefore, it requires careful evaluation of the interactions between different parts of the structure to ensure a holistic and optimized design. The time spent on a manual layup optimization depends on the complexity of the structure, the number of variables involved, and the desired level of optimization. It often requires several iterations, simulations, and analysis steps to converge on an optimal solution. [30], [32]–[34].

To enhance the efficiency and accuracy of the optimization process for reducing time spent in structural weight optimization, computational tools have played a crucial role. These tools automate various aspects of the process, enabling the expedited exploration of optimal solutions with improved results. A key focus area is the development of optimization algorithms capable of navigating complex design space. These algorithms utilize mathematical techniques to iteratively explore different design configurations, adjusting variables such as fiber orientation, layer count, and laminate thickness to achieve the desired weight reduction. By employing these optimization algorithms, the need for manual trial and error is eliminated, saving valuable time and resources. The integration of finite element software, such as Abaqus, is also instrumental in this process. This software provides a comprehensive platform for studying composite materials, enabling to simulate and analysis of various composite layup configurations. By combining finite element analysis with optimization algorithms, a systematic evaluation of different design options can be conducted, facilitating the identification of the most promising solutions. Computational tools and optimization algorithms offer the advantage of considering multiple variables simultaneously, considering the interconnectedness and dependencies between different sections of the structure. This holistic approach allows for the optimization of not only individual components but also the entire system, considering the interactions and trade-offs between different sections. Through automated optimization, a wider range of design possibilities can be explored, leading to the identification of the most efficient combinations of fiber orientation, layering, and other parameters. The utilization of these computational tools not only reduces the time required for optimization but also increases the precision and reliability of the results. By leveraging advanced algorithms, robust and accurate optimization outcomes can be achieved, resulting in improved weight reduction without compromising structural integrity or performance. Furthermore, these tools enable the exploration of alternative design concepts, pushing the boundaries of innovation and uncovering unconventional solutions that may not be readily apparent through traditional design approaches. In this sense it is possible to present some examples of the existing commercial composite optimization.

- OptiStruct

  OptiStruct is a structural optimization software developed by Altair Engineering. It offers a range of optimization algorithms for composite structures, including layup optimization. OptiStruct can be integrated with popular FEA software packages and provides capabilities for optimizing composite layups based on various design criteria, such as weight, stress, and fatigue.[35].

- OptiSlang:

OptiSLang is a powerful software tool that is widely used in various engineering disciplines, including composite materials. It offers comprehensive capabilities for performing optimization, uncertainty quantification, and sensitivity analysis in composite design and analysis processes. In the context of composite materials, OptiSLang provides an integrated environment for automating and accelerating the optimization of composite structures. It allows to define and control multiple design parameters, such as ply orientations, thicknesses, and stacking sequences, to achieve desired performance objectives, such as minimizing weight, maximizing strength, or improving fatigue life. OptiSLang combines with ANSYS to perform optimization tasks.[36].

- Insight:

Insight is a plug-in developed by Firehole Composites that specifically integrates with the ABAQUS software. It is a tool designed for composite material analysis and optimization within the ABAQUS environment. With Insight, it is possible to automatically generate optimized ply shapes and orientations, using advanced algorithms to meet design objectives such as minimizing weight or maximizing stiffness. The software provides visualization tools for evaluating optimized results, including graphical representations of ply orientations and detailed reports. By streamlining the optimization process, Insight improves design efficiency, reduces manual iterations, and saves time. Insight provides advanced capabilities for analyzing composite materials, including progressive failure analysis, laminate optimization, and reliability analysis. It offers functionalities such as failure criteria, damage modeling, and ply-by-ply stress and strain visualization. The plug-in aims to enhance the accuracy and efficiency of composite structural analysis and optimization workflows within ABAQUS.[34].

Despite the availability of commercial computational tools for composite optimization, there are certain limitations associated with these tools. Some of them have a high cost of acquiring and licensing these software packages. The cost factor can make them inaccessible for small or budget-constrained engineering teams or individual users. Another limitation is the presence of pre-established constraints within the software. While these tools offer a range of optimization algorithms and functionalities, they may have limitations in terms of the types of constraints that can be applied or the complexity of the optimization problem that can be solved. This can restrict the design space and limit the flexibility in achieving truly innovative or unconventional composite designs. Furthermore, commercial optimization tools may not always encompass the specific requirements or constraints of a particular composite application. Certain niche or specialized design considerations may not be adequately addressed by off-the-shelf software packages.

For this reason and recognizing the advantages offered by computational tools and optimization algorithms in streamlining the optimization process, this work aims to address the challenges of structural weight optimization in the context of wing design for medical delivery unmanned aerial vehicles (UAVs) by developing a customizable computational tool proper for this specific application. By leveraging the capabilities of this tool, which integrates an optimization algorithm, the objective is to enhance the efficiency, precision, and reliability of the weight reduction process for UAV wings.

2.3.2 Optimization Algorithms

For this work it is needed to select an appropriate optimization algorithm. For this choice it is necessary to consider the great number of expected variables, three for each section, the number of constraints, the possibility of dealing with some nonlinearity, the limitations in computational resources, time, and the complexity of the algorithm. For that it is possible to briefly compare some of the most popular algorithms normally used.

Gradient-based algorithms are optimization algorithms that use the gradient of the objective function to iteratively improve the solution. They can be efficient for optimization problems with a smooth and continuous objective function. However, they can struggle with non-linear or non-smooth objective functions in the local minima, plateaus, and discontinuities. Another common method is the exhaustive search that is a brute-force optimization algorithm that evaluates all possible solutions in the solution space. While it can be computationally expensive and time-consuming, they are a more suitable choice for small optimization problems with a limited number of variables. Another possible solution would be The Pattern search, that is an optimization algorithm that uses a set of search directions to explore the solution space. It can handle non-linear and non-smooth objective functions but again is particularly useful for problems with a small number of variables.

Genetic Algorithms (GA) are a type of optimization algorithm that is based on the principles of biological evolution. They can be used to solve complex optimization problems that have a large solution space and many constraints. In the context of composite structure optimization, genetic algorithms are a suitable choice for optimizing the number of layers in a composite structure because they can explore a large solution space efficiently, handle non-linearity, and incorporate constraints. Since, optimizing the number of layers in a composite structure is a non-linear problem because the number of layers can affect the composite's strength, stiffness, and weight in a non-linear way, the choice of genetic algorithms is well-suited for non-linear optimization problems because they can evaluate many potential solutions and identify non-linear relationships between variables.

Another advantage of GA is their ability to explore a large solution space efficiently. The number of layers in a composite structure can be varied over a wide range of values, and genetic algorithms can explore this space more efficiently than other optimization algorithms, such as exhaustive search or gradient-based algorithms. Still, it is needed to consider that the inclusion of constraints is important when optimizing the number of layers in a composite structure. For example, there may be constraints on the minimum or maximum thickness, weight of the composite structure and failure indexes. For this. genetic algorithms can handle such constraints by incorporating them into the fitness function, which guides the optimization process.

Finally, GA are a stochastic optimization method, meaning they use random mutation and recombination to explore the solution space. This can help avoid getting stuck in local optima, which can be a problem with deterministic optimization methods. Which lead to the conclusion that genetic algorithms are a suitable choice for optimizing the number of layers in a composite structure due to their ability to handle non-linearity, large solution spaces, constraints, and stochastic optimization.[37], [38].

2.3.3 Genetic Algorithm

Genetic Algorithms (GAs) are powerful global search heuristics designed to evolve solutions for various problem domains. Proposed by John Holland in 1975 [39], GAs have gained significant attention and widespread usage due to their effectiveness in navigating complex search spaces, including NP-hard problems. To apply a GA, the practitioner needs to determine the encoding scheme for representing solutions as chromosomes, establish an appropriate initial population through randomization, define a fitness function for evaluating candidate solutions, implement crossover and mutation operations, and set GA parameters such as population size, number of generations, and probabilities of crossover and mutation. These considerations play a crucial role in the successful application of GAs, allowing for the exploration and exploitation of solution spaces to find optimal or near-optimal solutions.

In genetic algorithms, biological terms are used in the context of analogy with real biology. For example, when referring to a chromosome in a GA, it represents a potential solution to the problem at hand. It is analogous to the genetic material found in living organisms.

Another example is the use of Allele to refer to a specific value or state that a gene can take. It represents the variation of a trait within a population. The last mentioned “Population” consists of a set of individuals, each represented by a chromosome. It represents the collection of potential solutions that have evolved over generations. Finally, it is possible to mention the use of nomenclature fitness that is a measure of the quality of an individual solution in the population. It determines the likelihood of an individual to be selected for reproduction and contribute to the next generation.

The first algorithm model proposed by Holland [39] was the simple genetic algorithm (SGA), whose structure was characterized by binary representation of the search space, fitness-based selection of the parents, low mutation probability, genetic inspired recombination, and generational selection of the survivors, where all offspring replace parents. This first approach proposed by Holland would include the main operators of selection, crossover, and mutation. The base of this algorithm can be described by Figure 11 that presents the generic scheme of Evolutionary Algorithms [38].

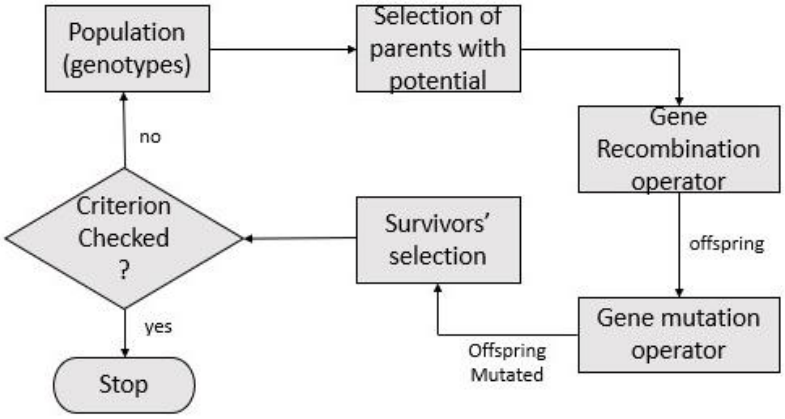

Figure 11 – Generic Scheme of Evolutionary Algorithms [38]

Since the GAs belong to the family of Evolutionary Algorithms (EAs) it is possible to retrieve this presented structure and expand the detailing for the main steps of its procedures. In this case, the algorithm follows the order described below in topics:

1. Initialization: The genetic algorithm starts by generating an initial population of random chromosomes. The population size is typically determined based on the problem's complexity and available computational resources. Each chromosome represents a potential solution to the problem at hand, and its characteristics are encoded within its genes.

2. Evaluation: Once the initial population is generated, each chromosome undergoes an evaluation process. This involves applying a fitness function that quantitatively measures the quality or suitability of the solution represented by the chromosome. The fitness function evaluates how well the solution satisfies the problem's objectives and constraints. The evaluation provides a fitness value for each chromosome, which serves as a basis for selecting parents for reproduction.

3. Selection: In the selection phase, individuals with higher fitness values are more likely to be chosen as parents for reproduction. The selection process is designed to favor chromosomes that exhibit desirable traits or characteristics. Various selection methods can be employed, such as tournament selection, roulette wheel selection, or rank-based selection. The goal is to create a mating pool that consists of chromosomes with better fitness values.

4. Crossover: Crossover, also known as recombination, is a fundamental genetic operator in GAs. It involves the exchange of genetic material between selected parent chromosomes to produce offspring. The crossover process mimics the idea of sexual reproduction in biology, where genetic information from two parents is combined to create genetically diverse offspring. Different crossover techniques exist, such as single-point crossover, multi-point crossover, or uniform crossover. These techniques determine how genes are exchanged between parents and influence the exploration of the search space.

5. Mutation: Mutation is another genetic operator that introduces small random changes to the offspring chromosomes. It helps introduce genetic diversity into the population and prevents premature convergence to suboptimal solutions. During mutation, certain genes within the chromosome are randomly altered, allowing for exploration of new regions in the search space. The mutation rate determines the probability of a gene being mutated, and it is usually set to a low value to ensure a balanced exploration-exploitation trade-off.

6. Replacement: After the offspring is created through crossover and mutation, they replace certain individuals in the current population. The replacement strategy ensures that the next generation of the population reflects improved solutions compared to the previous generation. Various replacement strategies can be employed, such as generational replacement (the entire population is replaced) or elitist replacement (the best individuals survive to the next generation). The replacement strategy influences the convergence speed and the preservation of the best solutions.

7. Termination: The GA continues to evolve generations until a termination condition is met. Common termination conditions include reaching a maximum number of iterations or generations, achieving a satisfactory fitness value, or running out of computational resources. Termination conditions ensure that the optimization process is bounded and does not continue indefinitely.

These procedures are better described for the specific application in chapter 5.2, while the flow diagram for a generic Genetic Algorithm is presented in Figure 12 from [38].

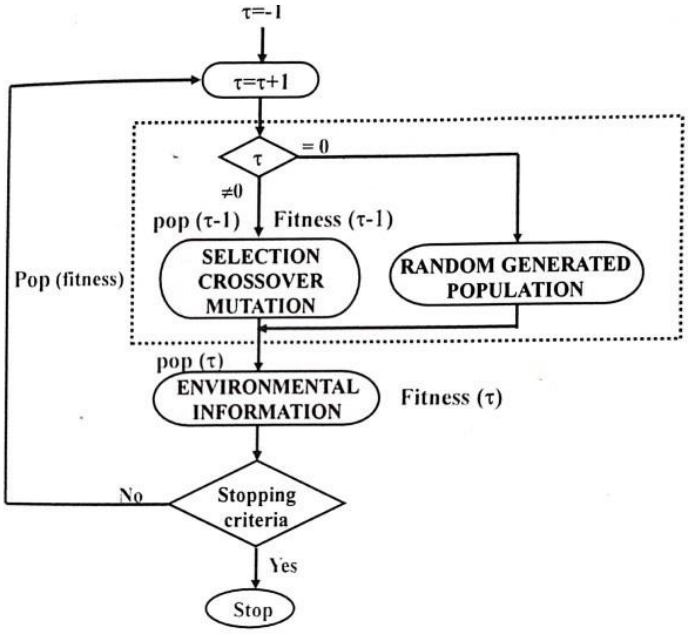

Figure 12 - Flow diagram for a generic GA [38]

The representation of the search space in Genetic Algorithms (GAs) is a crucial aspect that determines how candidate solutions are encoded and manipulated during the optimization process. This representation scheme establishes the connection between the genotype and phenotype of individuals, where the genotype represents the solution in a specific format, and the phenotype represents its expression or interpretation. To delve into the biological terms translated into the algorithmic context, the genotype refers to the genetic encoding or representation of a candidate solution within the GA. It takes various forms depending on the problem and the nature of the variables involved. For real-valued variables or parameters, binary encoding techniques can be employed to facilitate their representation.

Binary encoding enables the conversion of real-valued variables into binary string representations, allowing for manipulation and evolution using genetic operators like crossover and mutation. The process involves discretizing the variable's range into a predefined number of bits, where each bit represents a specific value or range within the variable's domain. The length of the binary string is determined by the desired precision or granularity of the variable. To convert a real-valued variable into its binary representation, the first step is to determine its range or domain. This range is then divided into equally spaced intervals, each corresponding to a unique binary code. The number of bits required to represent each interval depends on the desired precision and the total number of intervals. Further details on this specific application can be found in Section 5.2 of this project.

During the evolution process, genetic operators like crossover and mutation are applied to the binary strings to generate new offspring. Once the new binary strings are obtained, they are decoded back into their real-valued counterparts to evaluate their fitness and determine their performance in the optimization process. This type of representation provides a flexible and efficient approach for handling real-valued variables within genetic algorithms. It enables the algorithm to explore the solution space by manipulating binary strings while retaining the ability to represent and optimize real-valued parameters [37], [38].

2.3.4 Surrogate Models

Surrogate models are mathematical approximations or simplified representations of complex and computationally expensive systems or processes. They serve as efficient surrogates for the original system, enabling faster evaluations and explorations of the design space. In many real-world engineering and scientific applications, the evaluation of a system's behavior or performance can be time-consuming or costly. For example, running simulations, conducting physical experiments, or performing extensive computations might require significant resources and time. These models offer a way to address this challenge by providing a less computationally demanding alternative. Their basic idea is to construct a mathematical function or model that approximates the behavior of the original system based on a limited number of evaluations. These evaluations are typically obtained by sampling the original system at various input configurations. By capturing the input-output relationship of the system, surrogate models can predict the system's response at unexplored points within the design space. Surrogate models can be built using various techniques whose choice depends on the nature of the system, the available data, and the desired accuracy of the approximation, one example is the use of regression methods. [40].

The construction of a surrogate model for weight optimization of structures is advantageous, since this is an example of a very computationally expensive process, considering the evaluation of failure constraints for each individual is performed by a detailed finite element analysis, where the results are post-processed in each iteration. For this reason, it is possible to establish the interaction of optimization algorithms with the surrogate model to search for optimal design configurations in a more efficient way.

As a starting point, it is possible to mention that the choice of a sampling method is a crucial aspect when designing experiments, as it directly impacts the quality and reliability of the data collected. A well-designed sampling method ensures that the experimental data effectively captures the underlying behavior of the system or process being studied. This is particularly important in the context of Design of Experiments (DOE), where the goal is to understand the relationship between input variables and the corresponding system response. The sampling method determines how the input space is explored and the data points are selected. It plays a significant role in achieving a representative and diverse set of data points that adequately cover the input space. A poor choice of sampling method may result in biased or incomplete data, leading to inaccurate models and unreliable predictions. [41].

When talking about Design of Experiments (DOE) it is possible to relate to statistical techniques used to systematically design experiments and optimize processes by controlling and manipulating independent variables to determine their effect on a dependent variable. The goal of DOE is to determine the optimal settings for the independent variables to achieve the best possible results for the dependent variable. Still, it is possible to say that DOE is based on the principle of statistical inference, which is the process of using sample data to make inferences about a population. By carefully designing experiments and collecting data, it is possible to make accurate inferences about how changes in the independent variables affect the dependent variable. In this sense there are several types of DOEs, including full factorial designs, fractional factorial designs, response surface designs, and Latin Hypercube Sampling (LHS) designs. Each of these designs has its own strengths and weaknesses, and the choice of design depends on the specific problem being studied. [40]–[42].

Full factorial designs, known for their comprehensive approach, represent the most straightforward type of Design of Experiments (DOE) methodology. These designs involve testing every conceivable combination of independent variables at varying levels, thereby providing a thorough exploration of the input space. This sampling method is particularly well-suited when dealing with a limited number of factors and discrete or easily adjustable factor levels. However, it is important to acknowledge that the implementation of full factorial designs can be demanding in terms of time and resources, especially when the number of independent variables or levels becomes substantial. In the context of integrating a genetic algorithm with a surrogate model, the application of full factorial designs may not yield significant benefits [42]. This stems from the fact that the utilization of a pure genetic algorithm proves more advantageous, as the algorithm itself directs the search towards the desired solution region. Consequently, evaluating all possible individuals becomes unnecessary, as the genetic algorithm intelligently explores the search space based on evolutionary principles. By leveraging the genetic operators, such as selection, crossover, and mutation, the algorithm effectively evolves the population towards optimal solutions without exhaustively assessing every combination of variables.

The Latin Hypercube Sampling (LHS) method serves as an alternative to full factorial designs within the realm of Design of Experiments (DOE). LHS adopts a systematic approach to sampling, aiming to achieve representative and efficient coverage of the input space while reducing the number of required samples. Unlike full factorial designs that test every possible combination, LHS strategically selects a limited number of samples that effectively span the entire range of each input variable. LHS offers the advantage of a more balanced and evenly distributed exploration of the input space, even when working with a constrained sample size. This approach ensures that each factor level is well-represented across the samples, minimizing the risk of overlooking crucial regions or interactions within the design space. The methodology behind LHS involves dividing the range of each input variable into equal intervals or "bins" and randomly selecting one sample within each interval. This process guarantees that each sample is both unique and indicative of a specific range. By employing this stratified sampling approach, LHS provides more effective coverage of the input space compared to random

sampling or uniform grids. Consequently, an experimental design can be represented as a matrix p_{xd}, where p signifies the number of points and d represents the number of dimensions. In this matrix, the variables are represented by columns, and the samples are represented by rows. LHS generates points by dividing each of the d dimensions into p equal levels, assigning a single point (or sample) to each level. The objective is to generate points with orthogonal projections, whose specific locations are determined using a random procedure. [40], [43], [44].

One of the significant advantages of LHS is its capacity to optimize computational resources. With fewer samples required compared to full factorial designs, LHS proves particularly valuable when dealing with complex and computationally demanding models or simulations, where evaluating a large number of samples may be impractical. It is important to note, however, that while LHS offers advantages in terms of efficiency and coverage, it does not guarantee the same level of comprehensiveness as full factorial designs. Nevertheless, LHS remains a popular and valuable technique in the field of computer experiments and design optimization, especially for projects involving multiple independent variables, such as the current work, focused on the wing structural optimization. Figure 13 exemplifies with three-variables, ten-point Latin hypercube sampling plan.

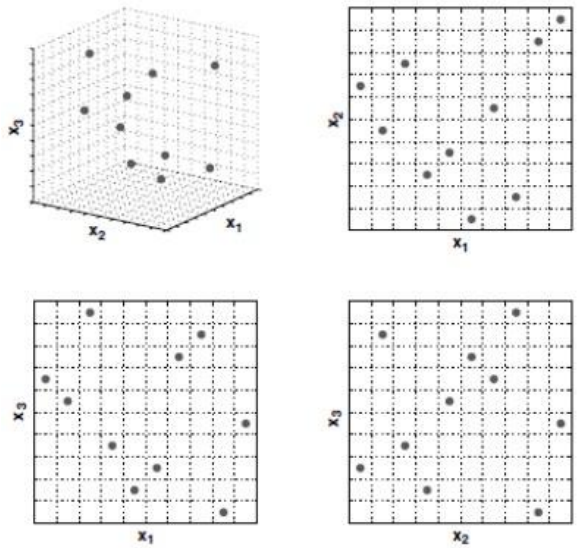

Figure 13 - Latin Hypercube representation [40]

Upon the establishment of the sampling strategy and completion of the Design of Experiments (DOE), the collected data is utilized for the construction of regression models. These models serve as mathematical representations that capture the relationship between the input factors and their corresponding responses, facilitating efficient prediction and exploration of the design space. Regression methods play a pivotal role in surrogate modeling as they enable researchers to comprehend the underlying trends and patterns inherent in the data. Numerous regression techniques exist, each possessing its own set of assumptions, strengths, and limitations. Among the commonly employed regression methods are linear regression, polynomial regression (which may incorporate normalization approaches such as Lasso, Ridge, or elastic net), and Gaussian process regression. The selection of a particular regression method relies on a range of factors, including the problem's nature, data characteristics, and the desired level of accuracy and interpretability. The subsequent sections will delve into a comprehensive elucidation of these methods.

2.3.5 Regression Methods

Regression methods play a pivotal role in the development of surrogate models, providing information about the relationships between variables, and the results of their

combinations. These statistical approaches aim to uncover the dependencies between a dependent variable and one or more independent variables. By fitting a regression model to the available data, also called training data, obtained with the previously stablished Latin hypercube method, it is possible to establish the degree of influence of different factors on the outcome of interest. These models offer a mathematical framework that allows the analysis and prediction of relationships between variables, revealing underlying patterns, trends, and performing predictions for unknown combinations of variables. In the context of this project, leveraging regression techniques is essential for analyzing complex datasets, with a particular focus on the impact of multiple predictors. [45]

The use of multi-regression enables the consideration of multiple independent variables simultaneously. By incorporating multiple predictors into the analysis, a more comprehensive understanding of the factors that shape the outcome can be gained, including intricate relationships and interactions. They facilitate the evaluation of individual contributions and the significance of each predictor, enabling informed decision-making and hypothesis testing. Within the realm of regression and multi-regression, various methodologies and approaches exist, each with its own set of assumptions, strengths, and limitations [46]. Techniques such as Gaussian process regression, linear regression, polynomial regression, and regression with regularization methods (such as Lasso, Ridge, or elastic net) offer versatile frameworks for analyzing data and extracting meaningful results.

This subchapter will delve into these regression techniques, providing an examination of their theoretical foundations. Understanding these techniques in detail will allow the evaluation of their implementation and comparison of their performance in the context of this work. By gaining a thorough understanding of these methodologies, the applicability of each approach can be assessed, determining which technique best suits the research objectives and dataset.

The following description, present in topics, of the regression methods presents their theoretical foundations, incorporating the formulation principles employed in the widely used scikit-learn library in Python [47].

- Linear Regression:

Linear regression is a type of regression analysis that models the relationship between a dependent variable and one or more independent variables. The aim of linear regression is to find the best-fit straight line that minimizes the sum of squared residuals, describing the relationship between the variables. The equation for a linear regression model can be written as Equation 5.[48]

$$y = \beta_0 + \beta_1 x_1 + \beta_2 x_2 + \cdots + \beta_n x_n + e \tag{5}$$

where y is the dependent variable, x_1, x_2, ..., x_n are the independent variables, β_0, β_1, β_2, ..., β_n are the coefficients, and e is the error term. The coefficients represent the effect of the independent variables on the dependent variable. The error term represents the variability in the dependent variable that cannot be explained by the independent variables.

- Polynomial Regression:

Polynomial regression is a regression analysis technique that enables the modeling of the relationship between a dependent variable and one or more independent variables using an nth-degree polynomial. It expands upon the concept of linear regression by introducing polynomial terms of the independent variables. By incorporating these additional terms, polynomial regression can capture nonlinear relationships and represent curves and non-linear patterns in the data. This technique can uncover hidden trends and capture the nuanced interplay between the independent and dependent variables. The resulting model

equation, represented by Equation 6, describes the polynomial regression model, and allows for flexible curve fitting to the training data points.[49]

$$y = \beta_0 + \beta_1 x_1 + \beta_2 x_2 + \cdots + \beta_n x_n + \beta_{1+1} x_1^2 + \beta_{1+2} x_1 x_2 + \cdots + \beta_{1+k} x_1^k + \cdots + e \quad (6)$$

Where the additional terms $\beta_{1+1} x_1^2$, $\beta_{1+2} x_1 x_2$, ..., $\beta_{1+k} x_1^k$ represent the higher-order iteration terms, capturing how the relationship between the two variables changes when they are considered together. It is worth mentioning that the choice of the polynomial degree (k) determines the complexity and flexibility of the model.

- Lasso:

Lasso, which stands for Least Absolute Shrinkage and Selection Operator, is a regularization technique used in linear regression to prevent overfitting. The lasso method adds a penalty term to the loss function, which is proportional to the absolute value of the coefficients. The effect of this penalty is to shrink the coefficients towards zero, effectively selecting only the most important features. Equation 7 is a description of the loss function with the L1 penalty term.

$$L = \|y - Xb\|_2^2 + \lambda \|b\|_1 \quad (7)$$

In another words, the main formulation consists in minimizing the formulation described in the following Equation 8.

$$Min \frac{1}{2 * n_{samples}} * L \quad (8)$$

Where y is the dependent variable, X is the matrix of independent variables, b is the vector of coefficients, and together, form the term $\|y - Xb\|_2^2$ that represents the ordinary least squares (OLS). The term λ is the regularization parameter that controls the strength of regularization, with higher values leading to stronger regularization, by tuning λ, it is possible to balance between fitting the training data well and maintaining simplicity in the model, and finally, $\|b\|_1$ represents the L1 regularization term.

Lasso regularization is particularly useful when dealing with high-dimensional data, where there may be many features but only a few are truly informative for predicting the target variable. It helps identify and prioritize the most important features for the regression task.[50]–[52]

- Ridge:

Ridge regression is another regularization technique used in linear regression to prevent overfitting. The ridge method adds a penalty term to the loss function, which is proportional to the square of the coefficients. The effect of this penalty is to shrink the coefficients towards zero, but not to zero. And this regularization term helps to control the complexity of the model and reduce the impact of multicollinearity between the input features. Equation 9 describes the loss function.

$$L = \|y - Xb\|_2^2 + \lambda \|b\|_2^2 \quad (9)$$

As Lasso, the main formulation consists in minimizing Equation 10.

$$Min \frac{1}{2 * n_{samples}} * L \quad (10)$$

Where y is the dependent variable, X is the matrix of independent variables, b is the vector of coefficients, and together, form the term $\|y - Xb\|_2^2$ that represents the ordinary least squares (OLS). This term measures the squared differences between the predicted values (Xb) and the actual target values (y), aiming to minimize the overall prediction error. Still, it is possible to mention the term (λ) is the regularization parameter that controls the strength of regularization, with higher values leading to stronger regularization, by tuning

(λ), it is possible to balance between fitting the training data well and maintaining simplicity in the model, and finally, $\|b\|_2^2$ represents the L2 regularization term.

Ridge differs from Lasso in that it does not force coefficients to become exactly zero. Instead, it reduces the impact of less important features by shrinking their coefficients towards zero, while still including them in the model. This method is particularly useful when dealing with datasets that exhibit multicollinearity, where there is a high correlation between input features. It helps reduce the sensitivity to multicollinearity and provides more stable and reliable coefficient estimates. From its use it is possible to note that by shrinking the coefficient values towards zero, Ridge helps improve the stability and generalization performance of the model. However, it does not perform automatic feature selection like Lasso. [53], [54]

- Elastic Net:

Elastic Net is a regularization technique that combines the strengths of Lasso and Ridge regression. The elastic net method adds both the L1 and L2 penalties to the loss function. The effect of this penalty is to shrink some coefficients towards zero (like Lasso) and others towards each other (like Ridge). Equation 11 is a representation for the loss function with the elastic net penalty term.

$$L = \|y - Xb\|_2^2 + \frac{\lambda(1-l1_{ratio})}{2}\|b\|_2^2 + \lambda l1_{ratio}\|b\|_1 \quad (11)$$

The objective function to minimize, as the previous cases is described by the Equation 12.

$$Min\frac{1}{2*n_{samples}} * L \quad (12)$$

The explanation of the terms of the formulation is kept from the previous topics, explaining Lasso and Ridge's parameters and regularization terms. Still, it is possible to include the explanation of the *l1_ratio* hyperparameter that determines the balance between L1 (Lasso) and L2 (Ridge) regularization. A *l1_ratio* of 1 corresponds to pure Lasso regression, while a *l1_ratio* of 0 corresponds to pure Ridge regression. By adjusting the values of λ and *l1_ratio*, you can control the trade-off between model simplicity, sparsity, and prediction accuracy. Elastic Net Regression combines the advantages of both Ridge and Lasso regression, providing a flexible approach that handles multicollinearity and performs feature selection simultaneously. This approach is useful for datasets with a large number of features, especially when some features are highly correlated. [51], [52], [55]

- Gaussian:

Gaussian Process Regression (GPR) is a powerful machine learning technique used for supervised learning tasks, such as regression and classification. It is a non-parametric, Bayesian approach that models the distribution of a function, which is typically used to predict the value of an output variable given input variables. The core idea of GPR is to represent a function as a Gaussian process, which is a collection of random variables, any finite number of which have a joint Gaussian distribution. In other words, a Gaussian process is a distribution over functions, rather than a distribution over individual values. This distribution is defined by a mean function and a covariance function. The mean function represents the expected value of the function, while the covariance function captures the degree of similarity between different points in the input space. GPR involves three key steps such as choosing a prior distribution over functions, conditioning the prior on observed data, and making predictions for new inputs based on the posterior distribution. The prior distribution captures our assumptions about the structure of the function before observing any data and can be chosen to be flexible or restrictive. The choice of prior is a crucial step in GPR, as it determines the range of functions that the model can generate.

Once having observed data, it is possible to condition the prior distribution on the data to obtain the posterior distribution. This is done using Bayes' rule, which involves multiplying the prior by the likelihood of the data given the function. The resulting posterior distribution over functions is a Gaussian process, with a mean and covariance function that has been updated to reflect the observed data. The final step in GPR is to make predictions for new inputs based on the posterior distribution. This involves calculating the mean and variance of the posterior distribution at the new input point. The mean represents the predicted value of the output variable, while the variance represents the uncertainty of the prediction. GPR is particularly well-suited for tasks where uncertainty estimation is important, as it provides a probabilistic prediction of the output variable.

In summary, Gaussian Process Regression is a flexible and powerful machine learning technique that models the distribution of a function using a Gaussian process. It provides a probabilistic prediction of the output variable, which is particularly useful for tasks where uncertainty estimation is important. The key steps in GPR involve choosing a prior distribution over functions, conditioning the prior on observed data, and making predictions for new inputs based on the posterior distribution.

Since this work is basing the possible regression approaches on the scikit-learn python library, it is possible to describe the practical usage of the Gaussian process regression. This process is implemented through the *GaussianProcessRegressor* class in the Gaussian Process module, where its steps can be defined in topics:

- Data Preparation: At this point it is necessary to retrieve the information data to be used as training set for the regression. It is important to ensure a proper data distribution using methods such as the previously mentioned Latin Hypercube Sampling (LHS) in this way it is possible to avoid biased predictions and not missing data in essential regions. The training data normally depends on the nature of each problem, but generally having more training data density represents more precision in the predictions, while it represents more computational cost.
- Model Initialization: After preparing the training data set, the model can be initialized. At his point an instance of the *GaussianProcessRegressor* class is created, this instance serves as the foundation for the Gaussian regression model. This phase is when it is possible to specify the hyperparameters to be used. As an example of the mentioned hyperparameters, the kernel function, that determines the shape and smoothness of the regression function. The noise parameters capture the level of noise in the data. And the alpha (α) parameter that controls the regularization strength in the regression helps to prevent overfitting.
- Kernel Selection: It is an important step to choose an appropriate kernel function that captures the underlying structure of the training data. scikit-learn provides a range of kernel options. The choice of kernel depends on the nature of your data and the assumptions to be taken about the relationship between the input and target variables. It is possible to shortly describe some of the common kernels and their formulation:

    - Radial Basis Function (RBF) Kernel (squared exponential kernel) is a popular choice for Gaussian process regression. It assumes that nearby points in the input space are likely to have similar target variable values. The length scale (l) parameter controls the smoothness and length scale of the correlations. The kernel is described in Equation 13.

$$k(x, x') = e^{-0.5 * \frac{\|x - x'\|^2}{l^2}} \tag{13}$$

    - The Matérn kernel is a flexible kernel that allows for varying levels of smoothness. The parameter υ controls the smoothness level, and length_scale

(l) controls the correlation length. When υ is set to infinity, the Matérn kernel reduces to the RBF kernel. The kernel is described in Equation 14, where gamma function ($\Gamma(\upsilon)$) is a generalization of the factorial function to non-integer values and K_ν is the modified Bessel function

$$k(x,x') = \left(\frac{1}{\Gamma(\nu)*2^{\nu-1}}\right) * \left(\frac{\sqrt{2*\nu}}{l} * \|x-x'\|\right)^{\nu} * K_\nu\left(\frac{\sqrt{2*\nu}}{l} * \|x-x'\|\right) \quad (14)$$

- The Rational Quadratic Kernel is a generalization of the RBF kernel that can capture both short-term and long-term correlations. The alpha parameter controls the smoothness of the correlations. The kernel is described by Equation 15.

$$k(x,x') = \left(1 + \frac{\|x-x'\|^2}{2\alpha l^2}\right)^{-\alpha} \quad (15)$$

- The Exponential Kernel assumes that the correlation between points decreases exponentially with their distance. It is useful when the target variable values change rapidly with small changes in the input variables. The kernel is represented by Equation 16.

$$k(x,x') = e^{-\frac{\|x-x'\|}{l}} \quad (16)$$

- The dot product kernel is a simple linear kernel that computes the dot product between the input variables. It is useful when the relationships between the input variables and target variables are expected to be linear. The kernel is represented by Equation 17.

$$k(x,x') = (x \cdot x') \quad (17)$$

It is important to highlight that each kernel has different properties and assumptions, and the choice of kernel depends on the characteristics of your data and the desired behavior of the regression model. It is often beneficial to experiment with different kernels and hyperparameters to find the best fit for the specific model.

- Model Fitting: After selecting the kernel to be used and the parameters of the process it is possible to fit the regression model to the training data. This step estimates the parameters of the model based on the provided data. The Gaussian process regression model learns the underlying patterns and relationships in the data, capturing the uncertainty in the predictions.
- Prediction: Once the model is fitted, it is possible to perform predictions of the new and unseen data, that will be the objective of analysis. The Gaussian process regression model estimates the target variable values for the given input variables. Additionally, it provides uncertainty estimates in the form of confidence intervals, which quantify the range of plausible predictions. These confidence intervals can be valuable for decision-making and understanding the reliability of the model's predictions.
- Model Evaluation: In order to assess the performance of the Gaussian regression model it is possible to use evaluation metrics such as mean squared error (MSE), mean absolute error (MAE), or coefficient of determination (R2). These metrics help to measure how well the model fits the training data and how well it generalizes to unseen data. Cross-validation techniques can also be applied to obtain more robust performance estimates. It is worth noting that these evaluations should be performed with seen data that was not used as training set.
- Hyperparameter Tuning: After verifying the performance of the model, it is possible to test different hyperparameter settings and kernel choices to optimize the model's performance. Hyperparameters, such as the kernel parameters and noise level, can significantly impact the behavior and accuracy of the Gaussian regression model.

By following these steps and iterating on the model training, prediction, evaluation, and hyperparameter tuning process, it is possible to effectively apply Gaussian regression using scikit-learn. This allows you to model and understand complex relationships in the data, make accurate predictions, and quantify the uncertainty associated with those predictions. It is important to mention that in case that after all the described steps the model still do not perform as expected, it is necessary to increase the density of training data as more complex models also require more information for obtaining a good performance. [56]–[58]

3. First Aircraft: Prototype Description

As mentioned before, the objective of this work is to produce a weight optimized carbon fiber wing for an UAV that will be used for medical delivery in remote areas of Nepal. The first step of this project was to size, design and manufacture a lighter weight prototype of a first aircraft for testing methodologies and obtaining flight logs from the real environment. Being this step relevant for the framework of this project, and not its focus, this section is dedicated to briefly presenting the produced First aircraft (Prototype).

3.1 Sizing of prototype for the first aircraft

Sizing an airplane refers to the process of determining the appropriate dimensions and specifications of an aircraft to meet the desired performance and mission requirements. This involves considering factors such as the desired range, payload capacity, speed, altitude capability, and fuel efficiency, among others. During the sizing process, various aerodynamic, structural, and propulsion systems are evaluated to ensure that they can support the required performance characteristics of the aircraft. Overall, sizing an airplane is a critical step in the aircraft design process, as it directly impacts the aircraft's capabilities, efficiency, and overall performance.

For starting this procedure, it is important to have into account the followed given requirements, that represents a simplification of the final desired product, but not losing the capability of proving the followed methodology and as mentioned before to extract real flight logs, thus producing a more optimized final product. From that it is important to have into account the considered requirements:

• Maximum speed: 200 km/h

• Cruise speed: 70 km/h

• Range at 3000m: 100 km

• Payload: 1 kg

• Gust wind: 80 km/h

• Weather: Rain, Snow and Low temperatures

• Powerplant: Electrical

• Wingspan: maximum of 3 m (multi-divided wing for transportation)

From the described requirements it was possible to size the airplane based on the weight estimation method which included power plant selection, wing geometry sizing, airfoil selection, tail sizing, stability analysis and structural analysis based on the obtained V-n diagram. The mentioned aircraft design procedures were based on [59]. For this present work, it will be summarized and presented the wing geometry sizing, airfoil selection and wing structural topology as the V-n diagram.

For choosing geometry, easy manufacturing was a decisive point to consider, where it was decided to use a rectangular wing geometry, which means following a constant chord along the span. From the belly-landing assumption, as for the rough terrain it was chosen the High Wing configuration, ideally full cantilever but at this point still being an option to be chosen after structural analysis. Having fixed the wingspan to 3 meters and understanding the idea of following an aircraft type glide, aiming more endurance and the ability of performing slower flights, it was considered the aspect ratio of 12. This decision was based on historical data of similar UAVs for this use. These assumptions resulted in a chord of 0.25 m. Still, for more geometric and aerodynamic considerations, the software XFLR5 was an important and decisive tool. Its use assisted in choosing the airfoil GOE 398_MOD (Figure 14), that was selected

having into account the necessity of cross-sectional space for the tubular spar and aiming to reduce the stall speed.

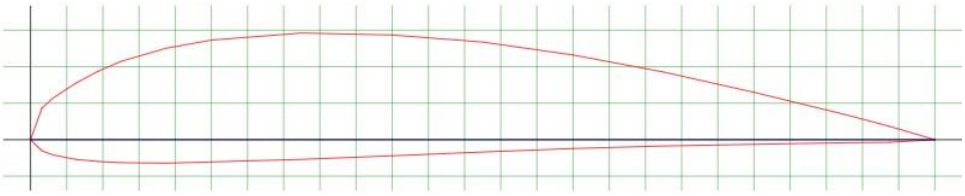

Figure 14 - GOE_398 Airfoil [60]

Finally, from the iterative sizing process based on weight estimation and on [61], a maximum weight of 9.8 kg was obtained and the aerodynamic coefficients from XFLR5 as the V-n diagram (Figure 15) for proceeding with structural analysis. Considering that the designed aircraft is expected to operate in challenging environmental conditions, and despite the cruise being at high altitude, the V-n diagram was generated using sea level altitude. This choice accounts for the higher air density, leading to increased aerodynamic loads and, consequently, a more conservative structural design for some load cases. To address the high gust wind conditions anticipated in the operational region, the maximum gust speeds specified in CS-VLA regulation [61] were utilized for the calculations.

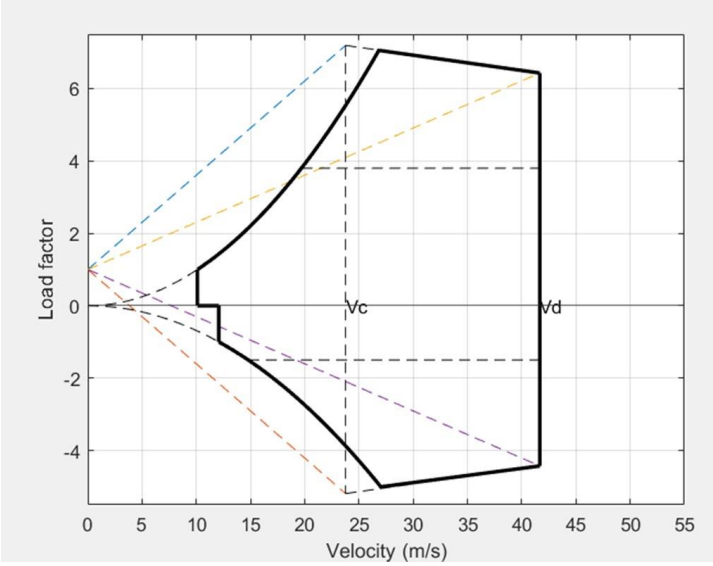

Figure 15 - V-n diagram for prototype (First Aircraft)

3.2 Design of first the first aircraft (prototype)

Based on the previously described sizing results, knowing that the wing has a 3 m span and 0.25 m of cord, being rectangular and positioned as high wing, its design and topology of the structural components were decided and presented in this subsection. Another important pre-defined factor to consider is that for transportation matters, the 3 m wingspan was divided into three panels of one meter each, being the central panel responsible for the wing connection and the tip panels symmetric to each other.

- Spars:

  It was chosen to use a single spar concept, and for simplification matters, to use tubular carbon fiber profiles that could be sized and ordered from a specialized company according to the specifications, saving time and ensuring more manufacturing quality. For sizing the spars, it was used both analytical, classical laminate theory, and Finite Element Analysis. Still, it is worth mentioning that, for safe design, it was considered that the main spar alone

would take all the aerodynamic loads. That hypothesis aligned to the quality factors and safety coefficients resulted in the sized tubes characteristics presented in Table 1. It is also worth mentioning that the available CFRP in the company are unidirectional in 300 g/m^2 and 160g/m^2 and woven 400 g/m^2.

Table 1 - Spar tubes characteristics

	N° of Layers per Orient/Mat. Density			Lenght	d_{int}	D_{ext}	Weight
	[+-45°]_400	[0°]_300	[0°]_160	[m]	[mm]	[mm]	[g]
Central Spar	1	4	3	1	18	22.24	230
Tip Spar	1	2	2	1	18	20.69	154.33
Carbon Rod	-	-	-	0.1	-	18	17.5

- Ribs:

  Considering the necessity of dividing the wing into three panels, it was chosen to use a 3 mm plywood rib in each side of the central panel as from the panel-to-panel connection side of each one of the two tip panels, also helping with the connection tip-central panels. In the tip of the wings, it is possible to find a 1 mm rib. Also, in the central panel there are two ribs of 10 mm plywood each, that are responsible for the wing to fuselage connection. It is worth mentioning that in between ribs the wing structure is filled by an XPS foam core that was also thought to mold the wing shape and receive the skin's woven carbon fiber cloth.

- Skin:

  It was chosen to use one layer of woven [0/90] of CFRP, covering the hole wing surface. It is worth mentioning that this layup came from the ABAQUS finite element analysis that considered the spar sized to sustain all the loading of the wing structure. In addition to the carbon fiber layer, it was decided to add another glass fiber layer for surface finishing purposes. This skin was molded by the internal foam core and applied through the hand layup procedure, avoiding the necessity of molds.

It is important to mention that the said dimensions and layups were defined based on finite element software ABAQUS analysis. Noting that due to multiple different materials and avoiding the use of multiple parts assembly, it was chosen to approach the problem subdividing it in smaller regions for analysis.

The result of the described wing design is shown in Figure 16 to Figure 20.

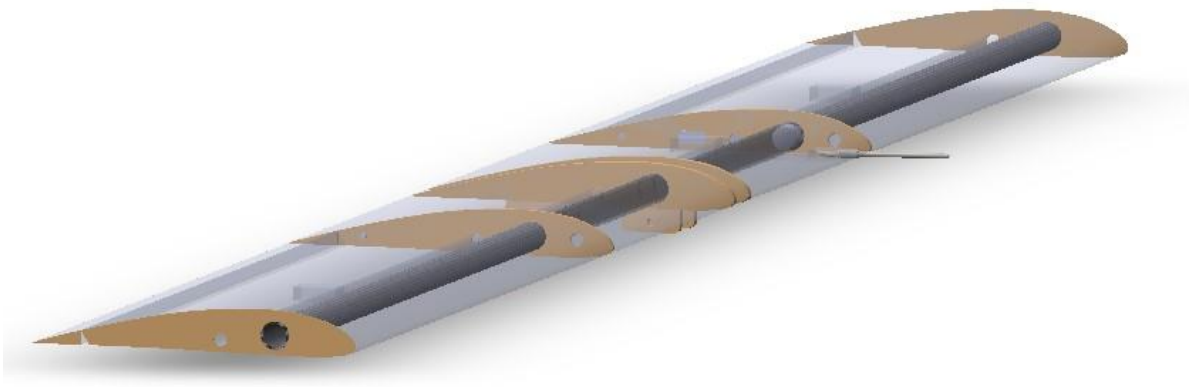

Figure 16 - Wing detailed design, view 1.

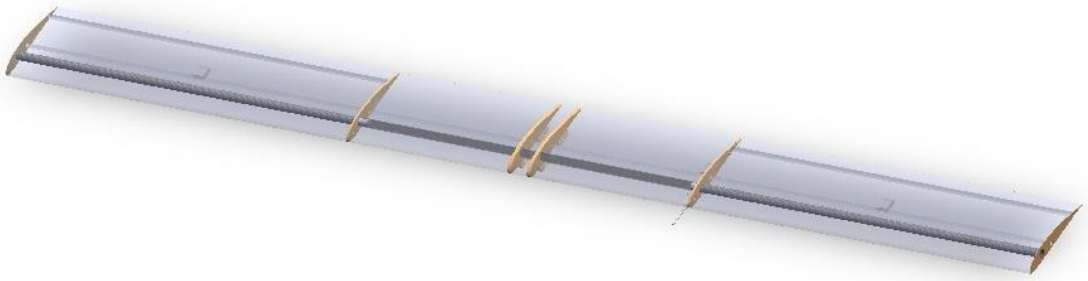

Figure 17 - Wing detailed design, view 2.

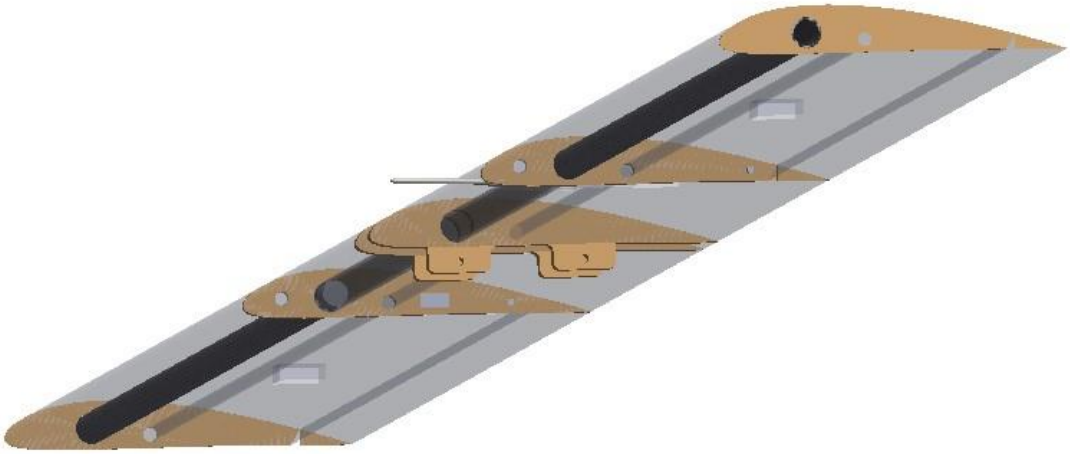

Figure 18 - Wing detailed design, view 3.

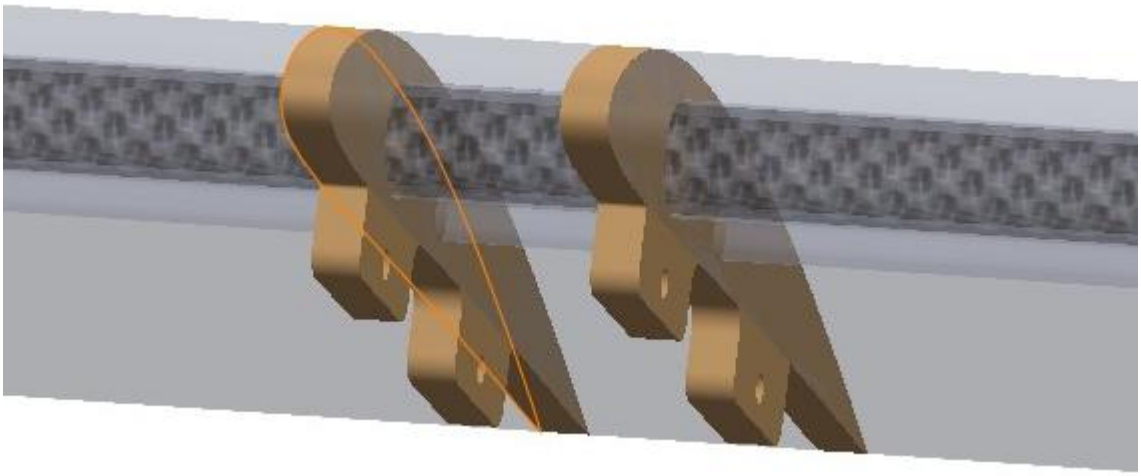

Figure 19 - Wing with fuselage connection (fittings)

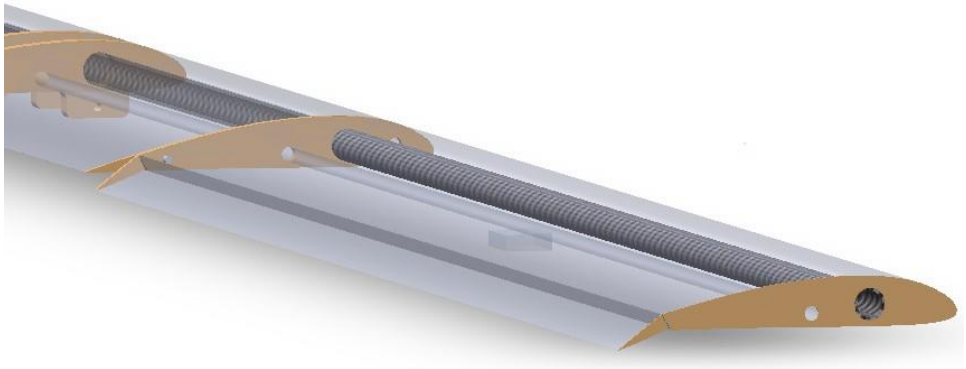

Figure 20 - Wing aileron design

Still, despite not being the focus of this work it is possible to present the fuselage design (Figure 21) that counts with ply-wood frames of 2, 2.5, 3 and 5 mm, 3d printed shell for molding the CFRP and Kevlar skin and the CFRP tube for tailboom connection.

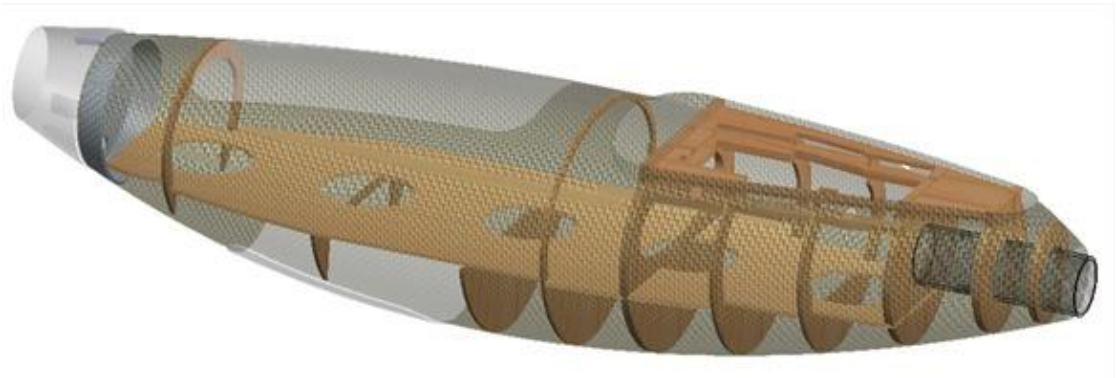

Figure 21 - Fuselage design

Finally, it is possible to present prototype complete design in Figure 22 and Figure 23.

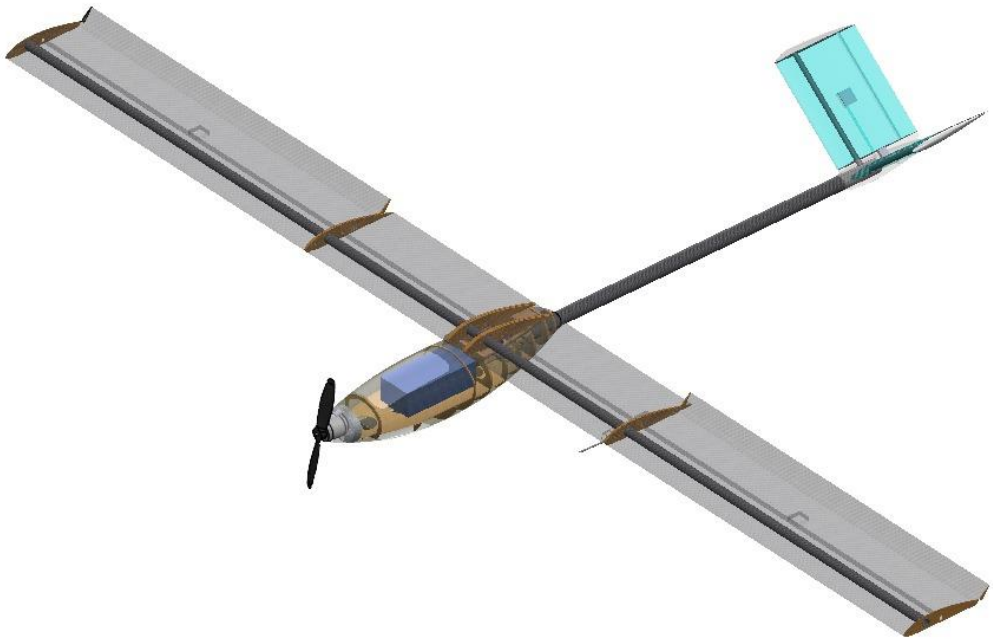

Figure 22 - Prototype's complete design, view 1.

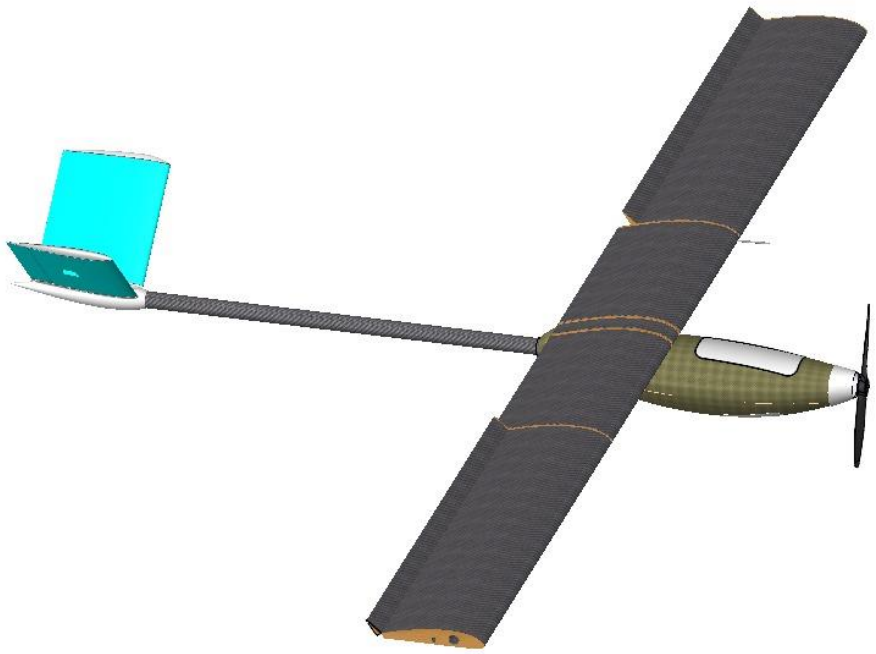

Figure 23 - Prototype's complete design, view 2.

3.3 Manufacturing process

The manufacturing process of the wing commenced with the precise cutting of the XPS foam core for the three panels. The selected airfoil shape was adhered to, while ensuring proper set-off for the skin. This cutting process was facilitated by employing a CNC hot wire cutter (Figure 24), which allowed for accurate and consistent results. Additionally, the machine was utilized to create the necessary openings within the foam core to accommodate the spars, taking into consideration their specified dimensions. Furthermore, wiring channels were incorporated during this stage to facilitate the installation of electrical components.

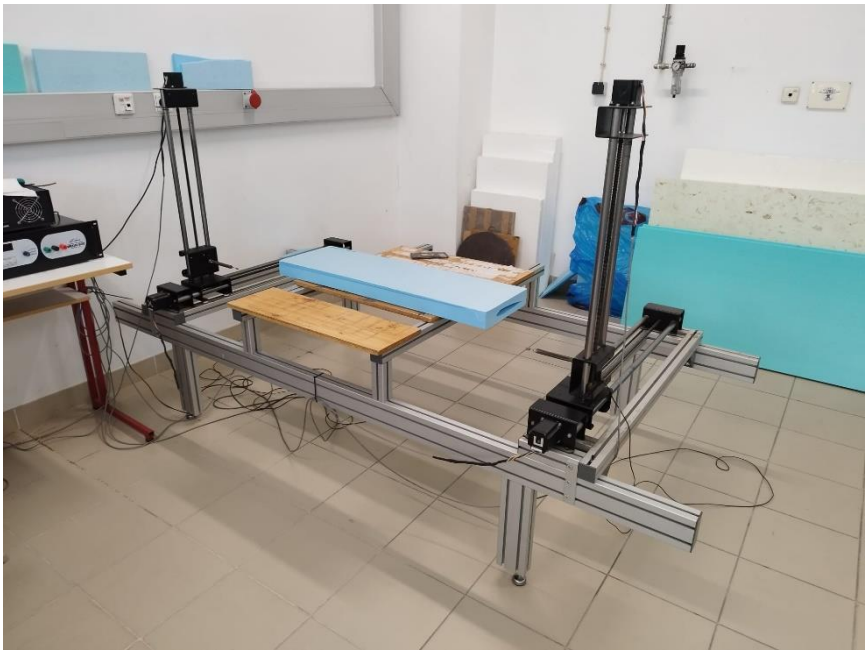

Figure 24 - CNC hot wire cutter from Universidade da Beira Interior (UBI)

The ribs were fabricated using a CNC laser cutting machine (Figure 25), which enabled precise and efficient cutting of the 1 mm, 2 mm, and 5 mm ply-wood sheets. The machine was calibrated to ensure accurate dimensions and to account for any offset that may be present. This offset consideration is crucial for maintaining the desired specifications and ensuring that the ribs are manufactured to the expected dimensions. By utilizing the CNC laser cutting machine, the rib fabrication process was optimized, resulting in accurate and consistent rib components for the wing structure, as it is possible to see in Figure 26.

Figure 25 - CNC laser cutting machine from UBI

Figure 26 - Central Ribs

After that, the spars were glued to their respective XPS foam and the plywood ribs, as in Figure 27.

Figure 27 - Wing Manufacturing - joining spar, foam core and ribs.

The carbon fiber cloth was carefully cut to cover both the pressure and suction surfaces of the wing skin. This involved cutting the cloth to the desired dimensions and shape, taking into account the curvature and contours of the wing. The cutting process ensured proper coverage of the entire surface area.

After cutting, the carbon fiber cloth was applied to the foam core using a hand layup process. This involved manually laying the cloth over the foam, ensuring proper alignment and smoothness. Care was taken to remove any air pockets or wrinkles during the layup process to ensure a strong bond between the carbon fiber and the foam core. This manual application allowed for precise placement and control, resulting in a well-adhered and uniform skin for the wing structure. The actual process can be seeing by Figure 28 and Figure 29

Figure 28 - Wing Manufacturing - Skin hand layup, 1.

Figure 29 - Wing Manufacturing - Skin hand layup, 2.

Additionally, it was decided to incorporate a glass fiber layer over the carbon fiber cloth for finishing purposes and to enhance the aerodynamic performance of the wing (Figure 30). This additional layer provides a smooth and visually appealing surface, reducing any imperfections and irregularities that may be present in the carbon fiber cloth. The glass fiber layer also helps to improve the overall durability and resistance to external elements such as moisture and abrasion. By combining the carbon fiber and glass fiber layers, a strong and aesthetically pleasing wing skin was achieved (Figure 31), ensuring both structural integrity and optimal aerodynamic characteristics.

Figure 30 - Wing Manufacturing - skin's glass fiber layer application

Figure 31 - Wing Manufacturing - skin's glass fiber layer

It is worth to briefly showing the fuselage manufacturing process. This process involved several steps to achieve the desired structure. Initially, a PLA shell was 3D printed to provide the outer shape of the fuselage. This shell served as the foundation for the internal components. The internal frames, made of plywood, were precisely cut using a CNC laser machine. These frames were then securely attached to the 3D-printed shell using epoxy glue, ensuring a strong and stable structure. Once the internal framework was in place, the multiple 3D-printed parts were connected to form the complete fuselage. On top of the 3D-printed skin, the stablished layup was applied using the hand layup method. This involved adding unidirectional 0°-oriented carbon fiber layers and one woven layer of Kevlar. The use of carbon fiber provided high strength and stiffness, while the Kevlar layer enhanced the fuselage's impact resistance. Additionally, an extra woven layer of Kevlar was incorporated in the bottom part of the fuselage as reinforcement for belly landings, offering increased protection during ground contact.

The manufacturing processes described above are visually depicted in the accompanying Figure 32 to Figure 36, providing a concise overview of the steps involved in creating the fuselage structure.

Figure 32 - Fuselage PLA Shell, frames, motor mounting and tailboom connection.

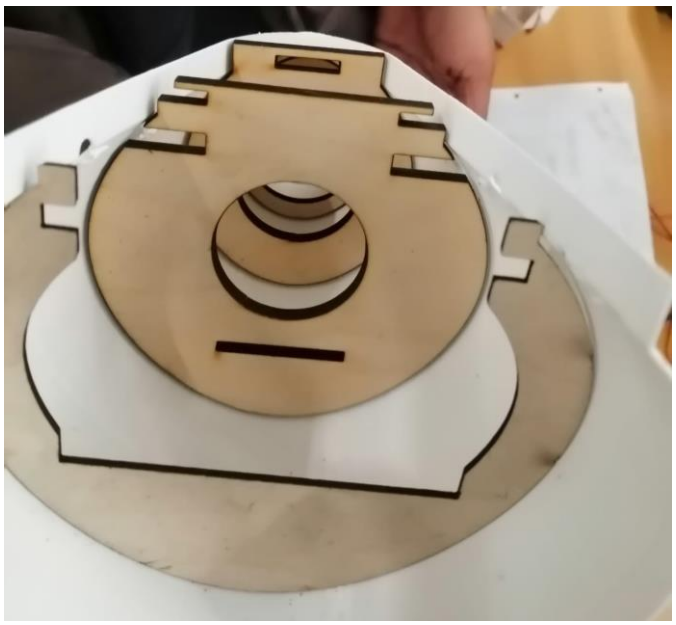

Figure 33 - Fuselage frames fitting.

Figure 34 - Fuselage PLA shell and frames assembly.

Figure 35 - Fuselage hand layup

Figure 36 - Fuselage skin, Kevlar layer.

3.4 Results of the manufacturing

Following the completion of the manufacturing process, it is possible to showcase the manufactured First Aircraft (Prototype) through a collection of photos. These images provide a visual representation of the results and offer a better understanding of the components described and discussed throughout the manufacturing journey.

- Wing [Figure 37 to Figure 41]:

Figure 37 - Wing tip panel with aileron.

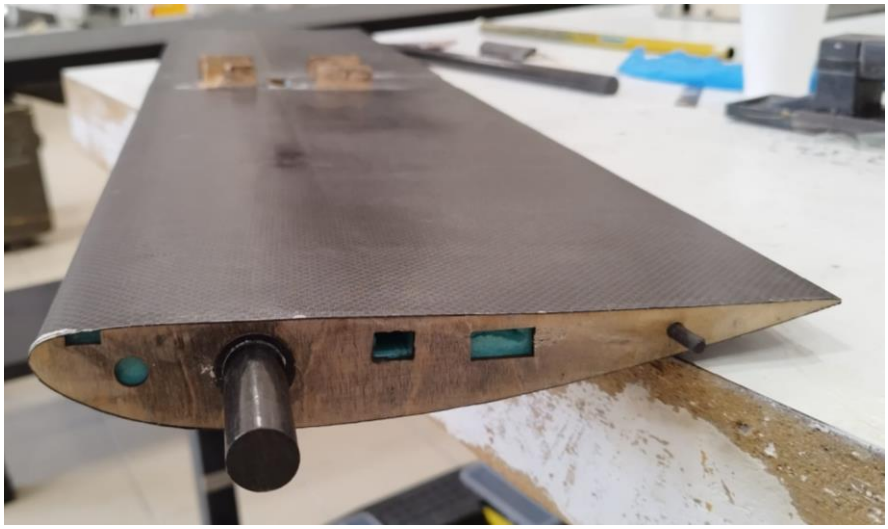

Figure 38 - Wing central panel with panel connection

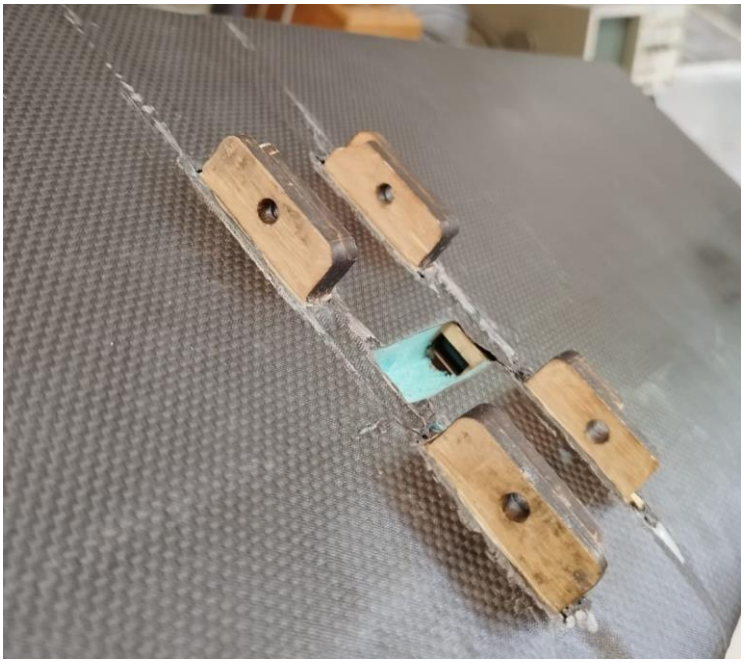

Figure 39 - Wing to fuselage connection

Figure 40 - Disassembled wing tip and central panels

Figure 41 - Complete wing assembled to fuselage.

- Fuselage [Figure 42 and Figure 43]:

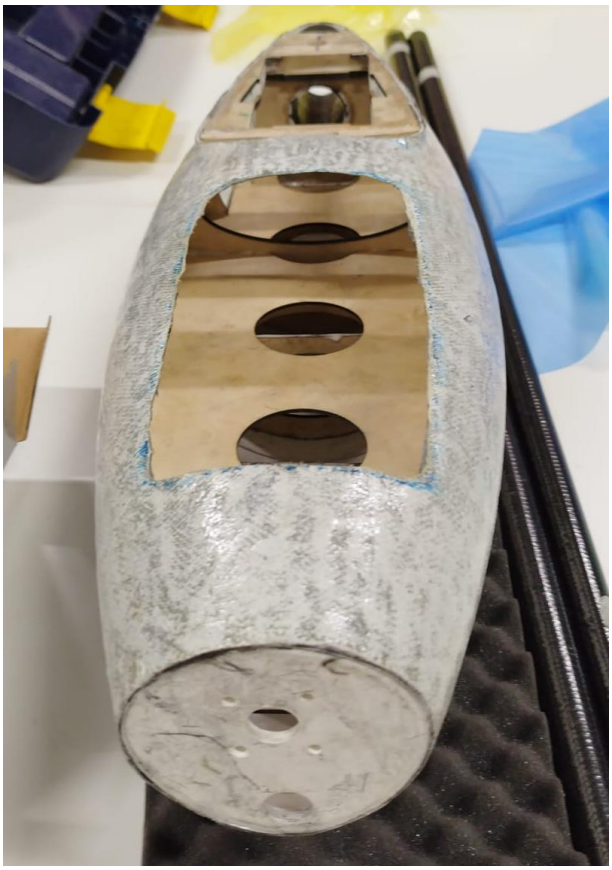

Figure 42 - Fuselage, view 1.

Figure 43 - Fuselage, view 2.

- Assembly [Figure 44 and Figure 45]:

Figure 44 - Assembled First Aircraft, view 1.

Figure 45 - Assembled Aircraft, view 2.

3.5 Flight test of the First Aircraft

Finally, the flight test was conducted to assess the performance of the aircraft and validate the applied methodologies. The results confirmed that the airplane operated as expected, demonstrating its capability to perform various maneuvers and flight tasks. This comprehensive evaluation allowed us to verify the aerodynamic stability, control response, and overall flight characteristics of the UAV. The successful completion of these maneuvers and flight tests provided strong validation for the design and manufacturing approaches employed. It also highlighted the areas of strength and identified potential areas for improvement in the next UAV model (Second Aircraft – Medical UAV). Moreover, the flight test phase enabled the acquisition of real flight data, which played a crucial role in refining the aircraft's performance and further optimizing its operational capabilities. Figure 46 to Figure 49 are photos from the test flight day.

Figure 46 - First Aircraft before take-off

Figure 47 - First Aircraft GPS calibration

Figure 48 - First Aircraft flying

Figure 49 - First Aircraft overflight

3.6 First Aircraft's Conclusions

It is possible to verify that the stability and maneuverability of the aircraft were found to be satisfactory during the flight test, affirming the effectiveness of the sizing and design choices made. The selected airfoil demonstrated favorable performance characteristics, making it a viable choice for the Second Aircraft (Medical UAV). Furthermore, the comparison between the sizing, predicted and measured Total Aircraft mass revealed that the weight was overestimated and represented a gain of around 1 kg in the First aircraft's payload. It is also worth noting that the wing structural weight played a significant role in the overall weight of the aircraft. The comparison between the predicted and measured wing structure, as well as the comparison with the historical data, demonstrated that the simplifications and assumptions made in the wing design resulted in a heavier wing structure (Table 2). However, the obtained weight ratios structural, avionics, and battery components are crucial for achieving better sizing prediction and optimization for the next UAV model. These findings will guide the future iterations and improvements in designing the second aircraft with enhanced performance and reduced weight.

Table 2 - Weight over different stages of the development of the first aircraft.

	W Sizing	W Design	W Measured
	[kg]	[kg]	[kg]
Central Panel	-	0.93	0.99
Tip Panels (each)	-	0.71	0.77
Aircraft Weight + PL	9.78	8.61	8.92

The completion of this step marks the progress towards the development of the Medical UAV (Second Aircraft), which presents an opportunity to explore more complex and resource-intensive structures. Building upon the lessons learned from the first aircraft, the objective of the next UAV will be to further optimize the wing's structural weight in relation to the MTOW (Maximum Takeoff Weight). By focusing on reducing the wing structural weight/MTOW ratio, the aim is to achieve a more efficient and lightweight wing design for the Medical UAV. This ongoing work strives to push the boundaries of weight optimization in order to enhance the aircraft's overall performance and payload capabilities.

4. Second Aircraft: Medical UAV Description

4.1 Sizing of Medical UAV

Having successfully validated the methodology using the First Aircraft (prototype), the development of the second aircraft, intended for medical delivery applications, can now be pursued. Building upon the insights gained from the data collected during the first aircraft's testing phase, improvements have been made to the existing codes, allowing for the generation of new reference parameters to guide the production of a more optimized structure. In designing the second aircraft, the objective is to maintain as much of the configuration used in the first aircraft as possible, while addressing the requirement of carrying a larger payload. This continuity in design helps leverage the knowledge and lessons learned from the first aircraft (prototype), ensuring a smoother transition to the new model while incorporating necessary enhancements. To further clarify the objectives and guide the design process of the second aircraft, new requirements have been identified. These requirements serve as key considerations for optimizing the aircraft's performance, payload capacity, and operational efficiency. By establishing these requirements from the outset, the design team can focus on developing a tailored solution that meets the specific needs of the medical delivery application. In the following sections, the new requirements will be outlined and discussed in detail, providing a clear direction for the design and development of the second aircraft. This iterative approach, informed by real-world data and the lessons learned from the first aircraft, will help ensure the success of the medical delivery application while maintaining the core attributes that proved successful in the prototype. For starting it is possible to present some of the new requirements:

• Maximum speed: 200 km/h

• Cruise speed: 120 km/h

• Range at 5000m: 150 km

• Payload: 5 kg

• Gust wind: 80 km/h

• Weather: Rain, Snow and Low temperatures

• Powerplant: Electrical

Based on the specified requirements, the sizing of the airplane was conducted using methods outlined in Section 3.1. This process encompassed power plant selection, wing geometry sizing, airfoil selection, tail sizing, stability analysis, and obtention of the V-n diagram for proceeding with the structural analysis. For this work, this process will be summarized to present the results from the sizing process.

To ensure consistency and facilitate data collection from real flights, the decision was made to maintain the wing configuration identical to that of the previous aircraft prototype. This includes preserving the same geometry, airfoil, chord, and span. Retaining the same wing design allows for the collection of accurate aerodynamic data during flight tests and improves the accuracy of the sizing process by reducing approximations. By maintaining consistency in the wing configuration, it becomes possible to build upon the knowledge gained from the previous aircraft and leverage it to refine the sizing process. This approach ensures that the aerodynamic characteristics and structural behavior of the wing are well understood and can be applied to the subsequent design iterations.

From the sizing process, it was possible to obtain the following reference values and the V-n diagram (Figure 50):

- MTOW: 24 kg

- $W_{structural}$: 11.7 kg
- V_{stall}: 24.63 m/s
- $V_{take\text{-}off}$: 27.10 m/s
- V_{climb}: 29.56 m/s
- Wing angle of incidence: 2°
- Wing Loading: 31.13 kg/m2
- Battery Capacity: 40000 mAh
- $Range_{@Vcruise}$: 150 km
- $Endurance_{@Vcruise}$: 1.19 h
- V-n Diagram:

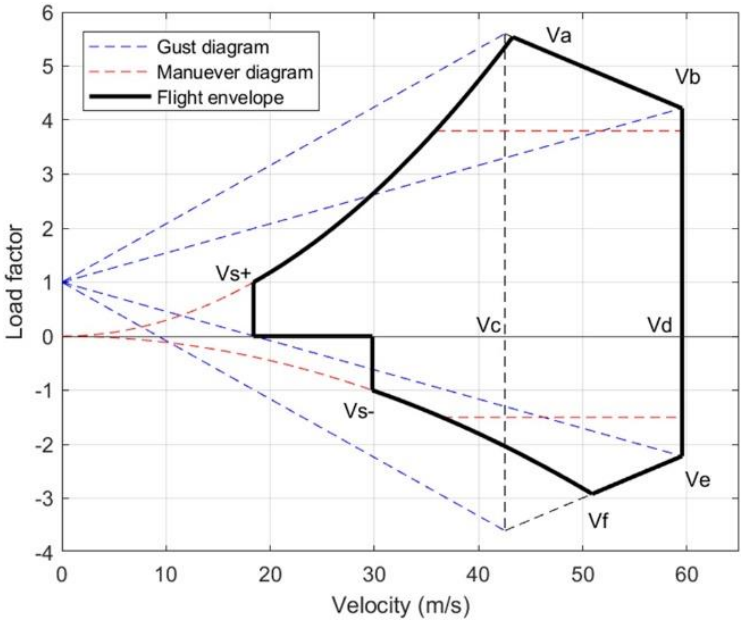

Figure 50 - V-n Diagram Second Aircraft (Medical UAV)

As with the first aircraft (prototype), the second aircraft is expected to operate under similar challenging environmental conditions. Consequently, the generation of the V-n diagram followed the same foundational assumptions. The air density was assumed to be at sea level to account for higher aerodynamic loading, resulting in a more conservative structure. The gust conditions were derived from the CS-VLA regulation [61], with the maximum gust speed from the gust plots selected for the calculations. Lastly, the previously outlined aircraft characteristics, such as MTOW and cruise speed, were taken into consideration. It is worth mentioning that these assumptions are expected to be actualized with real flight data in future iterations.

4.2 Load Case

The structural analysis of an aircraft involves evaluating the loads and stresses experienced by its components under different flight conditions. One crucial aspect of this analysis is considering the load cases derived from the V-n diagram (Figure 50 - V-n Diagram Second Aircraft (Medical UAV)Figure 50). The V-n diagram depicts the aircraft's safe operating limits in terms of velocity (V) and load factor (n), providing a valuable tool for determining the critical flight conditions that the structure must withstand. This diagram consists of a plot that illustrates the maximum permissible load factors for various airspeeds. By considering the aircraft's maximum operational limits, the diagram helps identify specific load cases that generate

significant loads on the structure. Load cases can include steady-state maneuvers like level flight, climb, or descent, as well as dynamic events such as gust occurrences.

Normally it is necessary to analyze multiple load cases to comprehensively assess the structural integrity of the aircraft. Each load case represents a specific flight condition or event that can impose unique loads and stresses on the structure. By considering a range of load cases, including those that represent critical maneuvers or gust encounters, it is possible to ensure that the structure is robust enough to withstand a variety of scenarios. However, for the scope of this work of developing an optimization tool for minimizing the structural weight of the composite layup of the wing, it is possible to choose between many of the critical load cases for analysis. From the V-n diagram (Figure 50) obtained from the sizing process, it is possible to note that a strong candidate for most critical load case would be the upper corner of the diagram, point A, where the stall curve matches the gust line, highlighted in a red point in Figure 51. At this point, it is possible to find a load factor of 5.5 at velocity *Va* = 43.3 m/s, close to cruise speed.

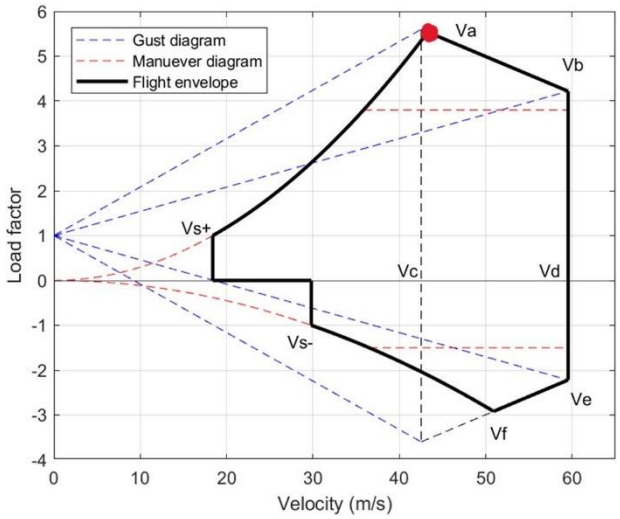

Figure 51 - Selected load case, V-n diagram.

Having selected this load case and knowing the MTOW of the aircraft and the dimensions and geometry of the wing, it is possible to perform an aerodynamic analysis in XFLR5 with the objective of obtaining aerodynamic loads. Still, it is important to mention that it was chosen to proceed with this analysis assuming the air conditions at sea level, since there is more availability of data for the airfoils and with the increment of air density, it is possible to observe the increment of the aerodynamic loads, resulting in a more conservative structure. Table 3 presents the parameters used for the next steps of the aerodynamic analysis.

Table 3 - XFLR5 input data

MTOW	24 kg
Airfoil	GOE_398
Chord	0.25 m
Span	3 m
Taper Ratio	1
Velocity	43.3 m/s
Altitude	Sea level

Before proceeding to analysis, it is still necessary to determine the angle of attack of the wing in the chosen load case. For that it is important to highlight that this point represents a pre-stall condition, thus, this angle is the critical angle of attack at velocity *Va* and sea level altitude, that presents the maximum lift coefficient (*Cl*). For determining this angle, it was chosen to proceed with two approaches. The first one is to appeal to the XFOIL database prediction from [62], that provides aerodynamic data of a large 2D airfoil library. From there,

and inputting the previously mentioned parameters, it was possible to obtain Figure 52, that presents the *Cl* vs α, where it is possible to verify that the maximum *Cl* occurred around 15°.

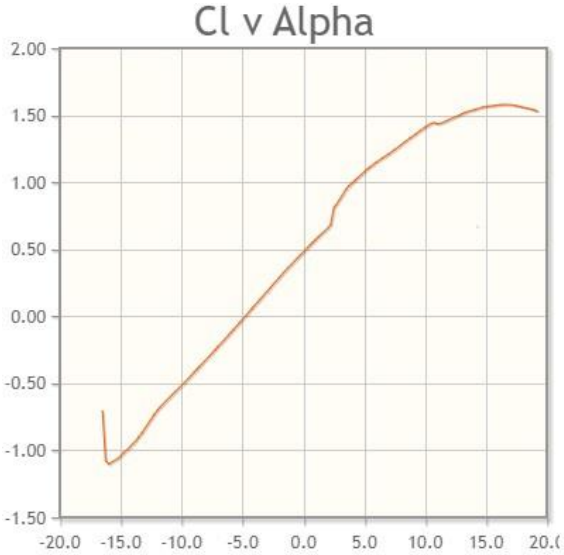

Figure 52 - Cl vs angle of attack _ GOE 398 [62]

The other approach, to confirm this information, was to perform in XFLR5 a LLT (Linearized Lift Theory) 3D wing analysis, considering the wing alone. This mentioned analysis is based on linearized potential flow theory, and it is a simplified approach to determine the aerodynamic characteristics of a wing by linearizing the flow equations around a reference condition. From performing this simulation, varying the angle of attack in a step of 0.5, it was possible to find the maximum *Cl* of 1.438 at 15°, which confirms the plot presented in Figure 52. However, it is important to acknowledge that both data obtained from computational methods are approximations with inherent numerical errors. While these analyses provide valuable insights and are widely used in the initial stages of wing design, it is recognized that more precise and reliable data can be obtained through wind tunnel testing. The following Figure 53 is a representation of the performed analysis in XFLR5.

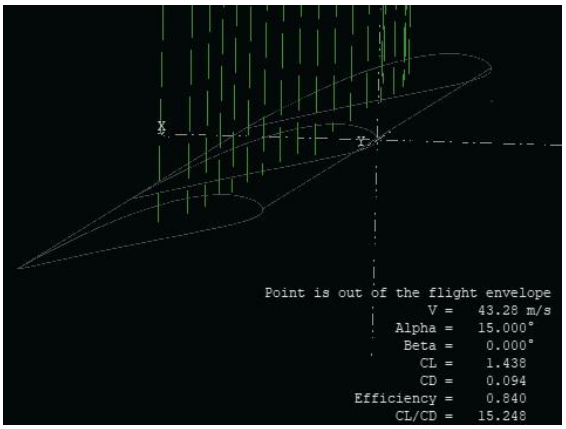

Figure 53 - XFLR5 – LLT analysis

After this definition, using the same software, it is possible to proceed using a 3D Panel inviscid analysis for estimation of lift, drag and pitching moment. This analysis in XFLR5 is based on a panel method, which discretizes the wing surface into a series of panels. Each panel represents a small section of the wing's surface and is treated as a source of potential flow. The method takes into account the wing's geometry, including its planform shape, twist, and camber, to calculate the flow field around the wing. During the analysis, XFLR5 solves the potential flow equations, typically using the panel method coupled with the vortex lattice method (VLM)

for improved accuracy. The software considers the flow-induced effects, such as lift, induced drag, and pitching moment, by solving for the circulation distribution along the wingspan. Figure 54Figure 54 - XFLR5, 3D panels at 2° incidence (Lift, Drag and Pitching moment) to Figure 56 presents the XFLR5 graphical representation for the lift, drag and pressure distribution for the cruise condition, incidence of 2°.

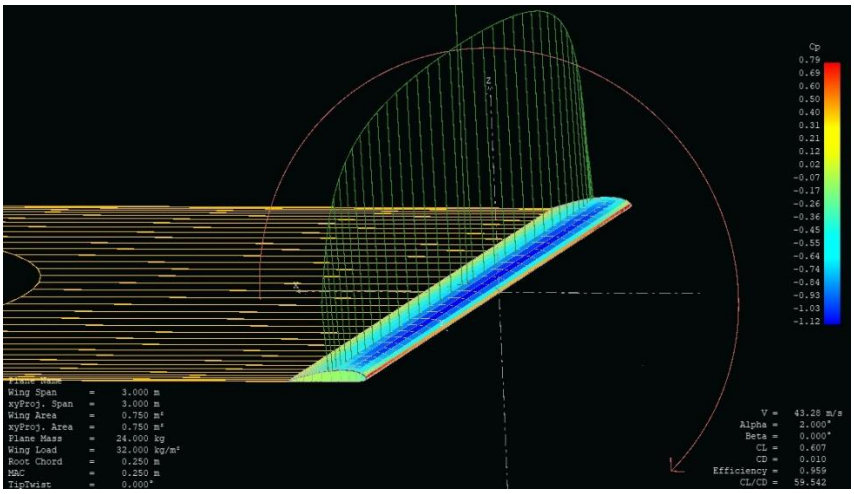

Figure 54 - XFLR5, 3D panels at 2° incidence (Lift, Drag and Pitching moment)

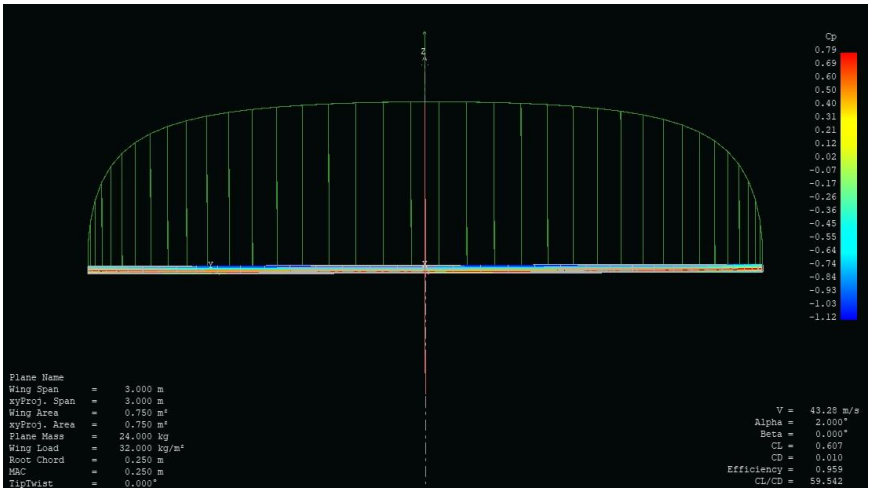

Figure 55 - XFLR5, 3D panels at 2° incidence (Lift)

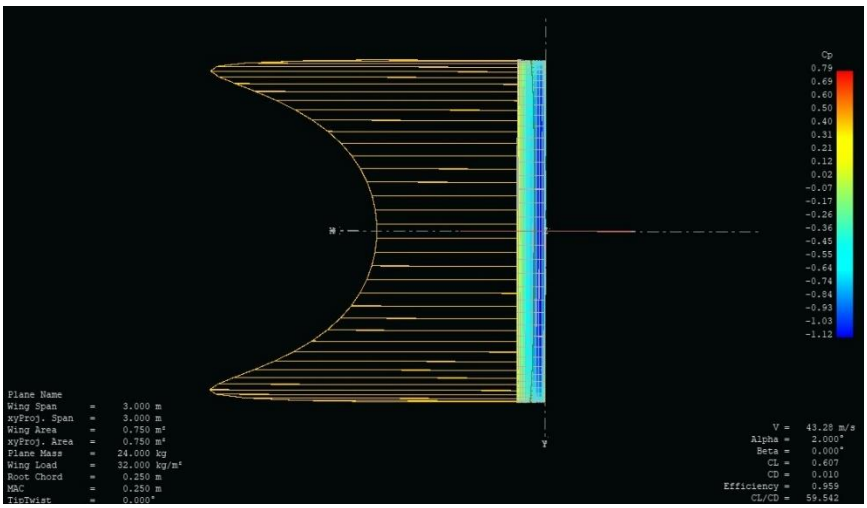

Figure 56 - XFLR5, 3D panels at 2° incidence (Drag)

By focusing on the selected load case, where the wing has an angle of attack of 15°, from the 3D Panel analysis, it is also possible to present the lift and drag along the span in addition to the pressure distribution in the wing surface on Figure 57 and Figure 58, XFLR5 representations.

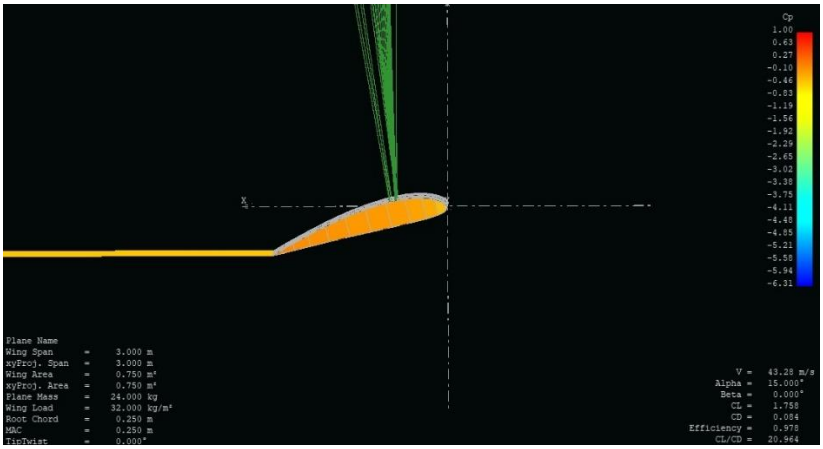

Figure 57 - XFLR5 3D Panels representation for 15° incidence, side view 1.

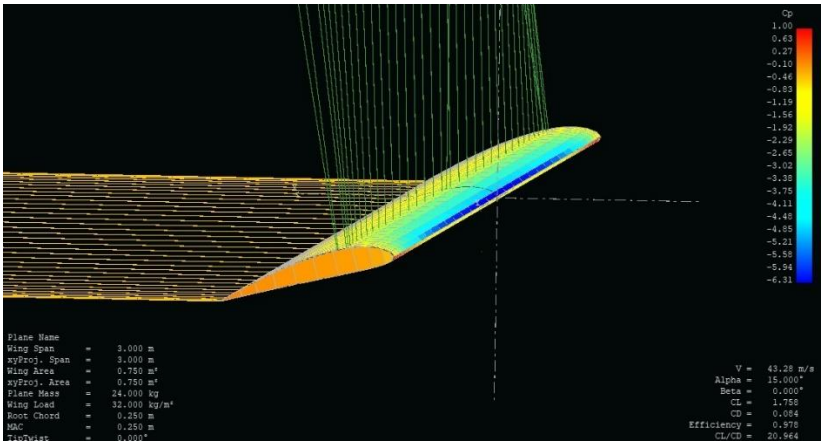

Figure 58 - XFLR5 3D Panels representation for 15° incidence, view 2

Despite having the pressure distribution from the 3D Panel analysis, it was chosen to proceed the aerodynamic loads calculation based on the lift, drag and pitching moment coefficients (*Cl*, *Cd* and *Cm*) obtained from the previously defined 15° of angle of attack, related to the wing alone, or 13° when considering the airplane reference, for the initial wing's angle of incidence of 2 degrees. The obtained data along the semi-span is present in Table 4.

Table 4 - XFLR5 data for *Cl*, *Cd* and *Cm* along the semi-span

Span [m]	Cl	Cd	Cm@25%c
0.0619	1.8678	0.0603	-0.0934
0.1854	1.8645	0.0609	-0.0932
0.3076	1.8578	0.0623	-0.0930
0.4276	1.8473	0.0645	-0.0925
0.5448	1.8326	0.0673	-0.0919
0.6582	1.8128	0.0711	-0.0910
0.7672	1.7871	0.0757	-0.0898
0.8709	1.7542	0.0812	-0.0881
0.9686	1.7123	0.0876	-0.0859
1.0598	1.6596	0.0947	-0.0829
1.1436	1.5934	0.1023	-0.0788
1.2197	1.5110	0.1098	-0.0733
1.2875	1.4091	0.1162	-0.0660
1.3464	1.2847	0.1200	-0.0563
1.3962	1.1352	0.1196	-0.0445
1.4364	0.9596	0.1130	-0.0319
1.4668	0.7589	0.0989	-0.0238
1.4872	0.5382	0.0777	-0.0381
1.4974	0.3175	0.0546	-0.0268

From the obtained data it is also possible to obtain the lift, drag and pitching moment per unit of span based on the formulation described in Equation 18 to Equation 22.

$$q = \frac{1}{2}\rho V^2 \tag{18}$$

$$vz_i = q * \frac{c(Cl_i + Cl_{i+1})}{2} \tag{19}$$

$$vx_i = q * \frac{c(Cd_i + Cd_{i+1})}{2} \tag{20}$$

$$My_i = q * c * -(Cm_{i+1} + Cm_i) \tag{21}$$

$$my_i = \frac{My_{i+1} + My_i}{2(y_{i+1} - y_i)} \tag{22}$$

The following Table 5 presents the essential aerodynamic loadings *my* [N], vz [N/m] and *vx* [N/m] for further calculations of forces to be applied to the finite element model.

Table 5 - Calculated *My* [N*m], *my* [N], *vz* [N/m] and *vx* [N/m]: Aerodynamic loadings.

Span (y) [m]	My [N*m]	my [N]	vz [N/m]	vx [N/m]
0.0619	26.780	216.685	535.265	17.382
0.1854	26.741	218.504	533.831	17.679
0.3076	26.661	221.643	531.364	18.182
0.4276	26.534	225.606	527.745	18.902
0.5448	26.349	231.225	522.798	19.852
0.6582	26.093	237.792	516.280	21.047
0.7672	25.745	245.995	507.867	22.498
0.8709	25.274	255.436	497.141	24.205
0.9686	24.638	265.433	483.575	26.147
1.0598	23.777	276.780	466.521	28.261
1.1436	22.611	286.761	445.210	30.422
1.2197	21.034	294.641	418.778	32.406
1.2875	18.920	297.799	386.328	33.872
1.3464	16.161	290.488	347.051	34.359
1.3962	12.772	272.564	300.421	33.347
1.4364	9.143	262.471	246.444	30.390
1.4668	6.816	435.106	186.017	25.333
1.4872	10.937	913.531	122.722	18.968
1.4974	7.699			

Figure 59, Figure 60 and Figure 61 displays the per unit of span values for lift, drag, and pitching moment. Notably, in Table 5, the pitching moment per unit span (*my* [N]) values show an increasing trend towards the wingtip, which can be attributed to the reduction in the span interval provided by XFLR5. To account for this, the pitching moment plot in Figure 61 was constructed by dividing the pitching moment (*My* [N*m]), obtained by interpolation, by an equally distributed interval. It is important to consider this adjustment in order to accurately interpret the pitching moment distribution along the wingspan and gain insights into the aerodynamic characteristics of the wing.

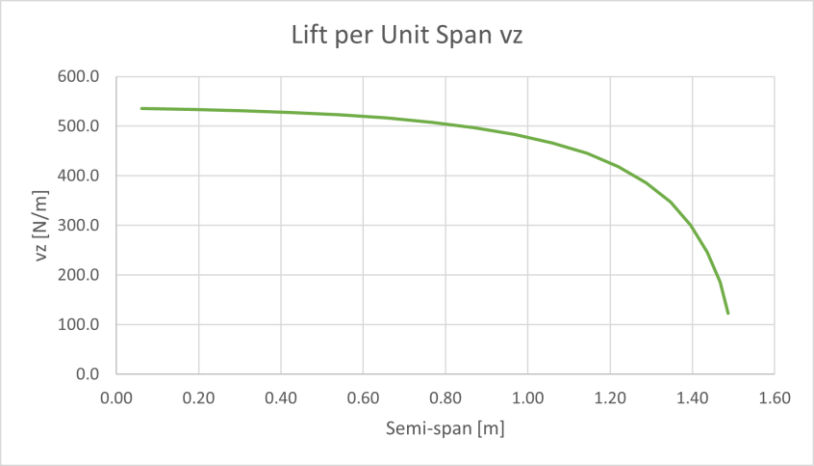

Figure 59 - Lift per unit span (*vz* [N/m])

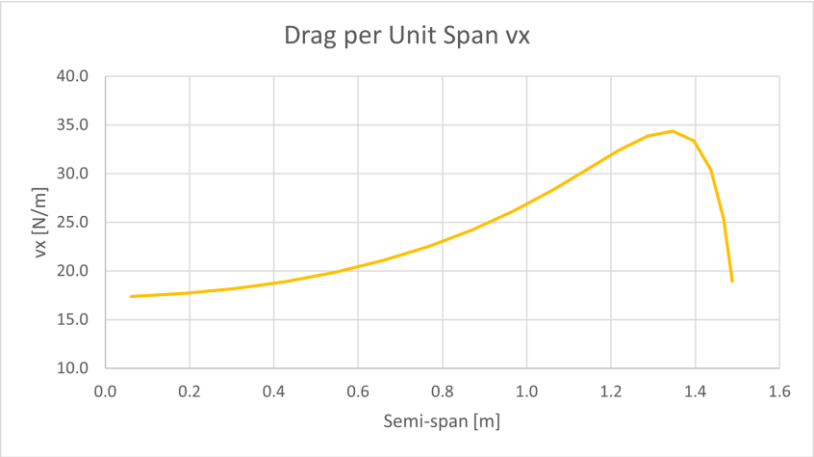

Figure 60 - Drag per unit span (*vx* [N/m])

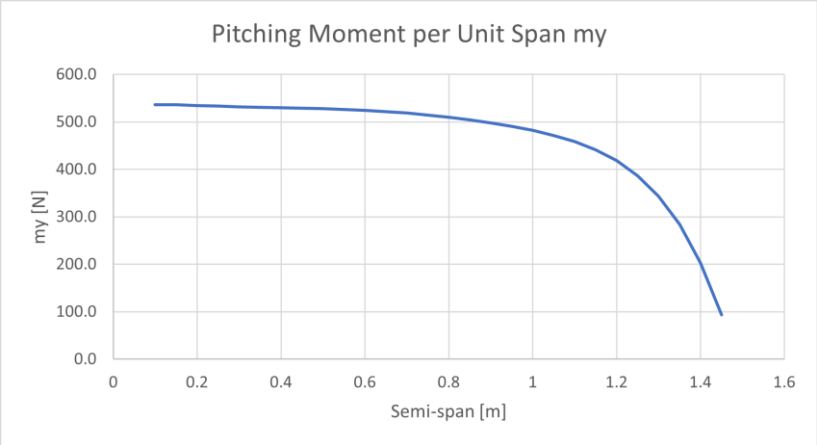

Figure 61 - Pitching Moment per unit span (*my* [N])

It is important to mention the inertial loads that are of paramount importance in the structural analysis of aircraft. In the selected case, the vertical load factor reaches 5.5 times the gravitational acceleration, indicating a substantial multiple of the aircraft's weight experienced during flight. When considering the wing analysis, with the boundary conditions in the root, this type of loading is represented by the wing's own structural weight. Additional considerations, such as the horizontal load factor and the load application, will be comprehensively elaborated in Section 6.2.5 to provide a detailed understanding of the inertial loads affecting the wing structure.

4.3 Wing design: Topology, Number of spars and ribs

In the context of the optimization process, it is essential to consider the topology of the structural elements. However, for the specific objectives of this project, the primary focus is on optimizing the composite layup. As a result, certain aspects related to the structural topology have been intentionally selected and fixed to facilitate the layup optimization.

To ensure appropriate structural support and consider aerodynamic factors, such as the distribution of forces to be applied to the finite element model, a rib spacing of ¼ of the chord length, representing 62.5 mm space between ribs, was deemed suitable and adopted. These spacing strikes a balance between structural integrity and aerodynamic load distribution. In addition to that, it was defined arbitrary holes for weight reduction and as a means of passing electrical wiring. These assumptions are graphically represented in Figure 62 and Figure 63.

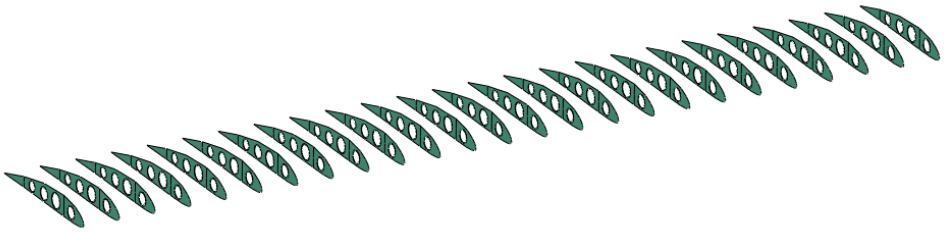

Figure 62 - Rib spacing

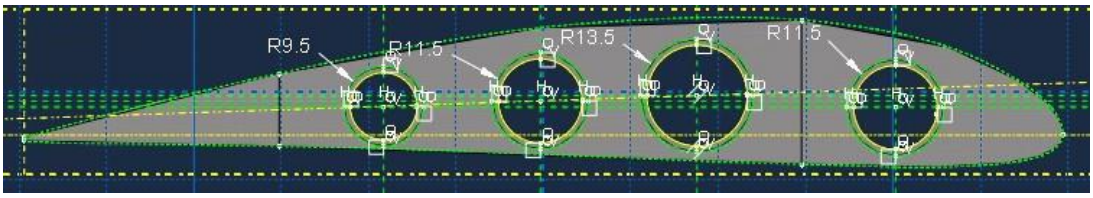

Figure 63 - Rib Holes

The positioning of the main spar was determined to be at 25% of the chord length, taking into account the airfoil characteristics, particularly the increased thickness typically found in that region. This position was maintained based on the initial prototype's definition. It is worth noting that the positioning of the main spar at 25% of the chord is also influenced by the point of application of aerodynamic loads. This strategic placement ensures that the main spar efficiently handles the bending and torsional forces experienced during flight, as it aligns with the location where aerodynamic loads are typically concentrated. Despite this supposition, it is important to acknowledge that, ideally, the main spar's optimal position would be located before the aerodynamic center, for the conventional two spar configuration. However, for the purposes of this project and as an initial estimation, the main spar position was kept as previously described. Furthermore, to enhance structural integrity and support, a secondary spar was introduced at 75% of the chord length. The addition of the secondary spar further reinforces the wing structure. These structural elements are represented in Figure 64. Figure 65 presents the wing in the airfoil view, where it is possible to verify the main and secondary spar positioned in the vertical lines.

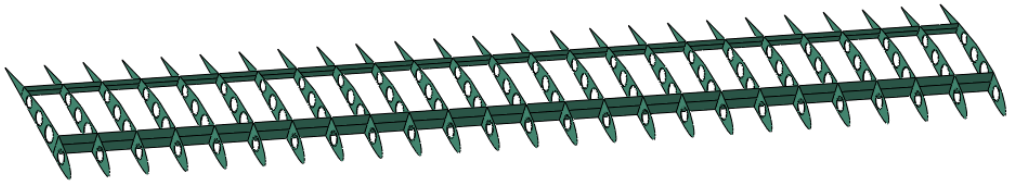

Figure 64 - Ribs, Main and Secondary Spars.

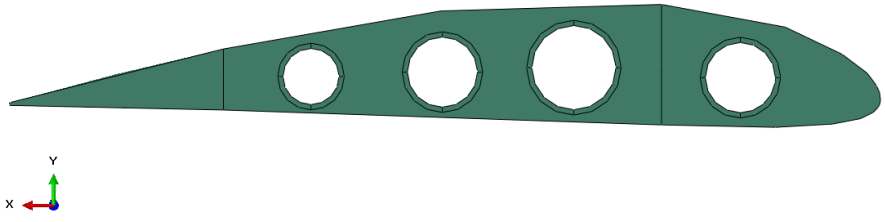

Figure 65 - Wing airfoil view

By establishing these fixed parameters for the rib spacing and spar positions, the project can concentrate its efforts on optimizing the composite layup for the wing structure. This approach allows for a targeted optimization process that considers specific design considerations and constraints, while also accounting for the essential role of structural topology in achieving an efficient and high-performance wing design.

Figure 66 and Figure 67 are final representations of the wing design.

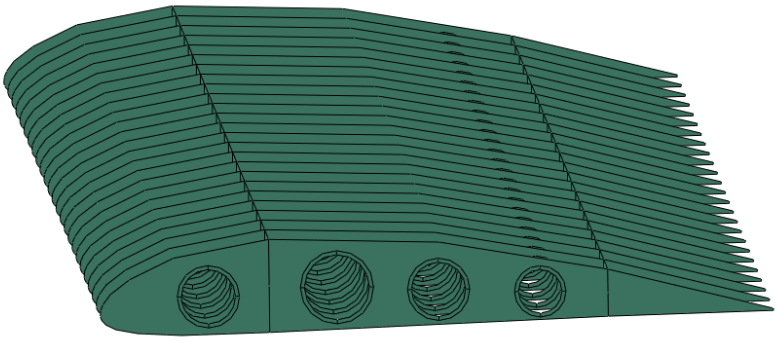

Figure 66 - Wing structure without skin

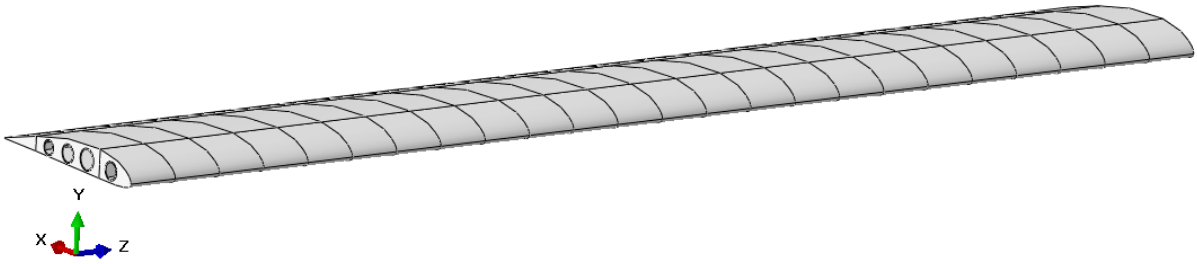

Figure 67 - Final model with reference coordinate axis

5. Optimization Tool

5.1 Idealization of the Optimization Tool

This subchapter starts with the idealization of the computational tool for the optimization of the carbon fiber wing structure. Being the objective to optimize the weight of the structure, it is easily possible to define the objective function of the optimization problem as a function stablishing the relation between the weight of the structure and the number of layers in each section, and it is possible to conclude that the number of layers in each section is directly and linearly related to the weight of the structure.

Having established the objective function of the optimization process, it is important to have a good understanding of the constraints, one of them is the evaluation of the validity of each layup, it means eliminate penalizing the results that present failure in the laminate. For that, the previously mentioned Finite Element Software ABAQUS can be used, where it can simulate the given layup and return the Tsai-Hill values for each layer of the layup, working in this case as "Black-box" for imputing layups and returning its failure indexes. The initial idealization of the computational tool can be presented in the following flow chart described in Figure 68.

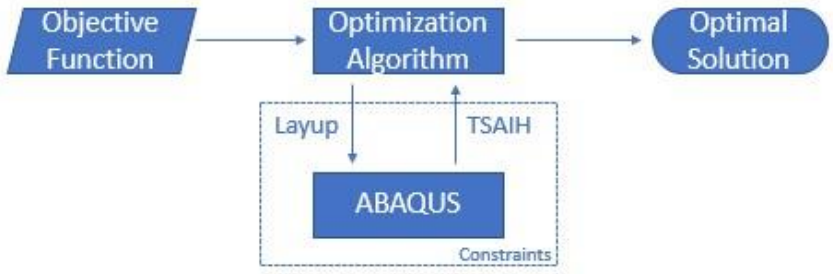

Figure 68 - Flow chart, initial idealization of the computational tool

5.2 Genetic Algorithm

5.2.1 Introduction

Based on the literature review, the GA was chosen as optimization algorithm to be used for the developed computational tool, since it is a suitable choice for optimizing the number of layers in a composite structure due to its ability to handle a large solution space, number of variables, constraints, and non-linearity.

Having selected the optimization algorithm, it is possible to start the development of the GA based on [38] with an elitist strategy of keeping the best individuals for the new randomly generated populations. The development of the genetic algorithm counts with adapting the code for this specific work of optimizing the weight, based on the number of layers of different sections of the Medical UAV wing structure. As previously defined, this is a single objective optimization, where the weigh minimization is the objective, and the failure of the laminate are the main constraints.

5.2.2 Objective Function

As previously mentioned, the objective function of this optimization is linearly and directly proportional relation of the weight of the structure and the number of layers in each section. More specifically, this function needs to account the areal density of the laminate (*Areal Density*$_{laminate}$), the area of each section (S_{Area}) to be evaluated, and the number of layers (N_{layers}) in each section. The objective function is described in Equation 23.

$$SW = \sum_{k=0}^{n} S_{AreaK} * Areal\ Density_{laminate} * N_{layersK} \quad (23)$$

5.2.3 Design Variables

Design variables in genetic algorithms (GAs) refer to the parameters or characteristics of a design problem that are subject to optimization. In other words, they are the inputs to the GA that determine the quality of the solution.

The developed optimization tool for structural analysis and design involves a finite element model, which is divided into sections selected by the user. The primary objective is to reduce the weight of the structure by minimizing the number of layers in each section. To achieve this objective, the tool employs three variables for each section, one for the number of layers of 0°, another for 90°, and one more for +-45° orientation. Notably, the number of layers in the +-45° orientation is considered equal, resulting in three design variables for each section. These orientations are commonly used in aerostructures and contribute to simplifying the manufacturing process. For this case, the number of layers in each orientation is transmitted to the finite element varying the thickness of each orientation in a symmetric layup. It means that the information transmitted by the GA is translated from number of layers, multiplying this variable for the thickness of each layer. The design variables can be expressed by Figure 69, where s_n is the section number, x_n is the number of layers (design variable) multiplying the thickness of the individual ply-laminate (t).

$0°_{s1}$	$90°_{s1}$	$+-45°_{s1}$	$0°_{sk}$	$90°_{sk}$	$+-45°_{sk}$
X_1*t	X_2*t	X_3*t	$X_{n-2}*t$	$X_{n-1}*t$	X_n*t

Figure 69 - Design Variables

The vector of design variables can be represented by Equation 24. Where the number of variables n can be obtained by the direct relation expressed in Equation 25.

$$X = (x_1, x_2, x_3, \dots, x_n), x_i \in \Omega_i \subseteq \mathbb{R}^n \quad (24)$$

$$n = Number\ of\ Sections * 3 \quad (25)$$

Still, it was chosen to represent the design variables in binary numbers, and this will result in the binary representation (string) in Equation 26.

$$S = b_1 b_2 b_3, \dots, b_n \quad (26)$$

Before proceeding with the binary encoding and decoding, it is necessary to present the Equation 27 that describes the relation of (l_{ci}), the total number of bits for the variable x_i in a binary sequency with (l_i), the total number of solutions that compose the domain of the variable x_i.

$$l_i = 2^{l_{ci}} - 1 \quad (27)$$

Being the xi,bin encoded as a binary substring b_i of length l_i. Then, the decoded subsequence is given by Equation 28.

$$xi, bin = \sum_{k=0}^{li-1} 2^k * b_{i,k} \quad (28)$$

where bi,k represents each component of bi, assuming the values 0 or 1.

The real value of each design variable is obtained by Equation 29.

$$x_i = x_i^{inf} + \frac{x_i^{sup} - x_i^{inf}}{2^{l^i} - 1} * x_{i,bin} \quad (29)$$

Being the upper and lower boundaries x_i^{inf} and x_i^{sup} input values, that can change for each section, it means each three variables (3*i).

The variables of this described process can be represented graphically by Figure 70.

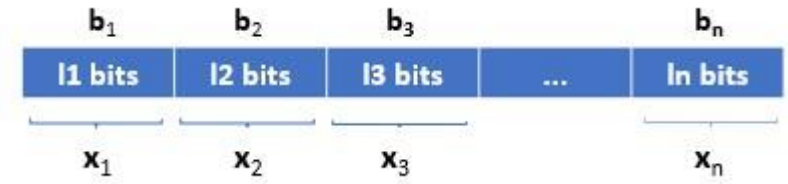

Figure 70 - Binary coding emulating the real representation. [38]

In addition, it should be emphasized that during the analysis, a range of 0 to 15 plies was initially considered. To account for the inclusion of zero-thickness layers in ABAQUS, a value of 0.0001 mm was assumed to represent the null thickness. This approximation was necessary because the finite element software does not accept a null value as input. The extremely small value of 0.0001 mm was chosen to minimize its influence on the overall model, effectively simulating the suppression of the ply.

5.2.4 Fitness Function (Evaluation)

Merit or fitness functions represent the relative value of solutions or individuals in the context of a population and are typically evaluated using a function constructed from the objective function and constraints defined in the mathematical formulation of the optimization problem. From the evolutionary perspective, there are significant distinctions between the objective function and merit/fitness function. The objective function measures the performance of an individual solution with respect to a specific set of gene values, independently of any other chromosome or individual in the population. The objective function is used to evaluate the quality of a solution and guide the search for better solutions.

On the other hand, the merit/fitness function transforms the objective function into an allocation of reproductive opportunities, relative to other members of the population. The fitness function assigns a fitness score to each individual based on its performance in the objective function and other criteria, such as diversity, novelty, or dominance. The fitness scores are used to determine the probability of an individual being selected for reproduction and passing on its genes to the next generation. Therefore, while the objective function guides the search for optimal solutions, the merit/fitness function determines the relative fitness of individuals and their chances of contributing to the next generation. In this way, the fitness function plays a crucial role in the evolutionary process, as it allows the most promising solutions to be selected and propagated, leading to improved performance over time. [38]

For the developed GA, the evaluation process was designed to work following the strategy of having the merit value defined by a normalization process described by Equation 30

$$Mer(x_i) = Fmin + \frac{Fmax - Fmin}{N_{pop} - 1}(Rank(i) - 1) \quad (30)$$

5.2.5 Constraints

The constraint inclusion for this problem consists in the evaluation of composite failure in each individual in the genetic algorithm, representing a specific layup combination. The evaluation is based on the Tsai-Hill failure criteria, which retrieves the failure indexes from a finite element model developed in ABAQUS.

To ensure an effective genetic algorithm, that converges quickly towards the optimal solution, the constraints incorporate a penalization strategy. Individuals that exhibit failure in

any of its plies are penalized with a fixed factor, and in addition to that with the extent of penalization varying depending on the number of failing plies. This second penalization is implemented by adding a penalty term for each ply that presents a failure index greater than 1. Layup combinations where the Tsai-Hill values for all plies falls within the range of 0 to 1 are not penalized as they do not exhibit failure. On the other hand, if the value exceeds 1 for any of its plies, the solution is penalized due to failure. This ranking of solutions with different levels of failure is an important feature, as it allows opportunities for crossover and mutation even for solutions with a small amount of failing plies. It is important to highlight that these extra penalizations are imposed due to the fact that the range of failure index is short, which makes difficult for the algorithm to differentiate them, even if summing their values within a section. Their stablish values for penalizing the solutions were accounted based on the normalized values of $g_4(\boldsymbol{x})$. It is important to mention that because of this penalty approach, it is essential to adjust in an appropriate way the degree of penalization ($\lambda(k)$), applied for all failing solutions in the merit equation. This adjustment ensures that while solutions violating the constraints are ranked, the final solution does not accept those with failure. The topics bellow describes all the constraints and their inclusion to the problem:

- $g_1(x)$: Granting that the solution is below the upper boundary.
- $g_2(x)$: Granting that the solution is above the lower boundary.
- $g_3(x)$: Granting that there is at least one ply in each section.
- $g_4(x)$: Penalizing solutions that present Tsai-Hill ≥ 1, as in Equation 31.

$$g4(x) = g_4(\boldsymbol{x}) + 10 + 1 * Number\ of\ failing\ plies \tag{31}$$

Finally, the inclusion of the penalties is described by Equation 32 and 33. [38]

$$u_j(x) = \max\left[0, g_j(x)\right] \tag{32}$$

$$Aval(x) = f(x) - \lambda(k) \sum_{j=1}^{m} \left[u_j(x)\right] \tag{33}$$

5.2.6 Selection

For this work it was chosen to proceed with proportional selection where the best individuals with better fitness have a greater probability of reproducing or surviving. The process chosen for that was the roulette wheel selection. This process is represented by Figure 71 where it is possible to see a graph of circular sectors in which all chromosomes in the population are placed according to their normalized condition. Then a random number is generated and is used to decide which chromosome to select. It means that chromosomes with higher merit values will be selected more frequently, because they occupy more space on the roulette wheel.

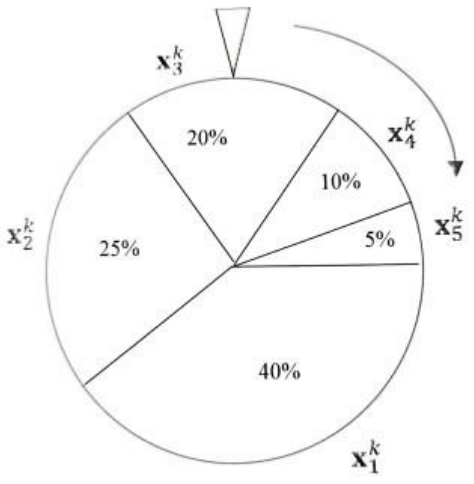

Figure 71 - Example of roulette wheel selection [38]

The probability of selection $P(x^k_j)$ of the individual j of the population with the phenotype x_j, in a generation k, is given by Equation 34.

$$P\left(x_j^k\right) = \frac{f\left(x_j^k\right)}{\sum_{j=1}^{N_{pop}} f\left(x_j^k\right)} \tag{34}$$

where $f(x^k_j)$ is the value of the merit/fitness function and $Npop$ is the population size.[38]

5.2.7 Crossover

Crossover is a genetic operator used in genetic algorithms (GA) to generate new candidate solutions from two or more parent solutions. In crossover, a subset of genes from each parent is combined to form a new candidate solution, which is referred to as an offspring. This process is repeated multiple times to generate a population of diverse candidate solutions. The goal of crossover is to combine the best traits from the parent solutions and create new candidate solutions that are better than their parents. Crossover is a key component of GA and is critical for the algorithm's ability to search for optimal solutions.

From the crossover operators for binary encoding that are emulated as a selection by a mask represented by the vector *Mi*, it was chosen to proceed with the Uniform Crossover (UX) operator that is a variation of the traditional single-point or multiple-point crossover. In traditional crossover methods, the exchange of genetic material is limited to specific positions on the chromosome, known as cut-off points. However, in UX, this concept is generalized in such a way that every position on the chromosome is a potential cut-off point.

During the UX process, a crossover mask is generated which is a random sequence of zeros and ones. This mask has the same number of positions as the chromosomes of the parent and offspring individuals, and the parity of each bit in the mask determines how the gene exchange will be processed. The UX process takes place gene by gene in a sequential manner. For each gene to be created in the offspring chromosome, the operator sorts out from which parent it should be generated. The first offspring, S_1, takes the gene of the first parent, P_1, if the corresponding positional bit of the mask, M_i, is "0". Conversely, S_1 takes the gene of the second parent, P_2, if the positional bit of the mask M_i is "1". The second offspring, S_2, is generated using the complement of the mask M_i, which involves reversing the gene-swapping process used to create offspring S_1. This approach provides a flexible and effective way to introduce diversity into the population of individuals in a genetic algorithm, which can help to prevent premature convergence and improve the search for optimal solutions. The described process can be seen in Figure 72. [38]

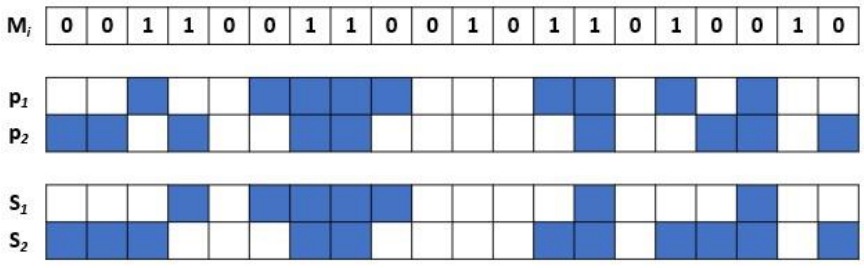

Figure 72 - Uniform Crossover (UX) operator [38]

5.2.8 Mutation

In mutation, a small random change is made to one or more genes in a candidate solution, resulting in a new candidate solution that is slightly different from the original. This process is typically applied with a low probability to maintain the general structure of the

candidate solutions while introducing diversity. The goal of mutation is to prevent the population of candidate solutions from becoming too homogeneous and getting stuck in local optima. Mutation is a complementary operator to crossover in GA and is critical for the algorithm's ability to explore the search space and find global optima.

In this specific case it was chosen to adopt the called gene exchange mutation, or flip-bit, that is the binary representation of the described mechanism. In this case an individual is subjected to random modification – change of binary codes from 1 to 0 and vice versa – with a certain probability P_m to avoid anchoring to a local max/min. The percentage of genes to be mutated is also an input value. A representation of this operator is presented in Figure 73.[38]

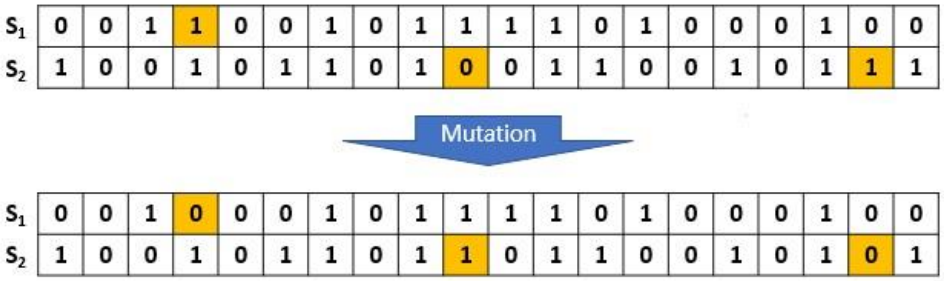

Figure 73 - Flip-bit mutation operator.

5.3 Methods of Applying GA

In the context of optimizing the number of layers in a composite structure, considering the use of genetic algorithm, there are two main approaches that can be used: a pure genetic algorithm and a surrogate model. Since the objective function is simply defined, the main difference between both would be in the evaluate function.

As previously mentioned, the genetic algorithm (GA) is an optimization algorithm that uses a population of candidate solutions to iteratively search for the best solution. Each candidate solution is represented as a string of binary digits or "genes," and these strings are manipulated using genetic operators such as mutation and crossover to generate new candidate solutions. The fitness of each candidate solution is evaluated using an objective function, which is typically a simulation or analysis of the composite structure. In the specific case of this work, the pure GA would be represented by an algorithm that is programed to perform the evaluation of each individual running an ABAQUS simulation for checking the satisfaction of the laminate failure constraints. The idealization of the pure GA can be represented by the flow chart in Figure 68.

A Genetic algorithm with a surrogate model, on the other hand, would keep the same working principles of the pure GA except for the evaluation function, for verifying the failure constraints. In this case the running of the finite element software for each individual would be substitute for the regression data, previously established by the surrogate model. This surrogate model would be based on previously sampling an adequate number of individuals, storing their failure indexes, and performing a regression for interpolating results for any solution. In this way, once the surrogate model is trained, it can be used to predict the failure value for each new candidate solution without requiring a full finite element simulation of the composite structure. This approach is defined by the flow charts in Figure 74.

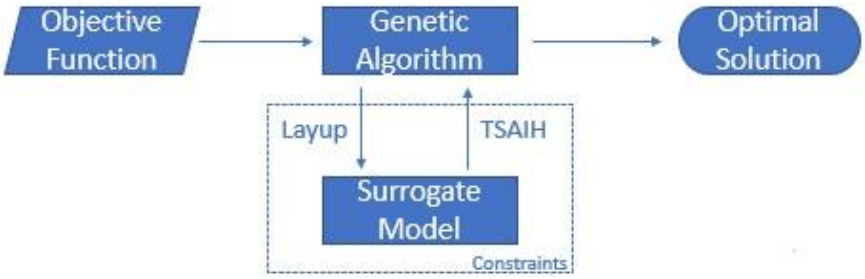

Figure 74 - Computational tool with the surrogate model substituting ang ABAQUS.

When comparing both, it is important to mention some key differences. Starting by the computational time, the Pure GA, into expected to have an extremely large computational time, especially considering large problems, separated in many different sections, and with different layups. This is expected since all the randomly generated population in each iteration would require an ABAQUS simulation for the verification of the failure constraints. For example, a simple simulation with a population of 100, with 500 iterations would require 50000 simulations in ABAQUS, and having into account an estimated time of 5 minutes for completing each analysis, in a traditional laptop, this approach would take around 24 weeks to be completed. It is worth noting that these values are simple suppositions since these parameters and time estimation are very sensitive to the size of the problem and its complexity, as the computer that is simulating. Still, it is possible to reduce the computational time of this approach by using a data base and avoiding the use of the finite element model for evaluating an individual that has been previously evaluated in the previous population. In any case, the tunning of the parameters for this optimization is an important step that require iterations, in this approach the high computational time spend to iterate these parameters also needs to be considered.

In the other hand, the surrogate model, with a data regression needs a smaller number of well-defined samples, that are simulated and stored in a database. These samples are needed for establishing a regression that will be capable of defining all the evaluated points. This approach, in addition to allowing a faster iteration of initial parameters for the GA, also has the potential of reducing the computational cost from several weeks to a few days. Still, needs to be considered the time spend in performing a sensitivity analysis for the regression, but once defined the surrogate model, it is possible to run the genetic algorithm in a few minutes. However, the surrogate model is expected to be less accurate since it performs approximations for the constraints, while the pure GA extracts these values directly from ABAQUS. Another important note is that with the use of a regression model, it is possible to maximize the use of the CPUs available, segregating the total samples to be tested and running them in parallel, this approach has the potential of reducing the computational time.

In conclusion, both pure genetic algorithms and surrogate models can be effective approaches for optimizing the number of layers in a composite structure. The choice of approach depends on the specific problem, the computational resources available, and the level of accuracy and robustness required. A pure GA is more accurate but computationally expensive, while a surrogate model is computationally efficient but may introduce inaccuracies. Still, the surrogate model will create a possibility of iterating the algorithm and model parameters, which for this work, is expected to conduct to better results. Moreover, after simulating a small model for a specific load case with a pure genetic algorithm, it was concluded that the expected time to be spent could not be afforded for this project since the development of the complete tool needs to count with errors and corrections.

Surrogate model

5.4.1 Structure

Figure 75 is a schematic representation of the obtention of the surrogate model to substitute the direct use of ABAQUS in the computational tool.

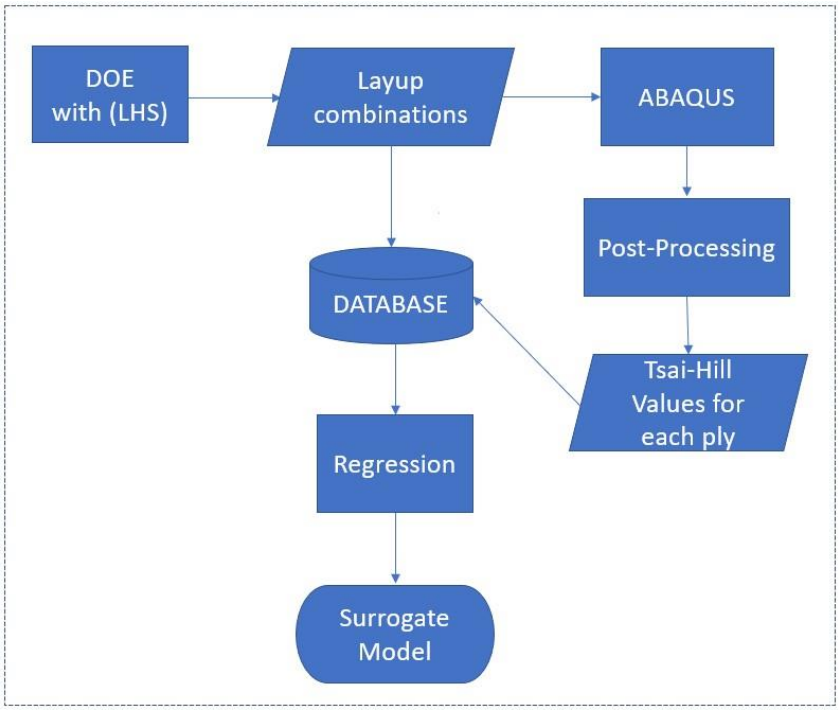

Figure 75 - Surrogate Model flow chart

5.4.2 Samples - DOE: Latin Hypercube

For the sampling with the layup combinations to be used in the surrogate model, a Python code integrating ABAQUS was developed. This code uses the DOEPY Python library to generate a design of experiments (DOE) using Latin Hypercube Sampling (LHS) to optimize the sampling to be analyzed in ABAQUS for generating the database for later doing the regression of the stablished constraints for the GA.[63]

In the specific code it is possible to set upper and lower bounds for the independent variables, which represent the maximum and minimum values that the variables can take on. Next, using the *build_space_filling_lhs* function, it generates the design experiments having into account the number of sections in input, which for this specific case is three independent variables per section. This function uses LHS to generate a representative set of samples from a multi-dimensional space, ensuring that the chosen number of samples are evenly distributed across the input space.

In this matter, it is important to mention that choosing an adequate number of samples for Latin Hypercube Sampling (LHS) depends on several factors, including the number of variables being studied, the complexity of the relationship between the variables and the response, and the desired level of precision or accuracy. Nevertheless, knowing that the relationship between the variables and the response is complex or nonlinear, it is expected to need a great number of samples to fully capture the behavior of the system. Also, to obtain a higher level of precision, more are required, since, in general, the more samples used, the more precise the results will be.

Finally, it is necessary to evaluate through the regression results if the chosen number of samples is adequate to the problem, as per example the use of metrics like R-squared or mean error through cross-checking results and performing a sensitivity analysis. The said analysis involves varying the number of samples and observing the impact on the results. If the results are stable across a range of sample sizes, then the current sample size may be adequate.

5.4.3 Finite Element Analysis and DATABASE

An important part of the computational tool is the definition of the ABAQUS finite element model that will be the basis of the results to be retrieved. At this point a Python script that contains the model object of analysis and optimization was created. This script is capable of generating the model one time and iterate the design variables, in this case the thickness of the 0, 90 and +-45-degree plies, according to the previously defined design of experiments (DOE) and submitting each" job" for analysis. Still, in between each analysis, a data post processing is performed, where the program identifies the element where the greater failure index (Tsai-Hill) is present for each ply orientation and retrieves this information. Considering that there are three different possible variables, for each section, the post processing will retrieve three different maximum Tsai-Hill values.

Since the described process is time consuming, it was clear the necessity of implementing the use of a database capable of storing the results from each iteration. Thus, being able to continue the analysis from where it started in case of necessity of stopping the process for any problem. For that it was used the python module "sqlite3" [64] that provides a straightforward way to interact with SQLite databases. This module allows the creation of the database. In addition to save the layup combination and its maximum Tsai-Hill values, the developed computational program verifies if the layup combination is already in the database, in positive case it skips the iteration. This described process is detailed in Figure 76.

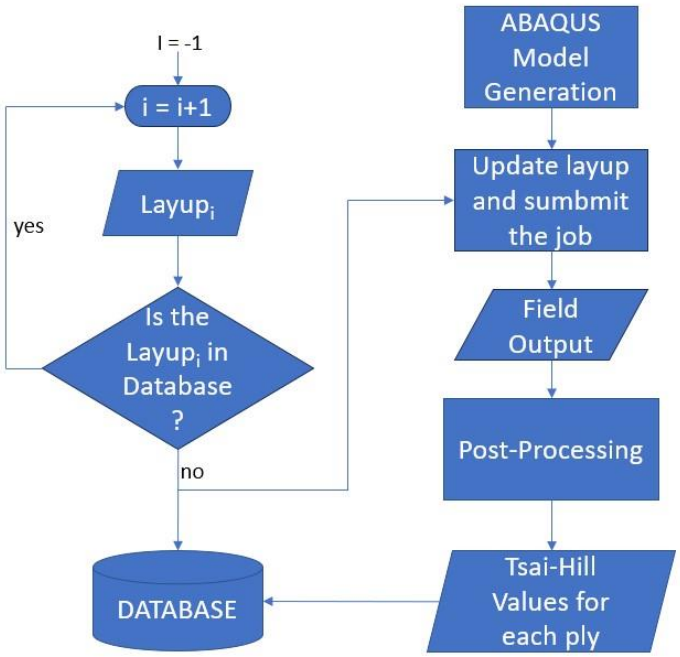

Figure 76 - Flow Chart, Finite Element Analysis and Database.

5.4.4 Load Cases for Comparison

After defining the methodology for generating the layup combinations to be tested, and extracting the results from ABAQUS to the database, it is possible to perform the regression of the stored data generating one equation for each layer in each section.

For this, it was considered six methods of regression to be compared with a testing set retrieved from ABAQUS results, and thus choosing the most adequate one for proceeding the work. The regression methods to be tested are the Linear, Polynomial, Lasso, Ridge, Elastic Net and Gaussian Process regressions. Moreover, for performing this comparison, four known load cases were taken as basis to verify the obtained results. The four chosen load cases were the Tensile Plate, Four Point Bending Plate, Pure Shear Plate and Open Cylinder with internal pressure. These models were evaluated using metrics such as the R-squared (R2) value, which measures the proportion of variation in the dependent variable that is explained by the independent variables. Which means that a value of 0 does not explain any variance in the target variable, and it is essentially equivalent to randomly guessing the target values, and a value of 1 indicates that the regression model perfectly predicts the target variable, capturing all of the variance in the data. Other parameters to perform this evaluation are the Mean Squared Error (MSE) and Mean Absolute Error (MAE), both metrics quantify the average discrepancy between the predicted values and the actual values of the target variable, being the first the average square difference and the second the average absolute difference.

As mentioned before, four known load cases of one section (three variables) were created to compare the performance of the regression methods and to evaluate correct functioning of the developed Genetic Algorithm. These four load cases are following described:

- Tensile Plate:

  This load case is represented by an ABAQUS model for a plate subjected to pure tension. The following model has a symmetric layup of $[45/-45/90/0]_s$ and has equally distributed load in one of its edges, while in the other edge has one fully constrained (Encastre) point in its middle and displacement restrictions U2 = U3 = 0. It is worth mentioning that this model was thought to have an expected answer of 7 layers of 0-degrees carbon fiber (aligned to the load). The model's representation is followed represented by Figure 77.

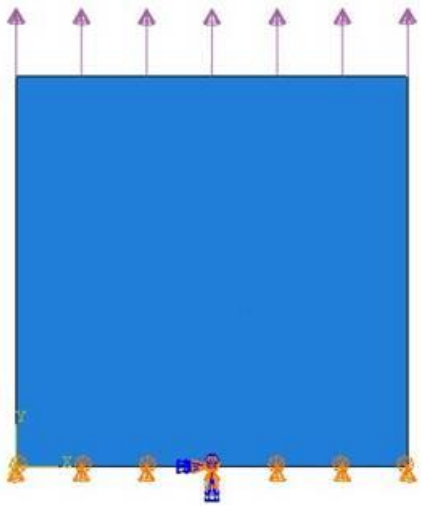

Figure 77 - Tensile Plate ABAQUS model

- Pure Shear:

The Pure Shear load case was designed in ABAQUS (Figure 78) to represent a pure shear test plate where the layup order would be $[45/-45/90/0]_s$ and has loads applied in the positive direction as Edge Forces in the upper and right edges. The left edge has a displacement restriction U2 = U3 = 0 and the bottom edge U1 = U3 = 0. Also, the sheared point of these edges has a displacement constraint U1 = U2 = U3 = 0 (pinned). The load applied was thought to be in a way to expect the result of 7 layers of carbon fiber aligned to 45-degrees and another 7 in -45-degrees.

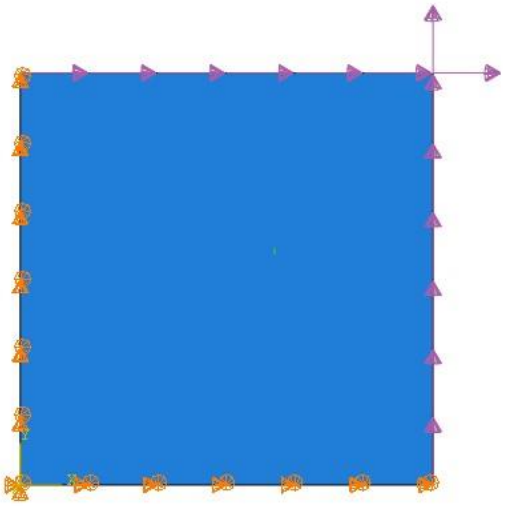

Figure 78 - Pure Shear Plate ABAQUS model

- Four Point Bending:

This load case was developed to simulate a four-point bending test in a carbon fiber plate, for that it was developed the followed represented in Figure 79 finite element model. The model was created having two edges close to each end of the plate with a displacement constraint of U3 = 0 and one point with the restriction U2 = U3 = 0. Also, it was applied a concentrated load in a reference point that has structural linear coupling constraints to both central plate edges. For this specific case the carbon fiber layup is $[0/90/45/-45]_s$ since it is expected to have better results for having 0-degree external layers in bending case. As in all the load cases, the applied load was thought for obtaining a result of 7 layers of carbon fiber, in this case expected to be aligned in 0-degrees.

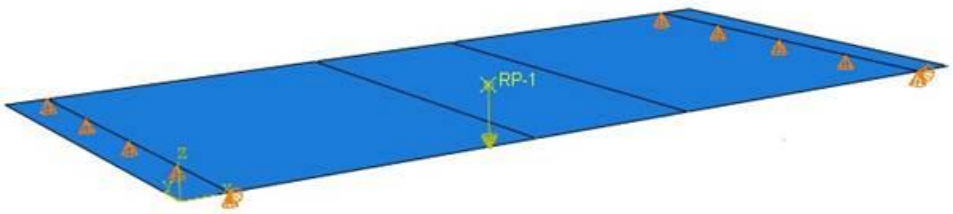

Figure 79 - Four-point bending Plate ABAQUS model.

- Cylinder with Internal Pressure:

The open cylinder with internal pressure finite element model was developed to simulate a case where it is more advantageous to obtain results where the carbon fiber layers are aligned to 90-degrees, it means the circumferential aligned layers. For this

model the boundary conditions were applied in the form of two points in the center of the cylinder as U2 = 0 and other two as U1 = 0. The loads were applied in the internal surface as pressure, and they were thought to obtain 7 layers of 90-degrees as result. The chosen layup for this case was $[45/-45/90/0]_s$. The ABAQUS model is represented in Figure 80.

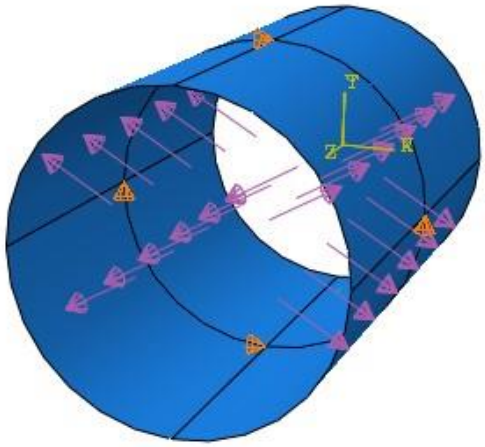

Figure 80 - Open-cylinder with internal pressure ABAQUS model

5.4.4 Regression Models Comparison

In this subsection, the results from the studied regression methods will be presented and compared, also having as reference base the points extracted from ABAQUS simulations. It is important to highlight that for all the cases a data base of 200 points, and 300 points for the four-point bending were extracted, where 80% of them were used as training data and the other 20% for testing and to obtain values such as the mean absolute error (MAE) and R-square (R2) that helped to adjust the parameters of its regression, being able to obtain results close to its best performance.

Being each load case a problem with three equations and three variables each, the difficult to represent them graphically is obvious. Nevertheless, it is possible to make some assumptions to extract information graphically. The first is a 3d plot where the number of layers from 0 to 15 in each orientation is represented in each axis and the color of the point represents the laminate failure, being red the ones that fail in at least one of the layers, and blue the ones that do not present ay failure. This previously mentioned plot together with the three plots with the variation of number of layers by the Tsai-hill value it is possible to understand the more influential layer of each load case and verify the validation models. Still, to compare the performance of the regression methods, for each load case, based on their trained model, it was chosen to fix the two less influential layers and vary the other remaining. In this case, the performance was measured comparing the obtained predictions from all the different regression methods to the results extracted directly from ABAQUS.

- Tensile Plate:

For this present load case, as expected, and from Figure 81 to Figure 84 it was possible to conclude that the zero-degree ply is the more influential one, where increasing the number of layers in this direction is directly related to reducing the laminate failure.

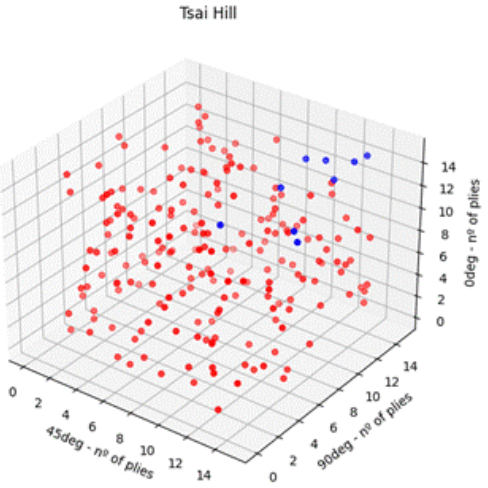

Figure 81 - Tensile Plate, failure related to the three possible orientations.

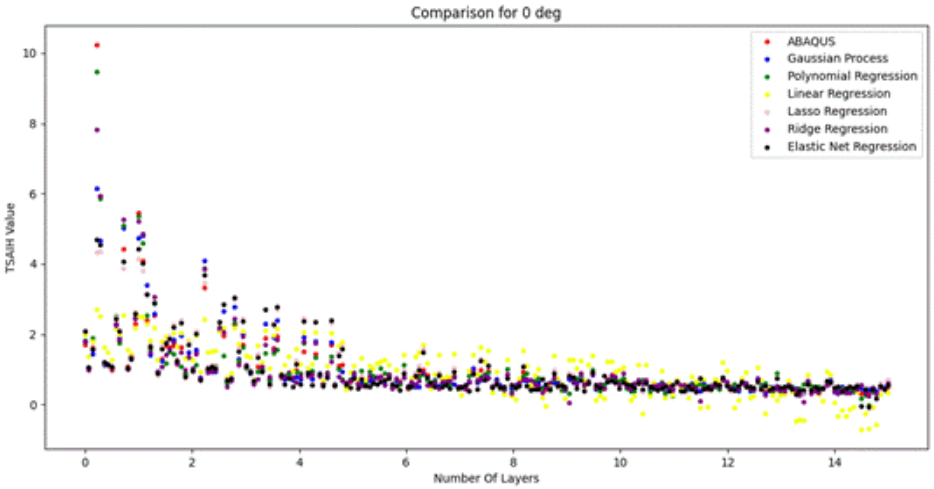

Figure 82 - Tsai-Hill vs number of layers in 0-degrees.

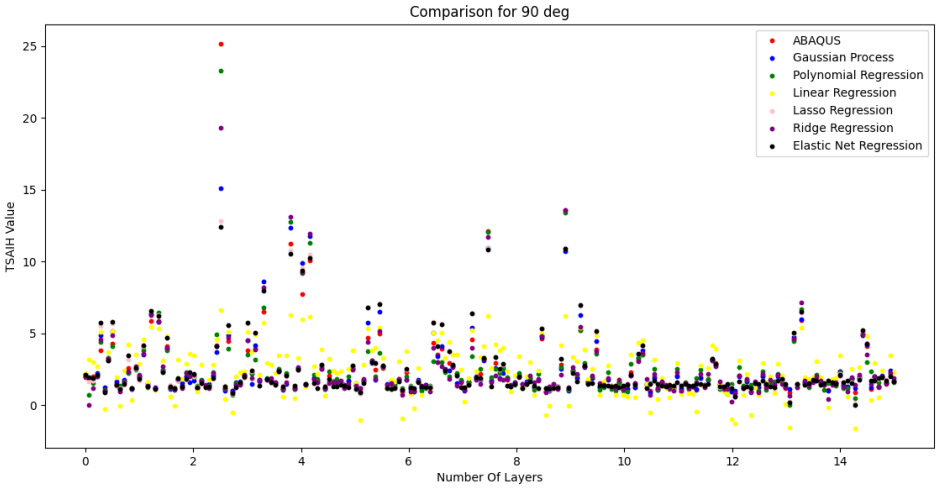

Figure 83 - Tsai-Hill vs number of layers in 90-degrees

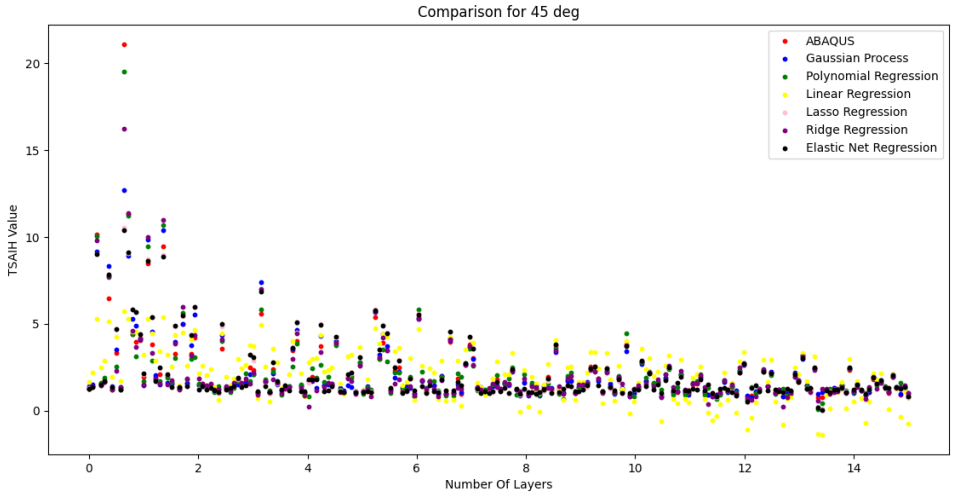

Figure 84 - Tsai-Hill vs Number of layers +-45-degrees.

After that, for comparing the performance of the regression methods, it is possible to present the graph of varying the most influential ply, in this case 0-degrees, from 0 to 15 layers, fixing the other orientations in zero layers and verify the comparison with the base reference of values extracted from ABAQUS (Figure 85).

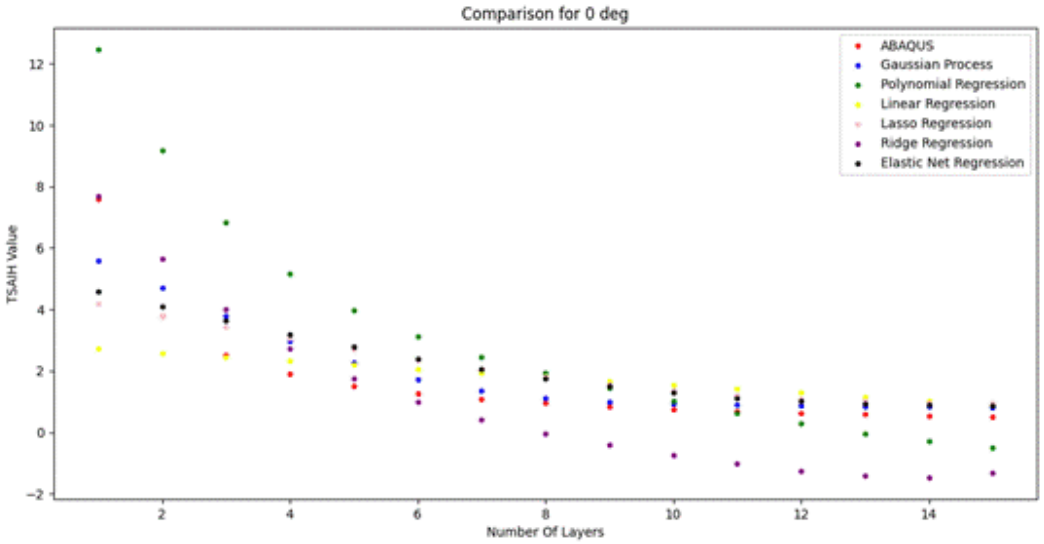

Figure 85 - Tensile plate, regressions comparison for the most influential ply.

It is worth mentioning that for the regression methods is important to understand that the boundary values may present numerical errors, because the values of excessive failure coming from ABAQUS represents noise values for the regression. For that, this comparison mainly focused on the central interval for the number of layers. Taking it into account, it was possible to verify that for the most relevant layer for this problem, the Gaussian method was the one that performed better predictions.

- Pure Shear:

For this present load case, as expected, and from analyzing the Figure 86 to Figure 89 it was possible to conclude that the +-45-degrees layers are the more influential ones, where increasing the number of layers in this direction is directly related to reducing the laminate failure.

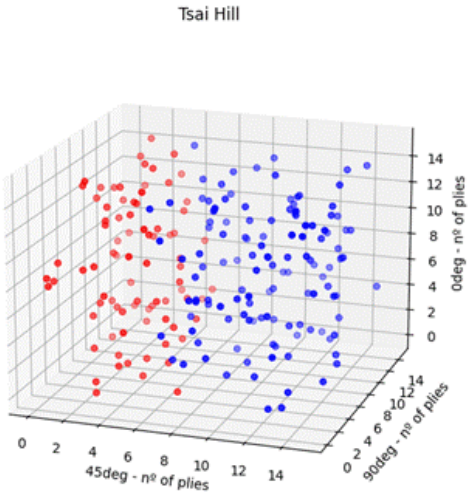

Figure 86 - Pure Shear, failure related to the three possible orientations.

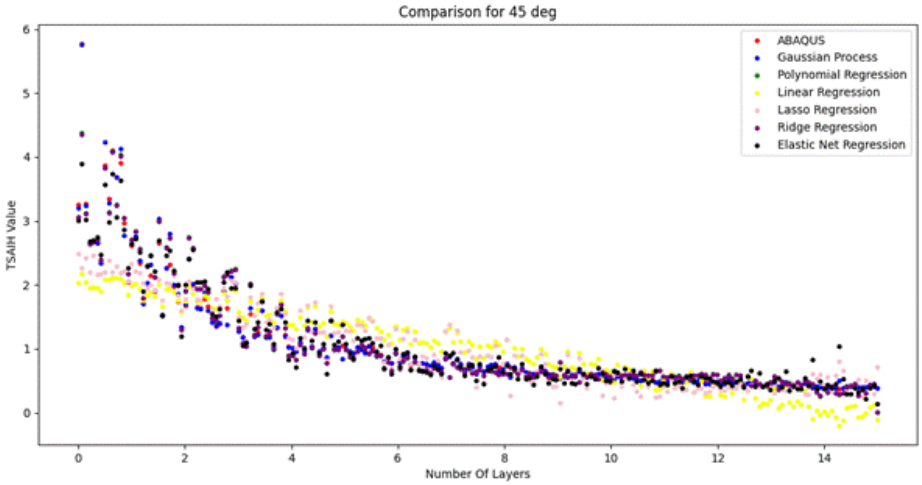

Figure 87 - Tsai-Hill vs number of layers in +-45-degrees.

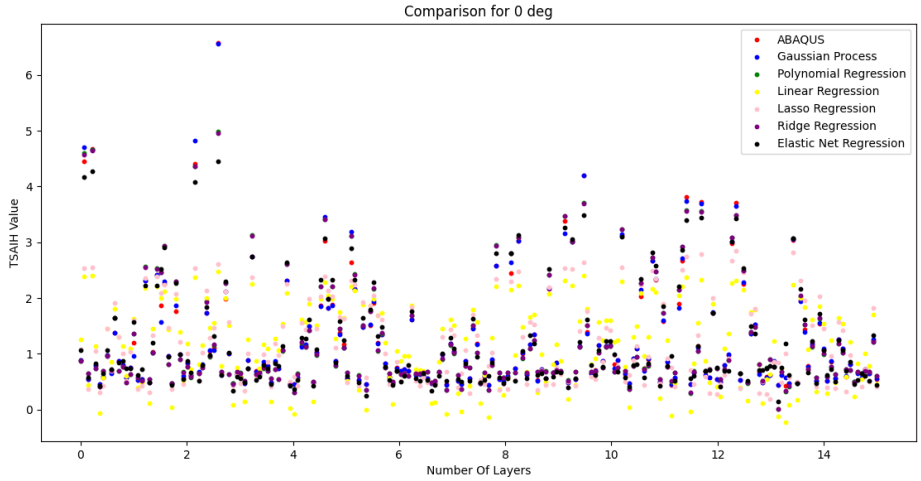

Figure 88 - Tsai-Hill vs number of layers in 0-degrees.

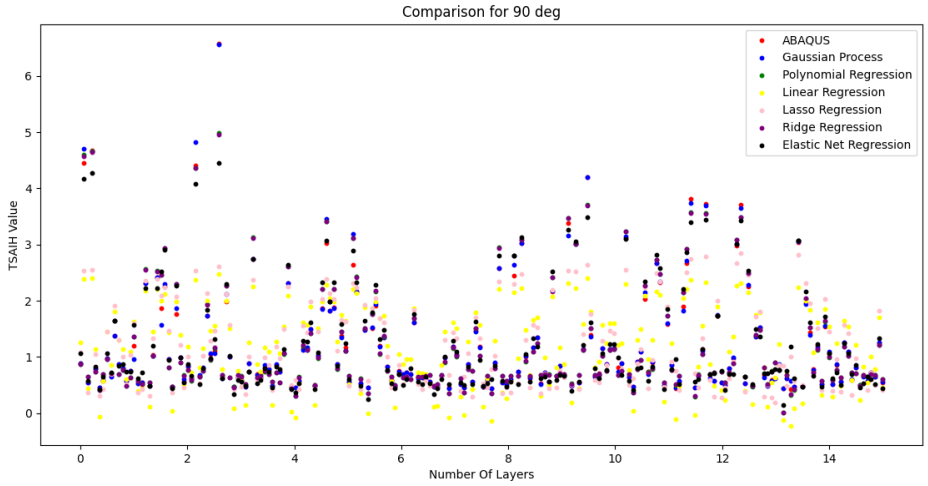

Figure 89 - Tsai-Hill vs number of layers in 90-degrees.

After that, for comparing the performance of the regression methods, it is possible to present the graph of varying the most influential ply, in this case +-45-degrees, from 0 to 15 layers, fixing the other orientations in zero layers and verify the comparison with the base reference of values extracted from ABAQUS (Figure 90).

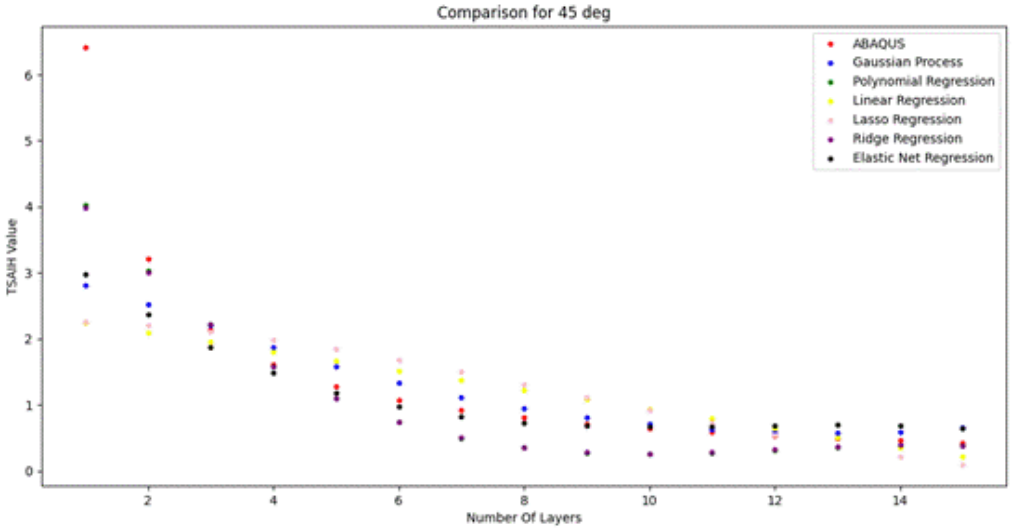

Figure 90 - Pure Shear Plate, regressions comparison for the most influential ply.

As in the previous case, it is important to focus on the center of the interval to do the comparison. Taking it into account, it was possible to verify that for the most relevant layer orientation for this problem, the elastic net and the polynomial were the ones that performed better. Still, the gaussian appeared to respect the real shape of the curve better.

- Four Point Bending:

For this present load case, as expected, and from Figure 91 to Figure 94 it is possible to conclude that the 0-degrees ply orientation is the most influential orientation, where increasing the number of layers in this direction is directly related to reducing the laminate failure.

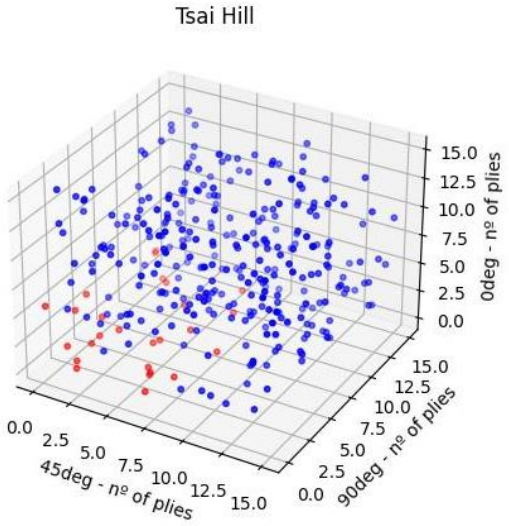

Figure 91 – Four-point bending, failure related to the three possible orientations.

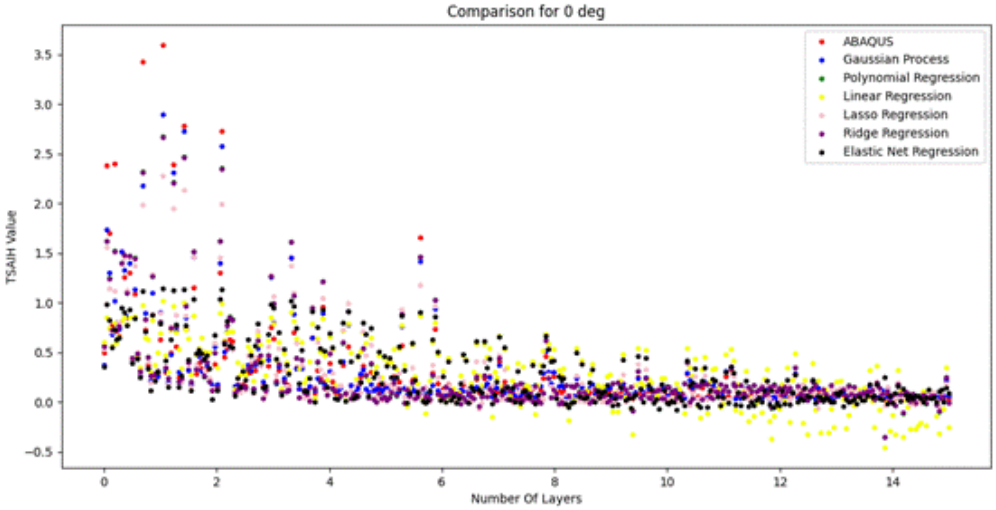

Figure 92 - Tsai-Hill vs number of layers in 0-degrees.

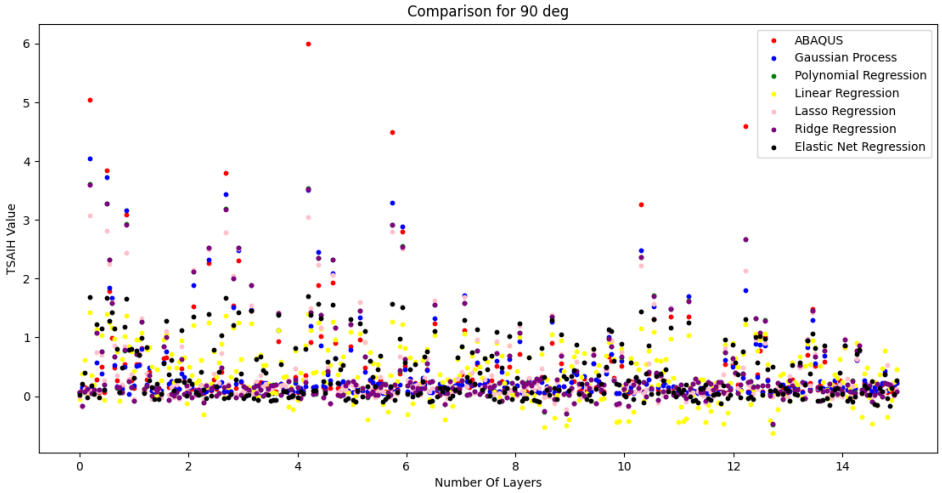

Figure 93 - Tsai-Hill vs number of layers in 90-degrees.

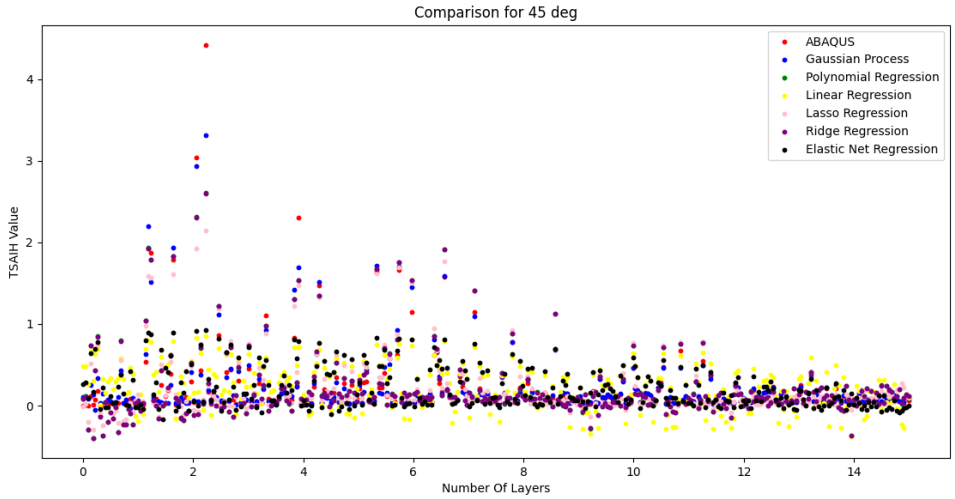

Figure 94-Tsai-Hill vs number of layers in +-45-degrees.

After that, for comparing the performance of the regression methods, it is possible to present the graph of varying the most influential ply, in this case 0-degrees, from 0 to 15 layers, fixing the other orientations in zero layers and verify the comparison with the base reference of values extracted from ABAQUS (Figure 95).

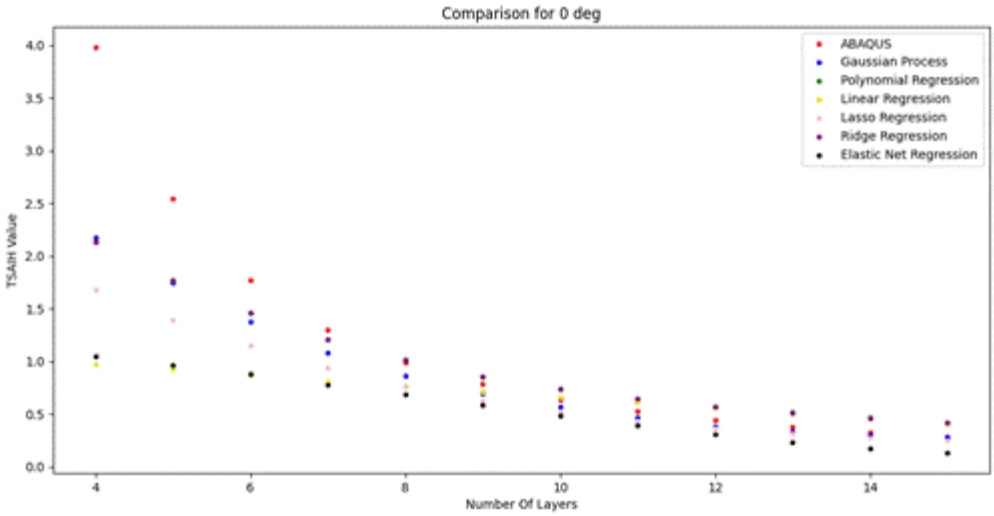

Figure 95 – Four-point bending plate, regressions comparison for the most influential ply.

As in the previous case, it is important to focus on the center of the interval to do the comparison. Taking it into account, it was possible to verify that for the most relevant layer orientation for this problem, the gaussian and ridge regressions were the ones that performed better.

- Open Cylinder with internal pressure:

For this present load case, as expected, and from Figure 96 to Figure 99 it is possible to conclude that the 90-degrees ply orientation is the most influential orientation, where increasing the number of layers in this direction is directly related to reducing the laminate failure.

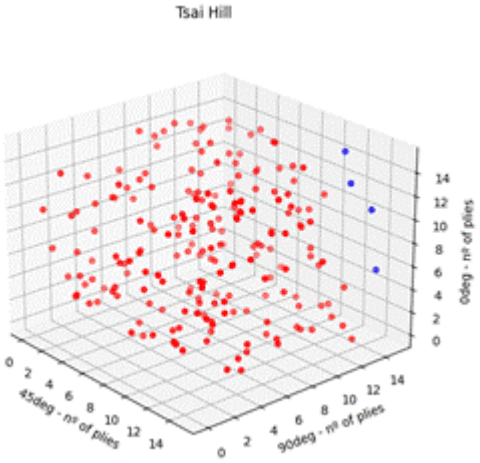

Figure 96 – Open Cylinder with internal pressure, failure related to the three possible orientations.

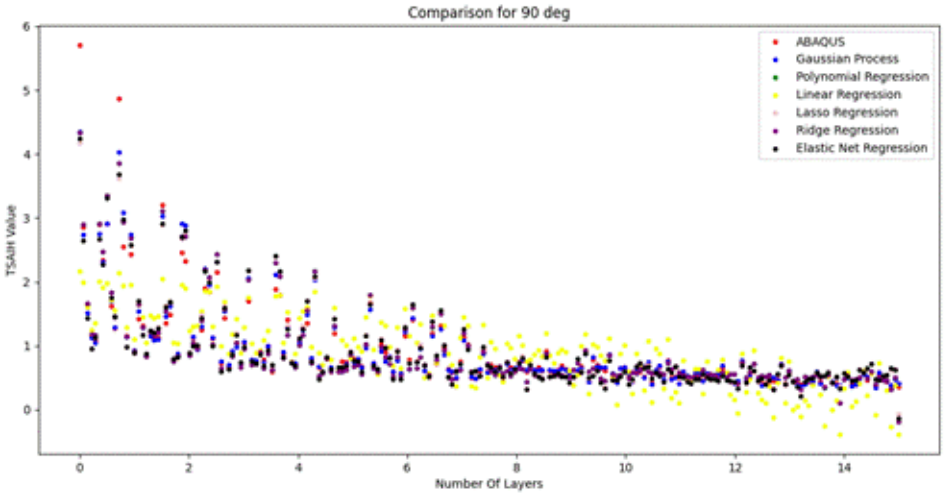

Figure 97 - Tsai-Hill vs number of layers in 90-degrees.

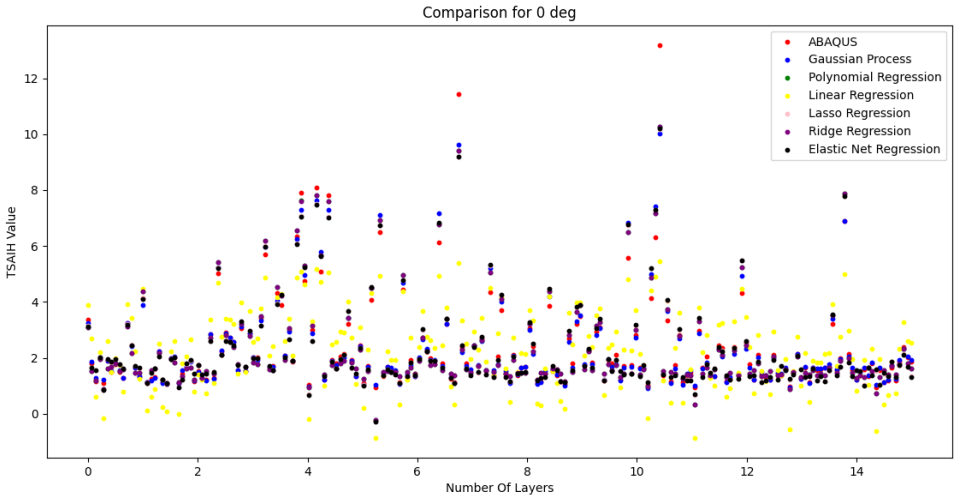

Figure 98 - Tsai-Hill vs number of layers in 0-degrees.

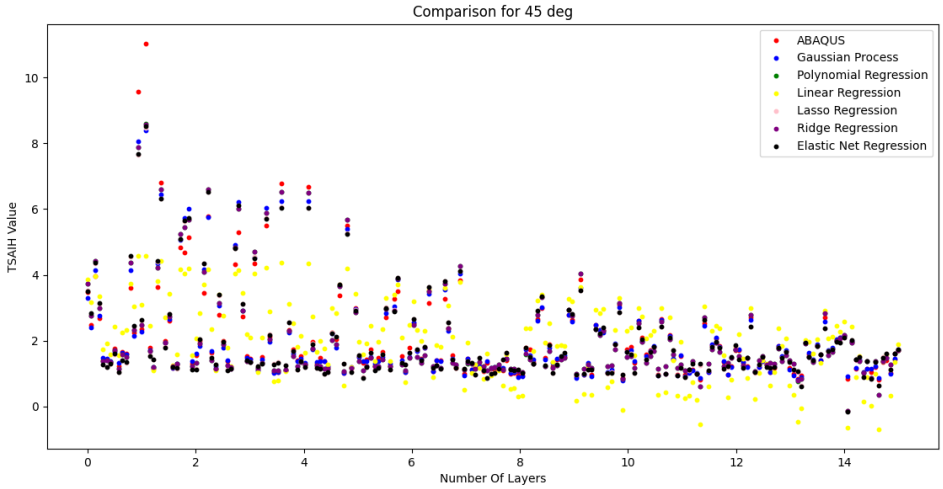

Figure 99 - Tsai-Hill vs number of layers in +-45-degrees.

After that, for comparing the performance of the regression methods, it is possible to present the graph of varying the most influential ply, in this case 90-degrees, from 0 to 15 layers, fixing the other orientations in zero layers and verify the comparison with the base reference of values extracted from ABAQUS (Figure 100).

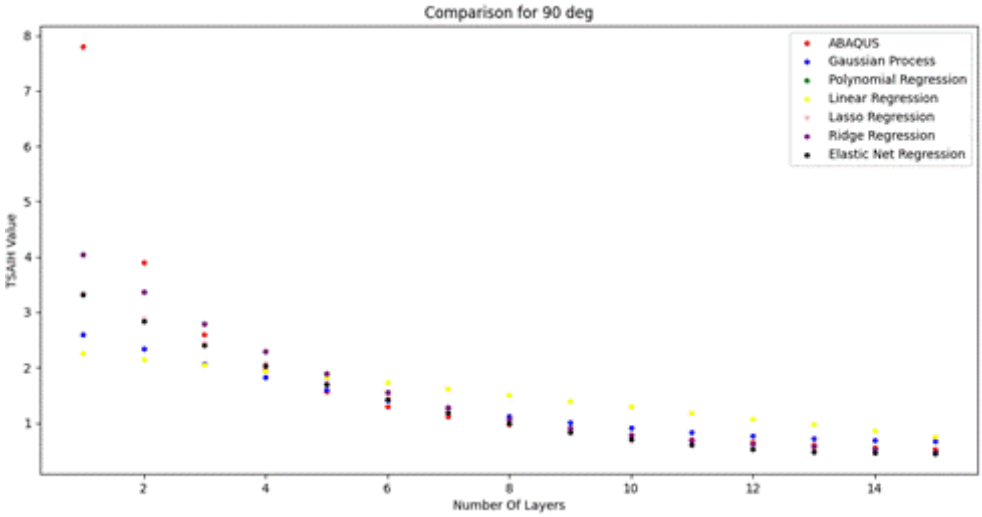

Figure 100 – Open Cylinder with internal pressure, regressions comparison for the most influential ply.

Focusing on the middle of the interval, as the other cases, to do the comparison. Taking it into account, it was possible to verify that for the most relevant layer orientation for this problem, the elastic net and the polynomial were the ones that performed better. Still, the gaussian appeared to respect the real shape of the curve better.

After conducting a graphical comparison of the regression models using different load cases, it is possible to conclude that the Gaussian process regression, although more computationally intensive, provided a superior fit for this problem in terms of overall performance. This outcome aligns with the initial expectations, since the gaussian process is the most flexible regression method. This characteristic is also valuable for the final problem that requires more flexibility, taking into account the different sections and the multiple combined load cases. Notably, this experiment showcased the effectiveness of Gaussian process regression in accurately predicting unseen values from ABAQUS. However, it is essential to emphasize that the final choice of regression method for the continuation of this work will be made after thorough evaluation of their performance in conjunction with the Genetic Algorithm.

By considering their combined performance and suitability for the specific objectives of the study, the most appropriate regression method will be determined for further investigations.

5.5 Validation of the computational tool

Finally, it is viable to conduct a validation test for the computational tool that has been developed by performing the optimization of the known load cases. Through analyzing the outcomes of the previously conducted influential ply tests and loading-controlled cases, it is determined that the optimal layup configuration will consist of seven layers in the most influential ply, while the remaining plies will have zero layers. Table 6 presents the reference optimal value from ABAQUS compared to the results of each regression model.

Table 6 - Validation of GA and comparison for different regression methods

#	Tensile Plate	Pure Shear	Four-point Bending	Open-cylinder (internal press.)
Method	$[+-45/90/0]_s$ Number of Layers	$[+-45/90/0]_s$ Number of Layers	$[0/90/+-45]_s$ Number of Layers	$[+-45/90/0]_s$ Number of Layers
ABAQUS	[0;0;7]	[7;0;0]	[7;0;0]	[0;7;0]
GA-Linear	[0;0;13]	[9;0;0]	[4;0;0]	[0;12;0]
GA-Polynomial	[0;0;10]	[6;0;0]	[8;0;0]	[0;8;0]
GA-Lasso	[0;0;11]	[9;0;0]	[7;0;0]	[0;8;0]
GA-Ridge	[0;0;7]	[6;0;0]	[9;0;0]	[0;8;0]
GA-Elastic Net	[0;0;11]	[6;0;0]	[5;0;0]	[0;8;0]
GA-Gaussian	[0;0;9]	[7;0;0]	[7;0;0]	[0;9;0]

Based on the results, it can be concluded that the ridge method outperformed the Gaussian method for the tensile plate and open cylinder with internal pressure cases. However, in the Pure shear and Four-point bending cases, the optimization tool with Gaussian process regression achieved the exact optimal solution, while the other two cases yielded results that were not optimal but very close and still valid. Consequently, it can be inferred that the Gaussian method, being a more flexible approach, exhibited superior overall performance as anticipated. Therefore, the Gaussian method was selected as the definitive regression approach for the developed computational tool. Furthermore, it was possible to confirm the well-functioning of the Genetic algorithm that directed to the most optimal solution region as well as confirming the validity of the hypothesis and assumptions taken during the development of the computational tool for this work.

5.6 Applying the computational tool to a simplified wingbox.

5.6.1 Introduction

After successfully validating the computational tool's capability to find the minimum weight layup while avoiding laminate failure, it is important to test the tool in a multi-section model. This test aims to identify the actual challenges posed by the algorithm, particularly in relation to the regression model. Given that each section represents an increment of three variables, it is anticipated that difficulties may arise in accurately predicting failure for all possible combinations. It is expected that a larger number of samples will be required for many sections, which may potentially impact the computational cost of the simulation or the quality

of the optimization. In this sense, a pseudo-wingbox configuration was developed, consisting of two spars, two ribs, and two skin panels (upper and lower skin). This model serves as a test for a problem involving six sections, representing a total of 18 variables. Furthermore, as the sections experience distinct loading conditions due to their diverse structural roles, it offers an opportunity to assess the regression model's performance under conditions of high nonlinearity.

5.6.2 Model and assumptions

The testing model being referred to represents a single wing bay located between ribs in a wingbox. This model is illustrated by Figure 101, where the rectangular sections correspond to the ribs and the trapezoidal sections represent the spars. [32], [65].

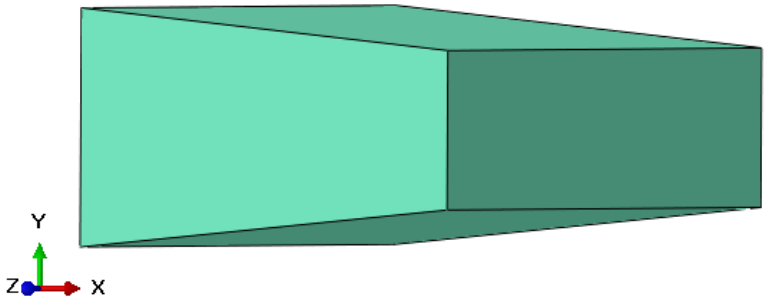

Figure 101 – Simplified wingbox ABAQUS model.

Once the part is created, the next step involves defining the composite layups for different sections, which are also subjected to optimization. At this stage, it is crucial to establish the reference orientation for 0 degrees. While these sections may vary, those belonging to the same structural group can have their orientations represented in a single image. Specifically, the orientations for the upper and lower skins (Sections 1 and 2, respectively) are depicted in Figure 102, while Figure 103 illustrates the orientations for the main spar (Section 3) and secondary spar (Section 4). On the other hand, Figure 104 shows cases of orientations for the Ribs (Section 5 for the right, loads side and Section 6 for the left, fixed side). These visual representations aid in defining the appropriate orientations for each section of the composite layups. It is worth mentioning that the layup was fixed in $[+-45/90/0]_s$.

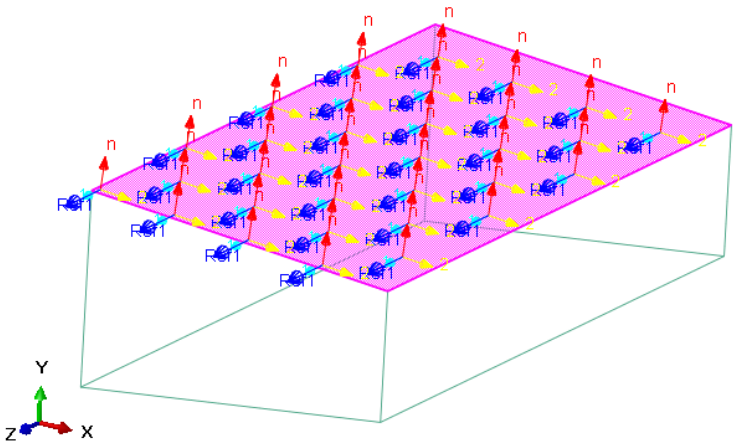

Figure 102 - Optimization Section 1 and 2 (Skins), reference orientation.

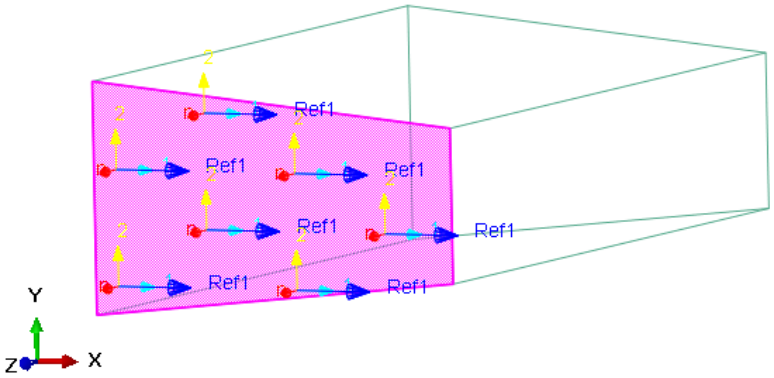

Figure 103 - Optimization Section 3 and 4 (Spars), reference orientation.

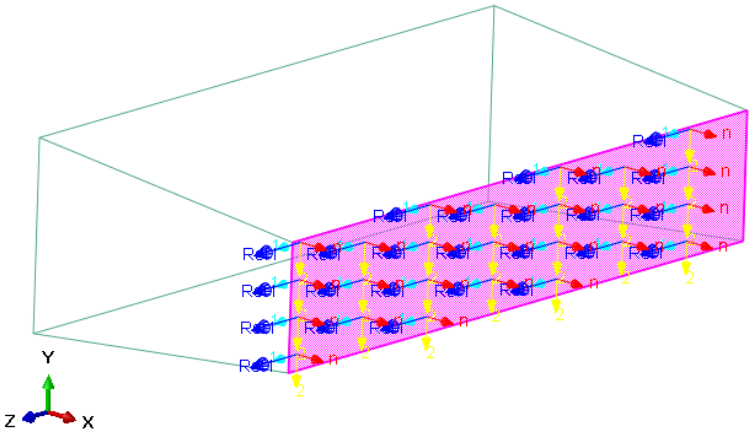

Figure 104 - Optimization section 5 and 6 (Ribs), reference orientation.

After establishing the different sections for optimization, it is essential to define the boundary conditions and apply the loads to the structure (Figure 105). Notably, one of the ribs is fully constrained (Encastre) at both vertical edges, ensuring it remains fixed. Conversely, the other rib receives punctual loads at its two upper vertices. It is important to note that the magnitudes of these loads have been arbitrarily chosen. Specifically, the load on the main spar is set at 75% of the total load, while the load on the secondary spar is set at 25% of the total load. This distribution is selected to increase the complexity of the problem and provide an approximation to the expected load distribution in the final wing structure. Also, when talking about the arbitrary magnitude of these loads, it aims to simulate a scenario where failure occurs around the middle of the range of the number of plies, contributing to the assessment of the optimization tool performance.

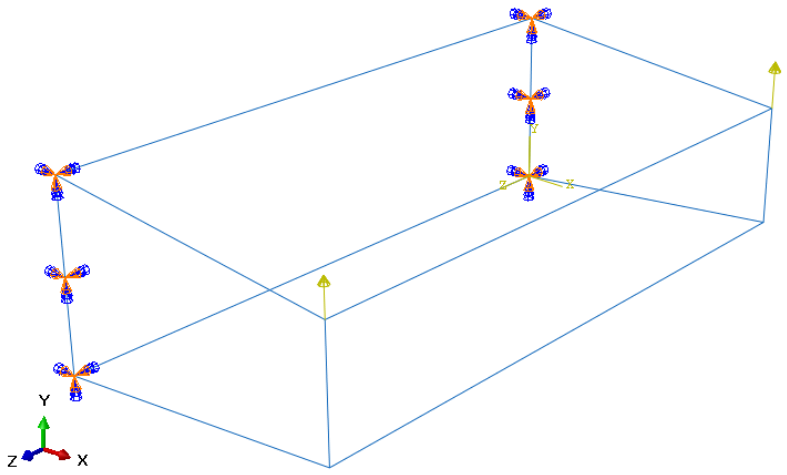

Figure 105 – Simplified wingbox, Boundary Conditions.

After defining the boundary conditions and load application, the next step is to determine the mesh for the structure. In this case, a QUAD-structured (S4R) mesh with 12814 elements was employed. Additionally, it is crucial to highlight that a mesh convergence analysis was conducted to determine the minimum number of elements required. This analysis ensures that the mesh is refined enough to capture the critical details and accurately represent the behavior of the structure. By iteratively refining the mesh and evaluating the convergence of the results, an optimal mesh resolution was determined to strike a balance between computational efficiency and accuracy in the analysis.

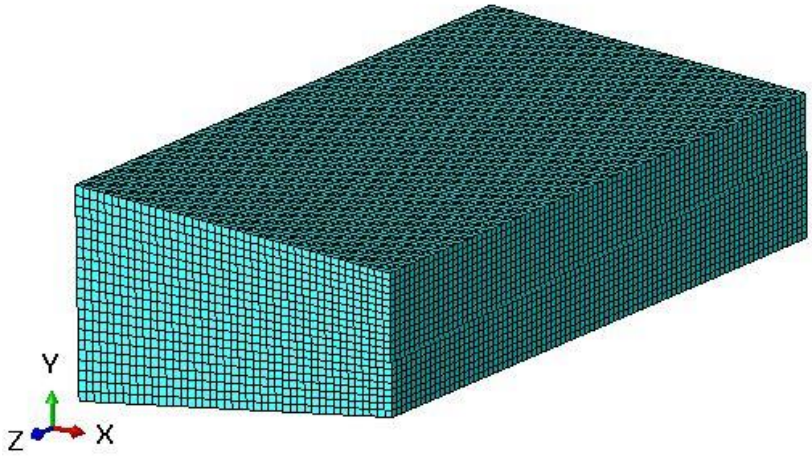

Figure 106 – Simplified wingbox, 12814 elements mesh.

After defining the mesh, it is possible to define elements sets in each section, for the post processing. This allows to cut out the boundary conditions from the analysis, avoiding the artificial concentrations of loads. At this case, it is possible to verify in Figure 107 that the eight corners of the pseudo-wingbox were cut out.

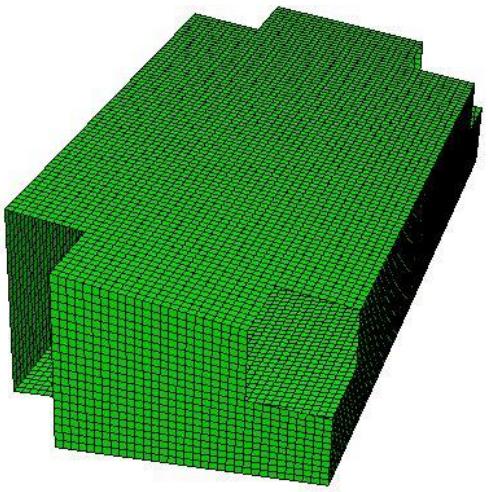

Figure 107 - Boundary conditions eliminated for analysis, view 1.

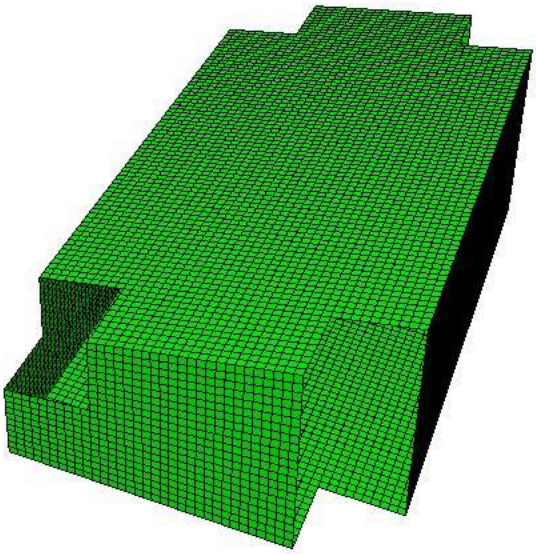

Figure 108 - Boundary conditions eliminated for analysis, view 2.

Finally, it is possible to present the deformed shape of the model to prove the well-functioning, not being visible any disconnections or anormal behavior.

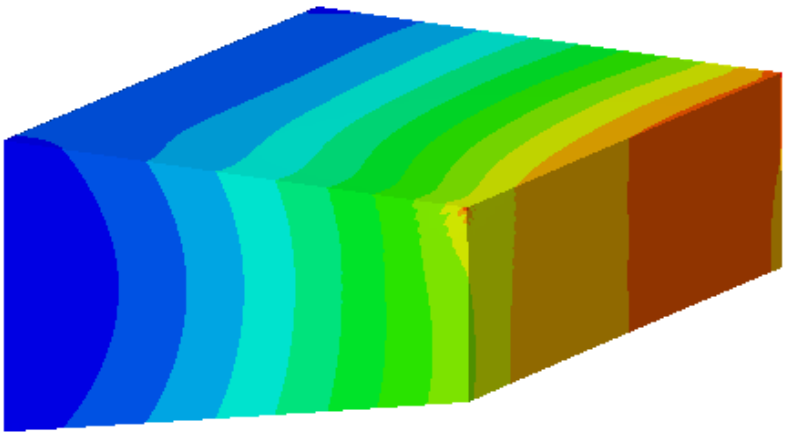

Figure 109 – Simplified wingbox deformed shapes.

5.6.3 Optimization tool parameters

As mentioned earlier, the optimization problem at hand involves six distinct sections, resulting in 18 independent variables. These sections represent different structural elements that are subjected to varying load conditions. To address this problem, a total of 16 levels were established for each independent variable, with values ranging from 0 to 15. In order to generate a training set, 1400 samples were chosen using Latin hypercube (LHS) sampling technique. The selection of the number of samples was based on a cross-validation process, considering the evaluation of R-squared (R2) and Average Mean Error (AME) values. Starting with 400 samples, the number of samples increased incrementally until reaching the final count of 1400. It is important to note that the primary objective of this experiment is to understand the limitations of the computational tool. Hence, the chosen number of samples is not necessarily enough to represent a faithful model description. Furthermore, a testing set for cross-validation purposes was created using a LHS design with 200 samples. This additional data set allowed for further validation and evaluation of the model's performance.

Using the generated samples and applying Gaussian process regression, the cross-validation R2 and AME values were obtained and are presented in Table 7 and Table 8, respectively. The results indicate that, despite testing various parameter combinations, sections 3, 4, and 5 showed inadequate approximations to the actual model. Notably, section 5 exhibited a negative R2 value for the 0-degree regression, indicating a poor fit between the observed data and the model for this specific ply in that section. Therefore, it can be concluded that the model for section 5 does not accurately represent the observed data. The contrasting performance between different sections highlights the limited amount of testing data, particularly considering the nonlinearity inherent to the different load cases in each section. The observed discrepancy indicates the need for a larger training set to better capture the complex relationships between the independent variables and the response. Given the significant number of independent variables involved, increasing the sample size for the training set becomes even more crucial in order to achieve more robust and accurate results.

Table 7 - Wingbox R2

#	45° -R2	90° -R2	0° -R2
Section 1	0.752	0.798	0.727
Section 2	0.809	0.719	0.859
Section 3	0.528	0.529	0.522
Section 4	0.251	0.189	0.415
Section 5	0.116	0.865	-0.349
Section 6	0.645	0.801	0.836

Table 8 - Wingbox AME

#	45°-AME	90°-AME	0°-AME
Section 1	0.071	0.065	0.075
Section 2	0.071	0.093	0.065
Section 3	0.283	0.287	0.290

Section 4	0.123	0.131	0.111
Section 5	0.171	0.063	0.193
Section 6	0.042	0.032	0.030

Despite acknowledging the suboptimal quality of the data for this particular problem, the decision was made to proceed with the optimization process. The aim is to gain a deeper understanding of the limitations of the regression model and the relationship between problem complexity and the quantity of samples necessary for achieving robust optimization results. By continuing with the optimization, valuable insights can be obtained regarding the challenges posed by inadequate data quality and the potential strategies for improving the accuracy and reliability of the results. This approach allows for a thorough exploration of the problem space and provides an opportunity to identify the key factors that influence the optimization outcomes, even under less-than-ideal data conditions.

5.6.4 Results and conclusions

After setting the gaussian process parameters for the regression, the genetic algorithm was applied to optimize the weight of the six different sections. At this point a population sensitivity analysis was performed, where it was established that after a population of 1000 individuals generated for each cycle the weight minimum result did not have any gain. Still a crossover rate of 90% of the population and a mutation in 20% of the population, in 20% of their bits, was established. Moreover, a lambda parameter of 1 was established. Another important consideration is that the Average Mean Error (AME) value is incorporated with the failure index obtained from the regression for each individual ply within each section. This inclusion of the AME value helps to mitigate the potential shortcomings of a poor regression and ensures that the results remain valid. By combining the AME value with the failure index, a more conservative approach is taken, which can help in avoiding unreliable or inaccurate results. This cautious approach accounts for the uncertainties introduced by the regression model and contributes to maintaining the overall validity and reliability of the optimization process.

From the described hypothesis, the problem converged to a layup solution, presented in Table 9, in 52 iterations having more 100 iterations for avoiding local minimums. It is worth remembering that the presented layup represents half of the number of layers considering that it is a symmetric layup. Still, the number of layers presented in the column named “45°” represents the number of layers in positive and negative, each individually.

Table 9 - Wingbox optimized layup.

#	45°-Number of Plies	90°-Number of Plies	0°-Number of Plies
Section 1	0	6	0
Section 2	2	8	8
Section 3	12	8	15
Section 4	2	0	4
Section 5	2	6	0
Section 6	0	0	2

After obtaining this result, a cross validation adding the layup to the finite element model in ABAQUS was performed. From this, the graphical representation of the maximum

Tsai-hill distribution displayed in the envelope mode, i.e. though all integration points of all plies (Figure 110 and Figure 111) was analyzed.

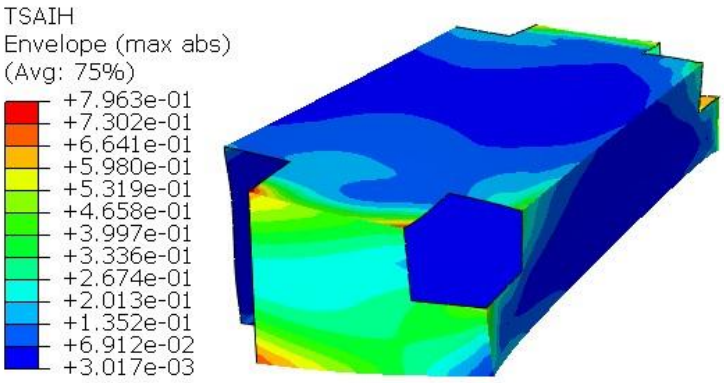

Figure 110 - ABAQUS graphic representation of the resultant layup, view 1.

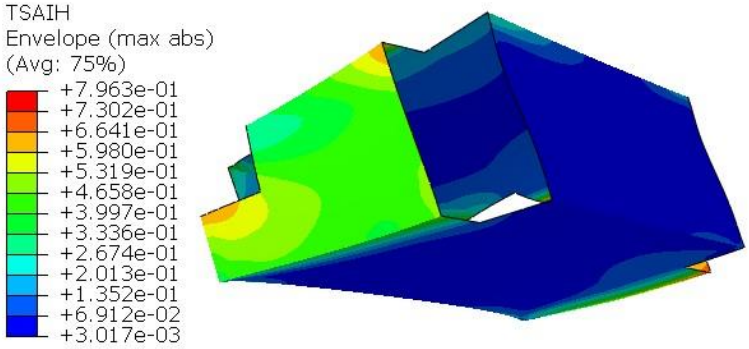

Figure 111 - ABAQUS graphic representation of the resultant layup, view 2.

Despite presenting an interesting insight of failure index distribution through the sections which were focus of the optimization process, it is essential to present the obtained values of the maximum Tsai-Hill values from each ply in each section from the generated report. These values are presented in Table 10.

Table 10 – Tsai-Hill values per section from ABAQUS report.

#	Tsai-Hill 45°	Tsai-Hill 90°	Tsai-Hill 0°
Section 1	-	0.74	-
Section 2	0.73	0.75	0.74
Section 3	0.70	0.70	0.69
Section 4	0.65	-	0.64
Section 5	0.53	0.53	-
Section 6	-	-	0.29

From the presented results it is possible to conclude that the sections that presented a good gaussian regression metrics had a more optimized result, of around 0.75 Tsai-Hill failure index, while the others had an even more conservative layup. This also showed that the regression model was predicting failure with a positive error, it means the regression was pointing to failure before the finite element model. Still, it is important to mention that Section

6 presented a low number of layers and that can be disregarded because it has all degrees of freedom constrained by both vertical edges.

From comparing some predictions from the regression model to apart values obtained from ABAQUS, especially the ones with layers in one orientation and zero layers in the others, it was possible to verify the difficulty the model had in correctly identifying failure in these layups. This suggests that it would be necessary to increase the number of samples, particularly, in the region close to zero plies, to better describe the design space. Still by the verification of the plots of the variation of Tsai-Hill values for each ply in each section, presented in Appendix A, it is possible to conclude that the multiple orientations of plies presented in the solution is not unexpected, since it is possible to verify the influence of those plies in the reduction of the failure index Tsai-Hill, which can help ascertain that the observed result is not necessarily indicative of a malfunctioning in the Genetic Algorithm.

In short it is possible to conclude that despite obtaining valid results, the layups do not appear to be optimized with some sections presenting values far from failure, which suggests the necessity of more samples for the training set. From the regression evaluation metrics and cross validation of results, it is possible to attribute this to the number of independent variables and levels of the variables being large, it increases exponentially the number of possible combinations which leads to a more complex problem. Another factor for that is the diversity in the different load cases considering different structural elements. This also leads to a high level of nonlinearity on the problem, which consequently requires a substantial number of samples and significant computational power to adequately address these complexities and achieve optimized layup designs.

To address the limitation of resources and reduce the nonlinearity of the problem, a possible approach is to fractionate the problem and optimize different groups of structural elements separately. This strategy not only helps in reducing the number of variables but also mitigates the complexities associated with the nonlinearity of the problem. Despite the mentioned advantages of splitting the problem, it is important to follow a logical order of optimization for the structural elements and iterate through the process. In the case of the wing, starting with the optimization of skins and moving on to spars and ribs. For weight optimization this logical order occurs, defining over defined spars and ribs, by reducing at its maximum the skin weight, structural element whose has the greater area. This approach ensures a systematic and controlled optimization sequence. Although there are interactions and dependencies between the elements, the incremental optimization process gradually converges to a final optimized solution, balancing the trade-offs between different structural elements.

6 Medical UAV Wing Optimization

6.1 Sections to be Optimized and Hypothesis

6.1.1 General Hypothesis

Considering the significant number of variables involved, optimizing all sections of the structural elements together would result in a large number of independent variables. This would require a substantial number of samples and significantly increase the computational time. It is estimated that this approach would lead to regression models with approximately 30 independent variables. Furthermore, based on the findings from the pseudo-wingbox test, it was observed that the relationship between variables in different types of structural elements is less direct, making the regression problem more complex. To address these challenges, the decision was made to proceed with individual optimization of each type of structural element, while keeping the layup of the others fixed. This approach allows for a more focused analysis and simplifies the regression problem. For splitting the problem, it was defined the order of optimization of the structural elements moving on from the Skin (Greater area) to spars and ribs.

6.1.2 Skin

To initiate the skin optimization process, an over defined layup configuration was chosen for the ribs, main spar, and secondary spar. This configuration includes four layers in all orientations for the ribs and secondary spar, and six layers for the main spar. Additionally, the entire structure was divided into two different bays. Each bay is characterized by two separate composite layups, one for the upper skin and one for the lower skin. This hypothesis came from the necessity of reducing the number of independent variables to the problem since the available computational power is low for performing the regression with many samples. Still, this hypothesis allows the easy manufacturing of two different types of wing panels, as the First Aircraft (prototype), with one central panel different from the tip panels. As a result, this assumption introduces a problem with four independent composite layups, corresponding to a total of twelve independent variables. Figure 112 represents the upper skin different layups, and Figure 113 the lower skin ones.

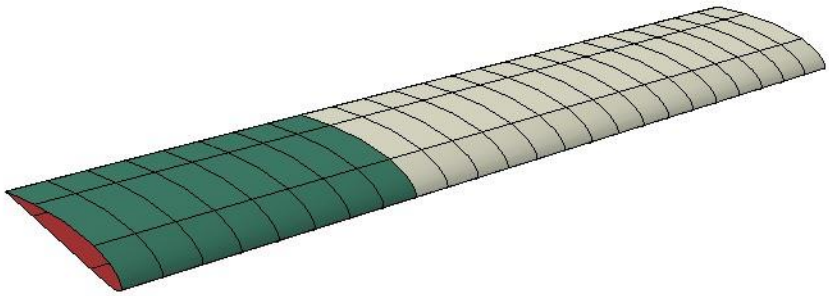

Figure 112 - Wing optimization sections, view upper skin.

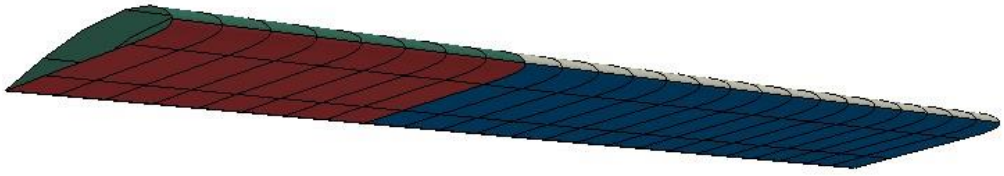

Figure 113 - Wing optimization sections, view lower skin.

In addition to the mentioned considerations, the analysis focuses solely on the mesh elements of the skin located between the two spars, excluding the leading and trailing edge skin. This decision is based on the understanding that this specific region experiences the highest stress levels in a wing structure. By excluding the leading and trailing edge skin from the post-processing phase, the computational cost is reduced. It is important to note that even though they are not considered in the construction of the regression model, the leading and trailing edge are accounted for in the finite element analysis. Additionally, the elements between the first and second rib of the first bay are excluded from the analysis due to their proximity to the boundary conditions. It is worth mentioning that the study area could be further refined by selecting a smaller critical region. The analyzed regions are represented in Figure 114.

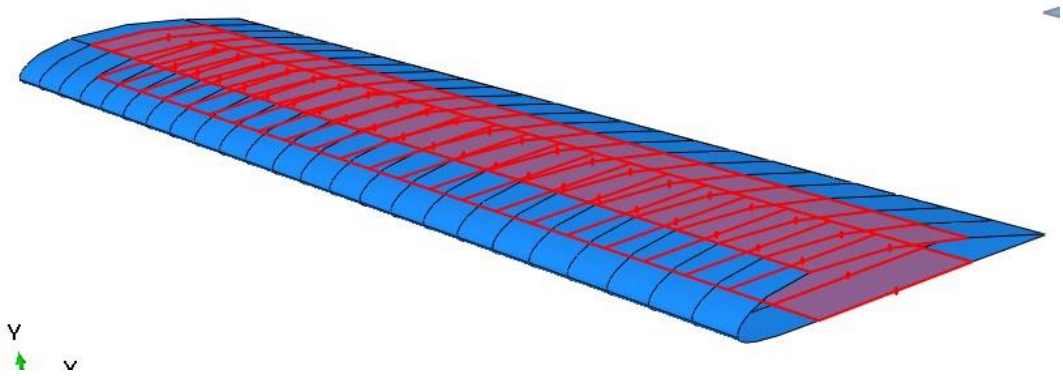

Figure 114 - Regions for skin analysis

6.1.3 Spars

The optimization of the spars will commence after determining the initial optimized layup for the skins, which will be fixed to the model along with the pre-defined ribs layup. Similar to the previous case, four optimization sections will be defined: the root section of the main spar (Section 1), the tip section of the main spar (Section 2), the root section of the secondary spar (Section 3), and the tip section of the secondary spar (Section 4). This distribution aligns with the previously established two bays and results in a total of 12 independent variables. By having a smaller area and fewer mesh elements it is anticipated that the surrogate model construction will require less computational time for the samples obtention. Figure 115 illustrates the different optimization sections, while Figure 116 depicts the area of optimization by removing the boundary conditions as the skin optimization hypothesis.

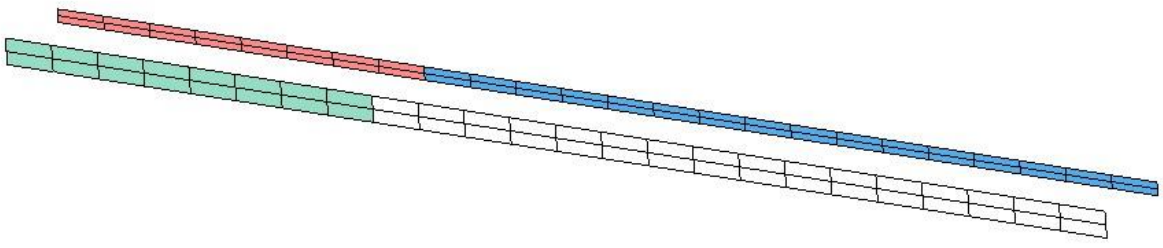

Figure 115 - Spar optimization sections.

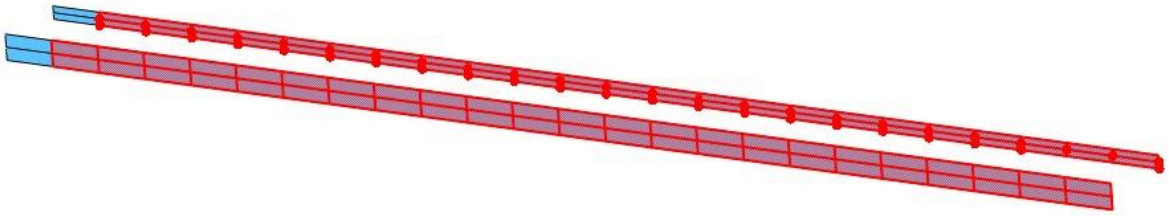

Figure 116 - Regions for spar analysis.

It is worth noting that the chosen study area presents a suboptimal condition due to the application of loads along the midline of both spars at the intersection with the ribs. However, as shown in Figure 117 and Figure 118, the localized loads do not seem to significantly disrupt the stress distribution in this region. Therefore, the decision was made to proceed with the analysis while excluding only the boundary conditions, acknowledging the potential disturbance in the results. It is important to recognize that in an ideal scenario, the model construction would require adaptations to better reflect the actual conditions.

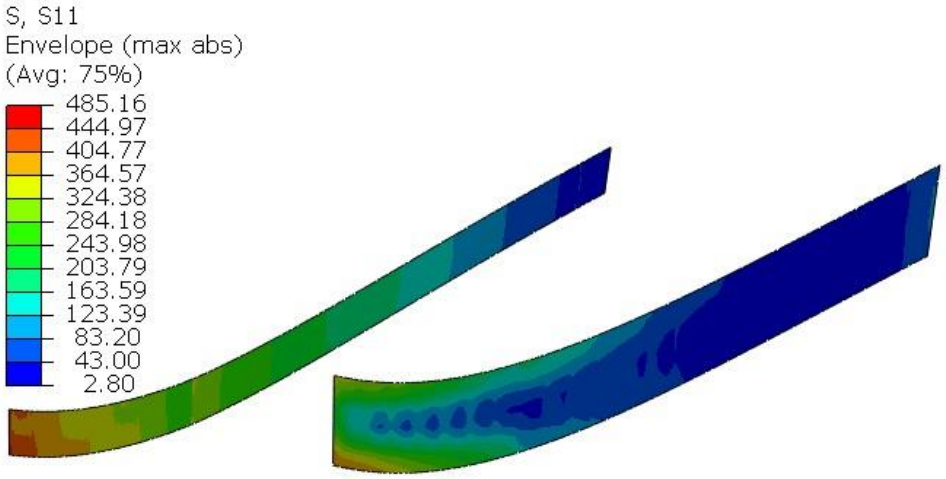

Figure 117 - Stress distribution for S11 in the spars.

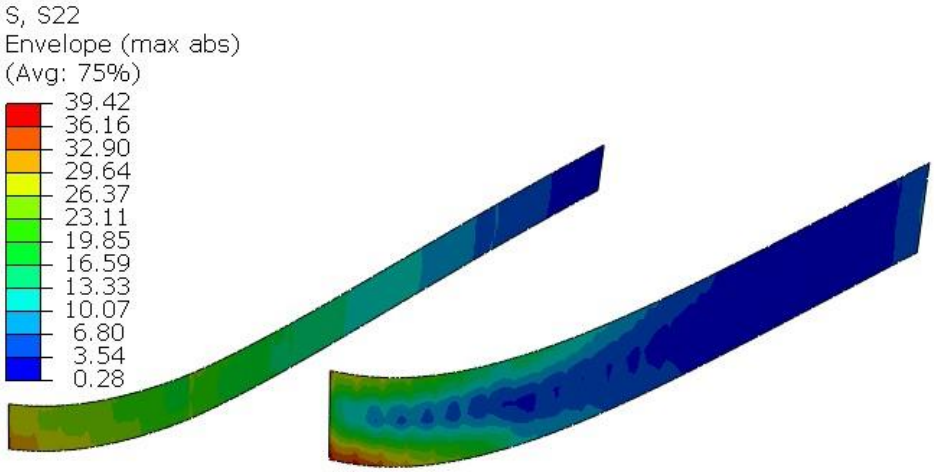

Figure 118 - Stress distribution for S22 in the spars.

6.1.4 Ribs

The optimization of the ribs starts after determining the initial optimized layup for the skins and spars which will be fixed to the model. Different from the previous cases, two

optimization sections will be defined: the ribs that correspond to the first bay (Section 1) and the ribs that correspond to the tip bay of the wing (Section 2). This distribution aligns with the previously established two bays and results in a total of 6 independent variables. This model is expected to be less computationally expensive when compared to the others because the post processing will run only two times per cycle, because of the two different sections. As well as it is expected that the regression model will require less samples for converging for having half of the independent variables. Figure 119 illustrates the different optimization sections, while Figure 120 depicts the area of optimization by removing the boundary conditions as the skin optimization hypothesis.

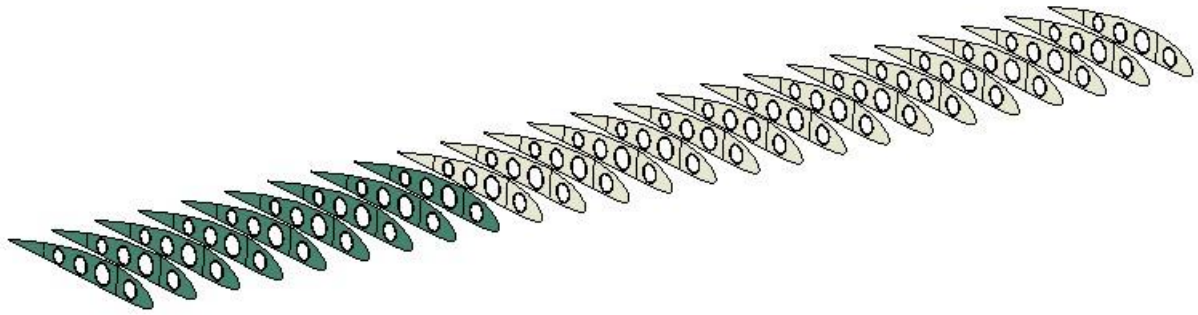

Figure 119 - Ribs optimization sections.

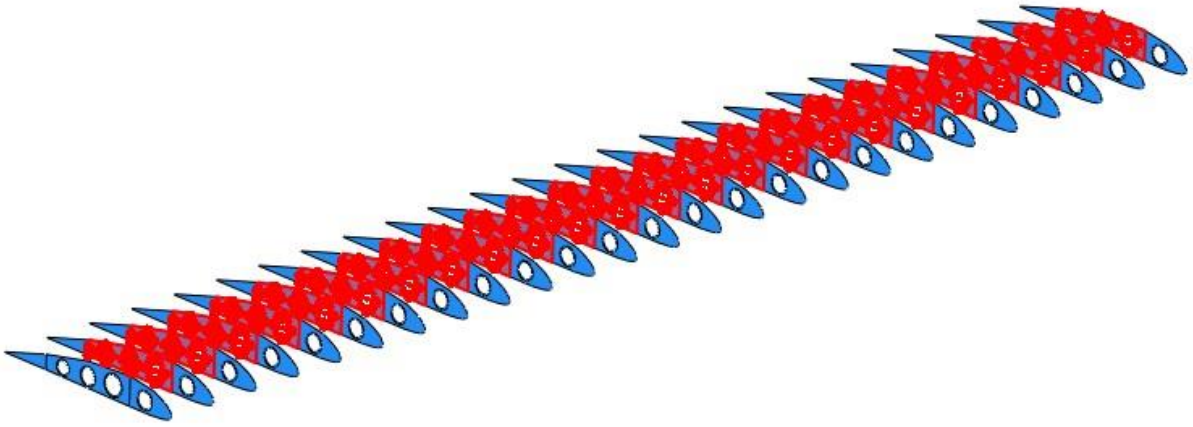

Figure 120 - Regions for spar analysis.

It is worth noting that the chosen study area presents a suboptimal condition due to the application of loads along the midline of both spars at the intersection with the ribs, in this case in the middle of the two vertical edges of the ribs. However, as shown in Figure 121 and Figure 122, the localized loads do not seem to significantly disrupt the stress distribution in this region and it is possible to verify the concentration of loads around the ribs holes. Therefore, the decision was made to proceed with the analysis while excluding only the boundary conditions, acknowledging the potential disturbance in the results. It is also worth mentioning that the study area could be further refined by selecting a smaller critical region.

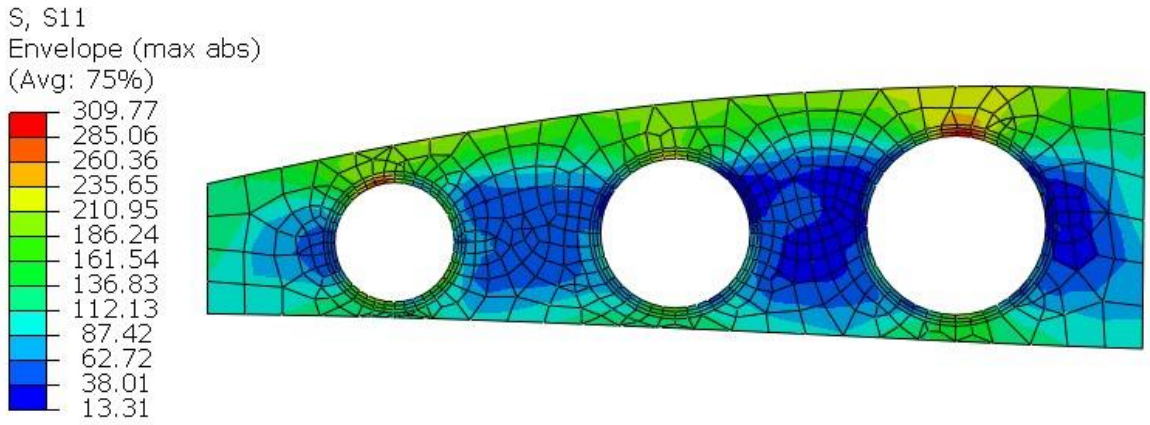

Figure 121 - Stress distribution for S11 in the ribs.

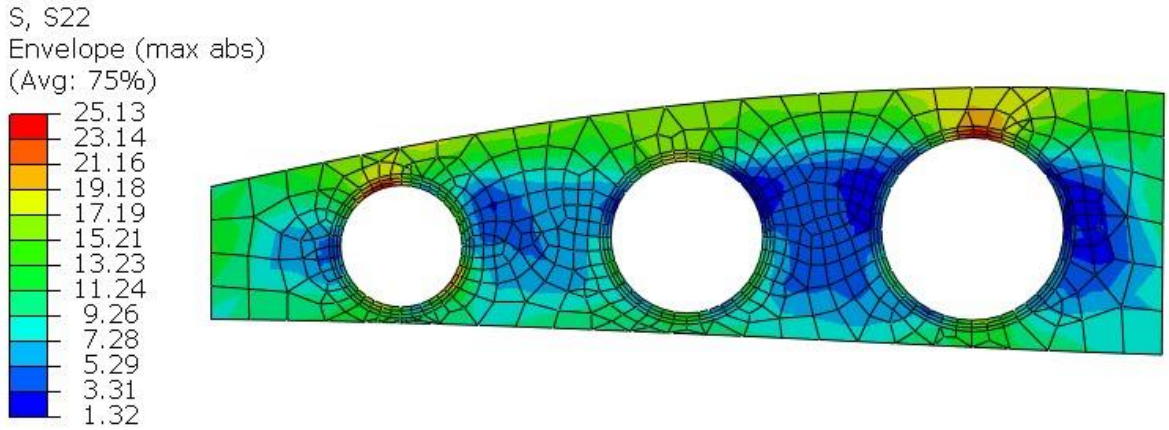

Figure 122 - Stress distribution for S22 in the ribs.

6.2 FEM model

6.2.1 Model Assumptions

The modeling process was conducted using a single part approach to avoid complexity assuming iterations and ensure the connectivity of all structural elements. Also, the developed model considered half of the wing structure, with a specific assumption of no displacement at the root. This assumption may result in an artificially stiffer representation of the wing structure. Ideally, for a comprehensive analysis of the entire wing structure, it would be necessary to include a portion of the fuselage structure as well, enabling the examination of the wing-fuselage connection. However, in this analysis, the decision was made to model only half of the wing and exclude the region near the boundary conditions of analysis. Consequently, the structural elements between the first two ribs are not included in the failure analysis.

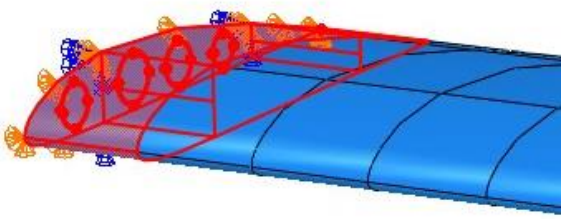

Figure 123 - BC region excluded from analysis.

The modeling process was conducted with the x-axis aligned to the chord length of the wing, with positive values directed towards the trailing edge. The y-axis was defined in the direction of the airfoil thickness, with positive values pointing upwards. The z-axis was chosen to align with the wingspan, with positive values extending from the root to the tip of the wing. Additionally, the reference point (0,0,0) was fixed at the zero point of the airfoil of the first rib (N1). The model from these assumptions is illustrated in Figure 124.

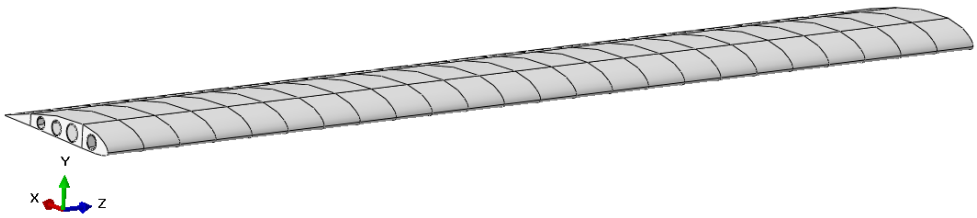

Figure 124 - Wing Finite Element Model

It is important to present the shell normal for each structural element, as it is reference for the locations from ABAQUS reports considering that fraction 1 indicates the positive direction of the normal, while -1 represents the negative direction [32]. Another important factor to be defined is the direction of the 0-degree reference orientation. This information is crucial when studying the stresses and reading the results from the final layup resultant from the optimization tool.

- Upper skin reference orientations, Figure 125:

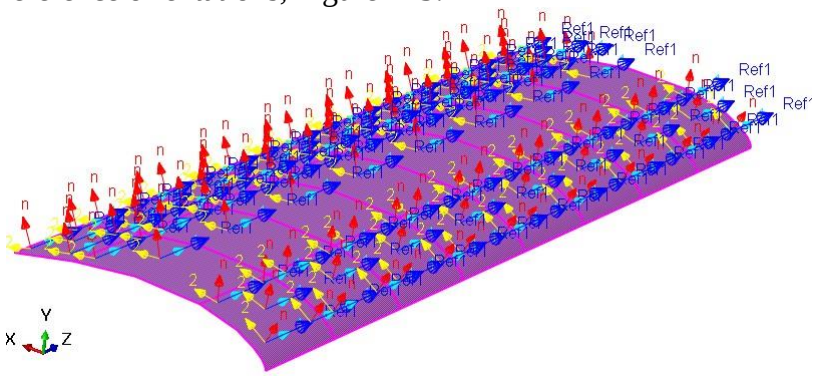

Figure 125 - Shell reference upper skin

- Lower skin reference orientations, Figure 126:

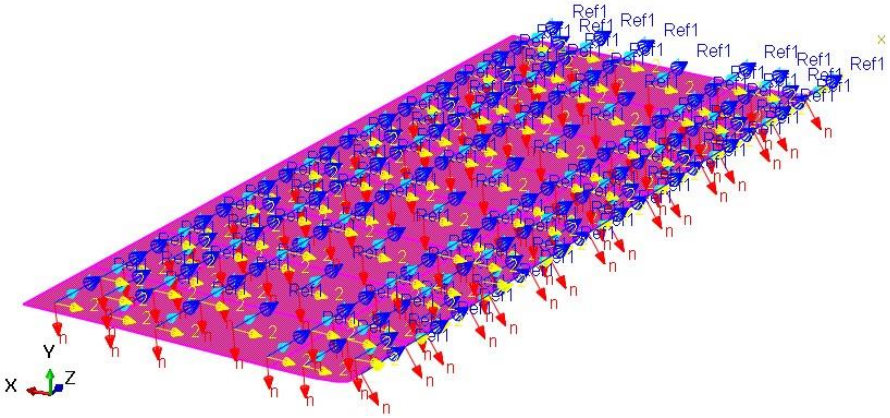

Figure 126 - Shell reference lower skin

- Main spar reference orientations, Figure 127:

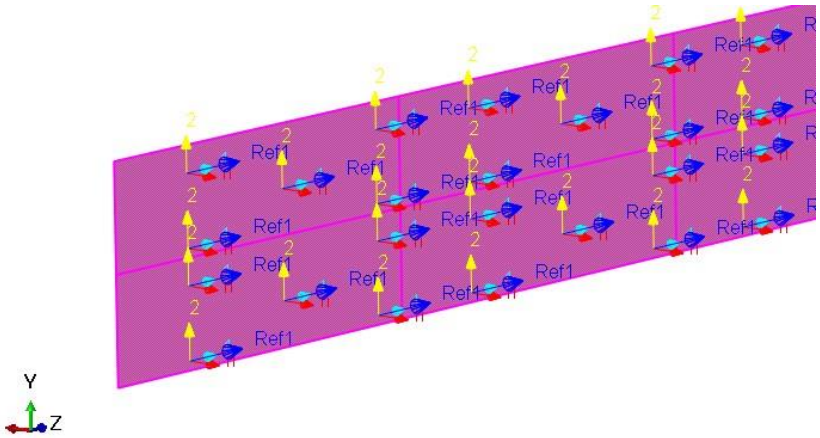

Figure 127 - Shell reference main spar

- Secondary spar reference orientations, Figure 128:

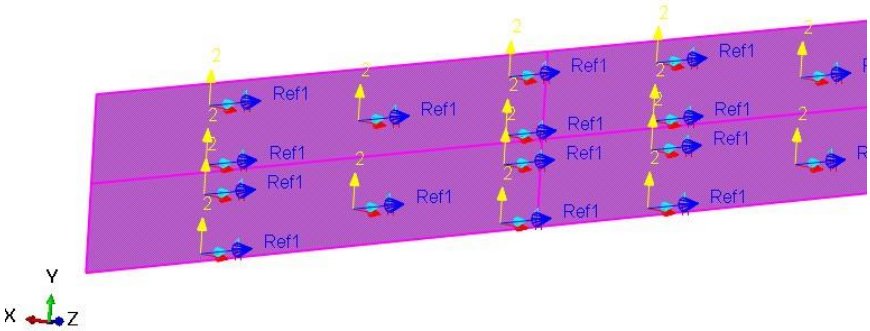

Figure 128 - Shell reference secondary spar

- Ribs reference orientations, Figure 129:

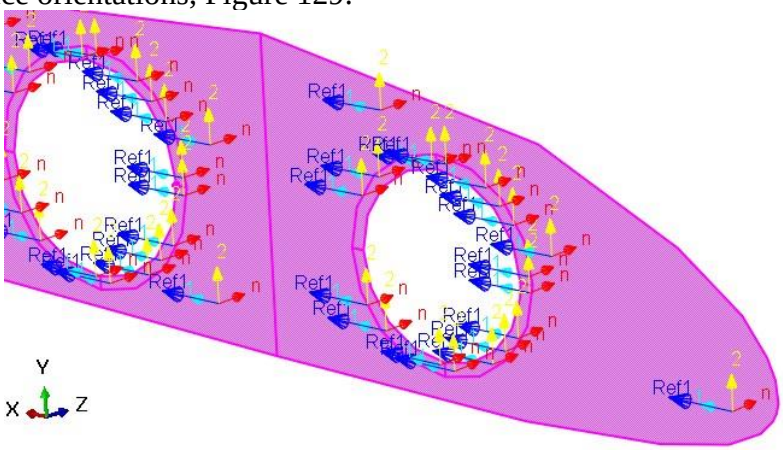

Figure 129 - Shell reference ribs

The composite layup for the complete wing structure follows a symmetric pattern and adheres to the assumption of varying only the thickness of each ply, with a multiple of the laminate thickness as the number of plies. The chosen layup configuration is $[0/90/45/-45]_s$, with the zero-degree ply positioned on the outermost layers. This configuration is selected based on the idea of considering a bending case in the structure, where having zero-degree ply on the outside results in lower stress values. It is important to note that the difference in the stress levels between these assumptions can be minimal, depending on the order, because it depends on the relative distance from the neutral axis of the structure to the skin plies. To validate the choice of layup, a comparative analysis was conducted on a generic wing box structure [66],

shown in Figure 130. The comparison of maximum Tsai-Hill failure index values in the symmetric panels of the generic wing box (Figure 131 to Figure 134). This comparison demonstrated a great advantage of the selected layup configuration.

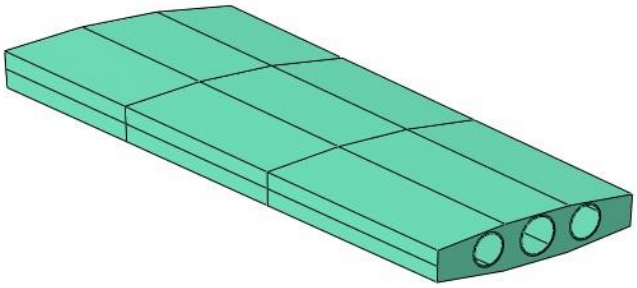

Figure 130 - Wingbox for finding better layer orientation order.

- $[0/90/+-45]_s$

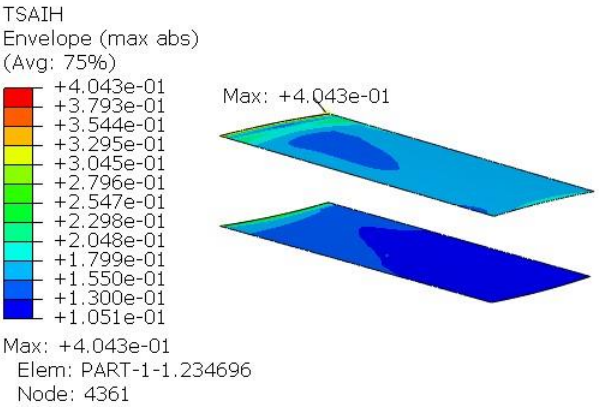

Figure 131, - Maximum Tsai-Hill for [0,90,45], wingbox testing.

- $[90/0/+-45]_s$

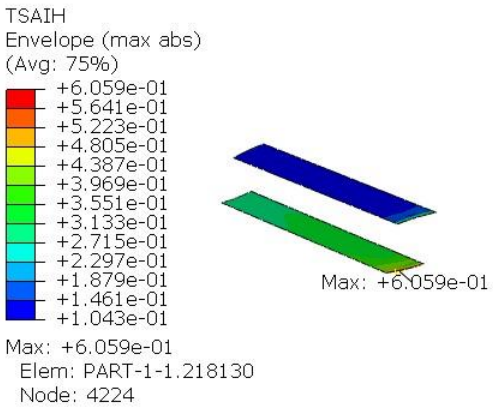

Figure 132 - Maximum Tsai-Hill for [90,0,45], wingbox testing.

- $[+-45/0/90]_s$

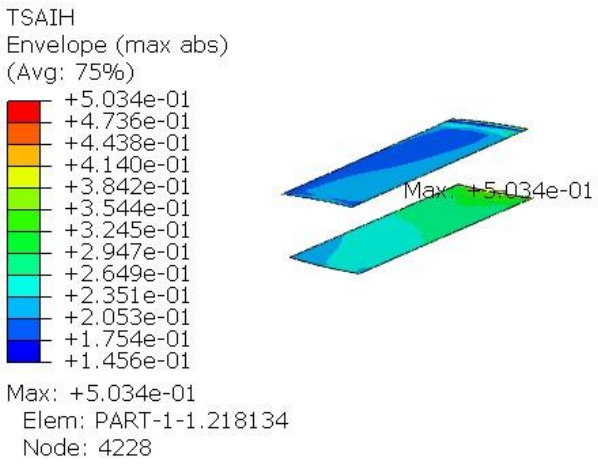

Figure 133 - Maximum Tsai-Hill for [45,0,90], wingbox testing.

- $[+-45/90/0]_s$

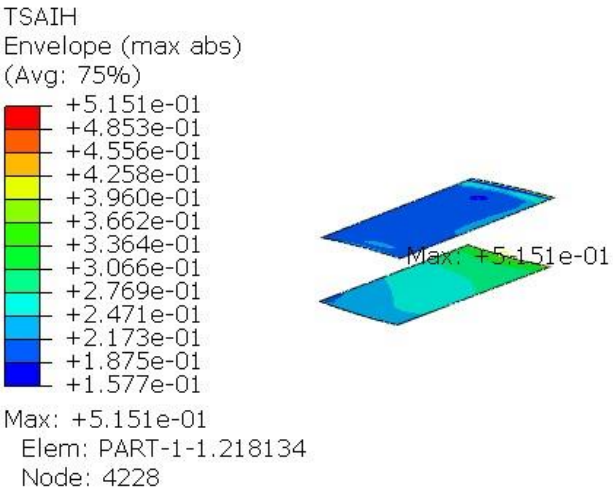

Figure 134 - Maximum Tsai-Hill for [45,90,0], wingbox testing.

6.2.2 Material Properties

The material properties of the selected unidirectional CFRP laminate for input in ABAQUS are summarized in Table 11 for the elastic properties and Table 12 for the failure properties. It is important to note that the laminate thickness (t) is 0.08 [mm] for each ply, and the specific mass of the material (ρ_{CFRP}) is $1.9*10^{-9}$ [tonne/mm^3].

Table 11 - Material properties, elastic.

Elastic Properties								
E1	E2	E3	ν12	ν13	ν23	G12	G13	G23
[MPa]	[MPa]	[MPa]	[-]	[-]	[-]	[MPa]	[MPa]	[MPa]
100000	10000	10000	0.34	0.34	0.34	5400	5400	3050

Table 12 - Material properties, failure.

Failure Properties				
Stress				
Xt_1	Xt_2	Xc_1	Xc_2	Xsh
[MPa]	[MPa]	[MPa]	[MPa]	[MPa]
1400	47	930	130	53
Strain				
eps_t_1	eps_c_1	eps_t_2	eps_c_2	eps_sh
[-]	[-]	[-]	[-]	[-]
0.025	0.01	0.002	0.018	0.03

Where:

• E1 is the composite stiffness along the fiber direction.

• E2 is the composite in-plane stiffness in the direction perpendicular to the fiber direction.

• E3 is the transverse lamina stiffness.

• G12 and G13 are the in-plane shear modulus.

• G23 is the transverse shear modulus.

• ν12 is the in-plane 1-2 Poisson ratio.

• Xt_1 is the longitudinal tensile failure stress.

• Xc _1 is the longitudinal compressive failure stress.

• Xt_2 is the transverse tensile failure stress.

• Xc_2 is the transverse compressive failure stress.

• Xsh is the in-plane shear failure stress.

• eps_t_1 is the longitudinal tensile failure strain.

• eps_c_1 is the longitudinal compressive failure strain.

• eps_t_2 is the transverse tensile failure strain.

• eps_c_2 is the transverse compressive failure strain.

• eps_sh is the shear failure strain.

6.2.3 Boundary Conditions

Considering that displacements and rotations for the section closer to the root of the wing-box are relatively small, it was assumed the approximation of the zero displacement at this region. Still, it is important to say that according to the De Saint-Venant principle, the complete clamp of the first rib would create an unrealistic stress concentration and an artificial over-stiffness of the hole structure. For this reason, it was opted to only clamp (U1=U2=U3=UR1=UR2=UR3=0) the vertical edges of the main and secondary spars, in the first rib (N1) region, while simply supporting (U1=U2=U3=0) the edges of the rib-skin region. This approach was adopted to mitigate the stress concentration at the mentioned region also conform with the NACA3781 hypothesis that considers the region of the frame of the ribs, as simply supported. The following Figure 135 helps to illustrate the boundary conditions assumptions.

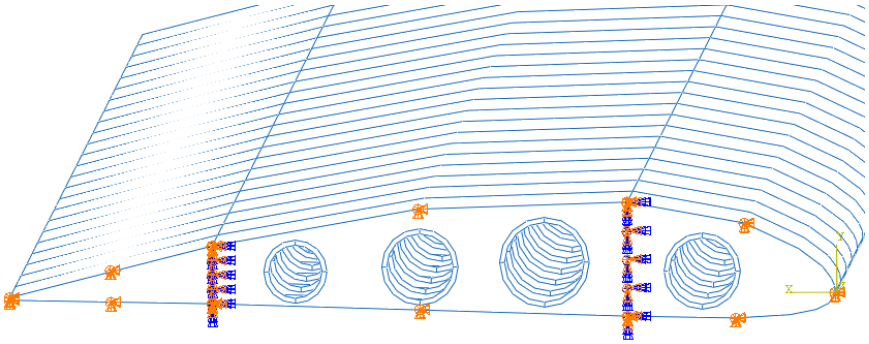

Figure 135 - Boundary Conditions

6.2.4 Aerodynamic Load Application

From the aerodynamic loading distribution previously described in Section 4.2, and having the model geometry and properties defined, it is possible to proceed by the application of the loads to the model. First it is important to highlight that despite in the following presented equations and tables the Y and Z axis are changed on applying the loads to the model it was considered the right previously described by Figure 124 reference system. The aerodynamic distribution along the wingspan is detailed in Table 5, which can be found in Section 4.2. The chosen way of application of these loads was directly applying a system of equivalent concentrated forces at the intersection of the spars and ribs, guaranteeing that there are regions away from the points of application of the loads that are not incorrectly deformed due to the concentrated forces applied. The ideal application of forces would be in the aerodynamic center, it means around 25% of the chord and between 50% and 60% of the wing-foil thickness, vertically, that can also be approximated by applying then in the central line of the spars. It is worth noting that a total of 25 ribs are present, with the first rib (N1) subjected to the boundary conditions. Consequently, the decision was made to distribute these loads by applying them to the remaining 24 ribs. To approximate the load acting on each rib, an evaluation can be performed by considering the area beneath the curves for *vz* [N/m], *vx* [N/m], and *my* [N] within a region obtained by uniformly dividing the wingspan around each rib. Furthermore, it is important to highlight that these areas were determined by placing the rib at the central position of this region, with the limits of integration defined as half the distance between adjacent ribs on each side. By adopting this approach, an estimation of the load distribution on each rib can be obtained. It is worth mentioning that the last rib (N24) has intervals of integration from half of the distance before it to its own distance, and since the first rib (N1) is under boundary conditions, the second rib (N2) boundary limits of integration is considered to start from the first rib's position. As result it is possible to find the Lift (Vz [N]), Drag (*Vx* [N]) and Pitching moment (*My* [N*n]) at 25% of the chord of each rib. The data obtained by these calculations is shown in Table 13, and it is important to note that the loads are approximations with induced numerical errors, from the obtention of the data, interpolation methods of the unknown values and for the trapezoidal integration.

Table 13 - Equivalent aerodynamic loads in rib positions.

Rib ID	Rib Position	Lim of Integ		Vz [N]	Vx [N]	My [N*m]
-	[mm]	[mm]		[N]	[N]	[N*m]
n1	0	-	-	-	-	-
n2	62.5	0	93.75	48.40	1.57	20.29
n3	125	93.75	156.25	32.21	1.06	13.60
n4	187.5	156.25	218.75	32.17	1.07	13.66
n5	250	218.75	281.25	32.09	1.08	13.76
n6	312.5	281.25	343.75	32.01	1.10	13.87
n7	375	343.75	406.25	31.90	1.12	13.99
n8	437.5	406.25	468.75	31.78	1.14	14.13
n9	500	468.75	531.25	31.62	1.17	14.32
n10	562.5	531.25	593.75	31.45	1.21	14.52
n11	625	593.75	656.25	31.23	1.25	14.74
n12	687.5	656.25	718.75	30.98	1.29	15.00
n13	750	718.75	781.25	30.69	1.34	15.30
n14	812.5	781.25	843.75	30.33	1.40	15.63
n15	875	843.75	906.25	29.91	1.46	16.00
n16	937.5	906.25	968.75	29.40	1.54	16.39
n17	1000	968.75	1031.25	28.79	1.62	16.83
n18	1062.5	1031.25	1093.75	28.05	1.71	17.32
n19	1125	1093.75	1156.25	27.11	1.80	17.78
n20	1187.5	1156.25	1218.75	25.91	1.90	18.21
n21	1250	1218.75	1281.25	24.36	1.99	18.50
n22	1312.5	1281.25	1343.75	22.27	2.05	18.42
n23	1375	1343.75	1406.25	19.28	2.03	17.52
n24	1437.5	1406.25	1468.75	14.44	1.78	19.52
n25	1500	1468.75	1500	3.96	0.60	26.48

The next approximation made is presented in Figure 136, and it is that the vertical forces are distributed in such a way to create equivalence also for the aerodynamic moment (*My*). For the drag loads (*Vx*), they can be approximated by their application only in the main spar.

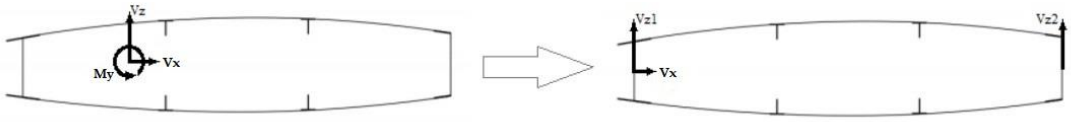

Figure 136 - Aerodynamic loading decomposition

Under the specified assumptions, the initial step is to estimate the equivalent vertical forces, Vz_1 and Vz_2, which are crucial for determining the load distribution. Assuming the aerodynamic center is positioned at 25% of the aerodynamic chord and taking into account the relative positions of the spars (L1 at 25% and L2 at 75%) with respect to the chord, a system of equations is formulated as presented in Equation 35. The solution to this system is obtained using Equation 36.

$$\begin{cases} \mathrm{Vz} = \mathrm{Vz}_1 + \mathrm{Vz}_2 \\ \mathrm{My} = \mathrm{Vz}_1\,(\mathrm{l1} - 0.25)\,\mathrm{c} + \mathrm{Vz}_2\,(\mathrm{l2} - 0.25)\,\mathrm{c} \end{cases} \tag{35}$$

$$\begin{cases} \mathrm{Vz}_1 = -\dfrac{\frac{\mathrm{My}}{\mathrm{c}} + \mathrm{Vz}(\mathrm{l2} - 0.25)}{\mathrm{l2} - \mathrm{l1}} \\ \mathrm{Vz}_2 = \dfrac{\frac{\mathrm{My}}{\mathrm{c}} + \mathrm{Vz}(0.25 - \mathrm{l1})}{\mathrm{l2} - \mathrm{l1}} \end{cases} \tag{36}$$

where l_i represents the relative position of the spar *Li* on the aerodynamic chord of length *c*.

The calculation results in the determination of the equivalent vertical forces, Vz_1 (negative, directed towards the ground) and Vz_2 (positive), as shown in Table 14.

Table 14 - Equivalent lift couple for ribs.

Rib ID	Rib Position	Vz1 [N]	Vz2 [N]
-	[mm]	[N]	[N]
n1	0	0	0
n2	62.5	-113.94	162.35
n3	125	-76.59	108.81
n4	187.5	-77.15	109.32
n5	250	-77.99	110.08
n6	312.5	-78.91	110.92
n7	375	-80.03	111.93
n8	437.5	-81.29	113.07
n9	500	-82.92	114.54
n10	562.5	-84.69	116.13
n11	625	-86.70	117.93
n12	687.5	-89.02	120
n13	750	-91.68	122.36
n14	812.5	-94.73	125.06
n15	875	-98.05	127.96
n16	937.5	-101.72	131.13
n17	1000	-105.88	134.67
n18	1062.5	-110.49	138.53
n19	1125	-115.15	142.26
n20	1187.5	-119.74	145.65
n21	1250	-123.66	148.03
n22	1312.5	-125.05	147.32
n23	1375	-120.85	140.13
n24	1437.5	-141.75	156.19
n25	1500	-207.86	211.82

Given that the finite element model has an angle of attack of 0°, it is essential to decompose both loads into their respective vertical and horizontal components. The decomposition process is illustrated in Figure 137, and their components can be obtained using Equation 37 to Equation 40.

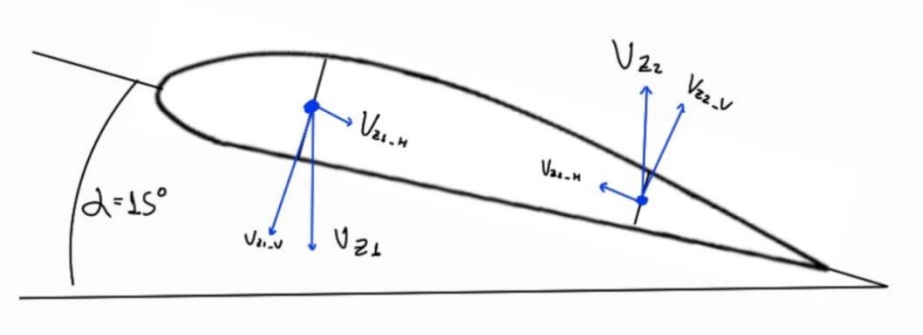

Figure 137 - Lift angle decomposition.

$$Vz_{1V} = Vz_1 \cos(15°) \tag{37}$$

$$Vz_{1H} = Vz_1 \sin(15°) \tag{38}$$

$$Vz_{2V} = Vz_2 \cos(15°) \tag{39}$$

$$Vz_{2H} = Vz_2 \sin(15°) \tag{40}$$

It is also necessary to account with the decomposition of the drag components, that are represented by the Figure 138 and obtained by the Equation 41 and Equation 42.

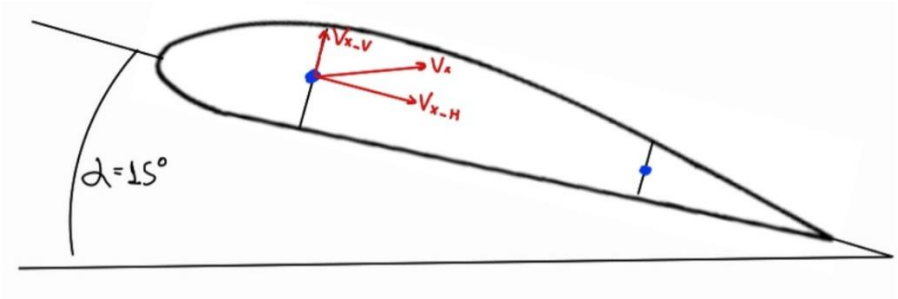

Figure 138 - Drag angle decomposition.

$$Vx_v = Vxsin(15°) \tag{41}$$

$$Vx_H = Vxcos(15°) \tag{42}$$

The decompositions previously explained are presented in Table 15, where it was applied a safety coefficient of 1.5 and a quality coefficient of 1.25.

Table 15 - Decomposed aerodynamic loads with safety and quality coefficients

Rib ID	Vz2 H	Vz2 V	Vz1 V	Vz1 H	Vx V	Vx H
-	SQF - [N]	SQF - [N]	SQF - [N]	SQF - [N]	SQF - [N]	SQF - [N]
n1	0	0	0	0	0	0
n2	-78.78	294.03	-206.36	55.29	0.76	2.84
n3	-52.8	197.06	-138.72	37.17	0.51	1.91
n4	-53.05	197.98	-139.73	37.44	0.52	1.93
n5	-53.42	199.37	-141.24	37.85	0.52	1.96
n6	-53.83	200.89	-142.92	38.29	0.53	1.99
n7	-54.32	202.73	-144.95	38.84	0.54	2.03
n8	-54.87	204.78	-147.22	39.45	0.56	2.07
n9	-55.58	207.44	-150.17	40.24	0.57	2.13
n10	-56.36	210.33	-153.38	41.10	0.59	2.19
n11	-57.23	213.59	-157.03	42.08	0.61	2.26
n12	-58.23	217.33	-161.23	43.20	0.63	2.34
n13	-59.38	221.61	-166.04	44.49	0.65	2.43
n14	-60.69	226.5	-171.57	45.97	0.68	2.54
n15	-62.1	231.75	-177.57	47.58	0.71	2.65
n16	-63.63	237.48	-184.23	49.36	0.75	2.79
n17	-65.35	243.9	-191.76	51.38	0.79	2.93
n18	-67.23	250.9	-200.10	53.62	0.83	3.09
n19	-69.04	257.65	-208.56	55.88	0.88	3.27
n20	-70.68	263.79	-216.86	58.11	0.92	3.45
n21	-71.83	268.09	-223.96	60.01	0.97	3.61
n22	-71.49	266.81	-226.47	60.68	1.00	3.72
n23	-68.01	253.8	-218.88	58.65	0.99	3.68
n24	-75.8	282.88	-256.73	68.79	0.86	3.22
n25	-102.8	383.63	-376.45	100.87	0.29	1.08

Lastly, the final loads to be applied to the finite element model can be obtained by summing the vertical components (Vz_{1V} and Vx_V) and horizontal components (Vz_{1H} and Vx_H). These loads are to be applied to the main spar. Additionally, the components Vz_{2V} and Vz_{2H} are to be applied to the secondary spar. The specific values for these final loads are presented in Table 16, considering the reference axis from ABAQUS. The model application is depicted in Figure 139 and Figure 140.

Table 16 - Equivalent aerodynamic loads for the Finite Element Model.

Rib ID	Vz MS H	Vz MS V	Vz2 H	Vz2 V
-	SQF - [N]	SQF - [N]	SQF - [N]	SQF - [N]
n1	0	0	0	0
n2	58.135	-205.6	-78.78	294.03
n3	39.083	-138.2	-52.8	197.06
n4	39.372	-139.2	-53.05	197.98
n5	39.805	-140.7	-53.42	199.37
n6	40.283	-142.4	-53.83	200.89
n7	40.868	-144.4	-54.32	202.73
n8	41.521	-146.7	-54.87	204.78
n9	42.366	-149.6	-55.58	207.44
n10	43.285	-152.8	-56.36	210.33
n11	44.336	-156.4	-57.23	213.59
n12	45.54	-160.6	-58.23	217.33
n13	46.921	-165.4	-59.38	221.61
n14	48.51	-170.9	-60.69	226.5
n15	50.234	-176.9	-62.1	231.75
n16	52.15	-183.5	-63.63	237.48
n17	54.315	-191	-65.35	243.9
n18	56.711	-199.3	-67.23	250.9
n19	59.151	-207.7	-69.04	257.65
n20	61.554	-215.9	-70.68	263.79
n21	63.62	-223	-71.83	268.09
n22	64.402	-225.5	-71.49	266.81
n23	62.33	-217.9	-68.01	253.8
n24	72.014	-255.9	-75.8	282.88
n25	101.95	-376.2	-102.8	383.63

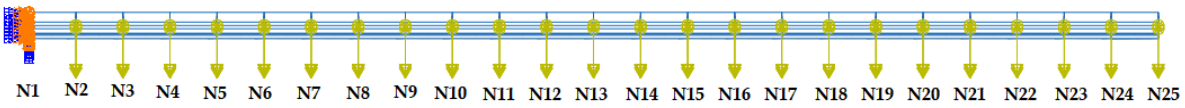

Figure 139 - Ribs' names and application of the forces.

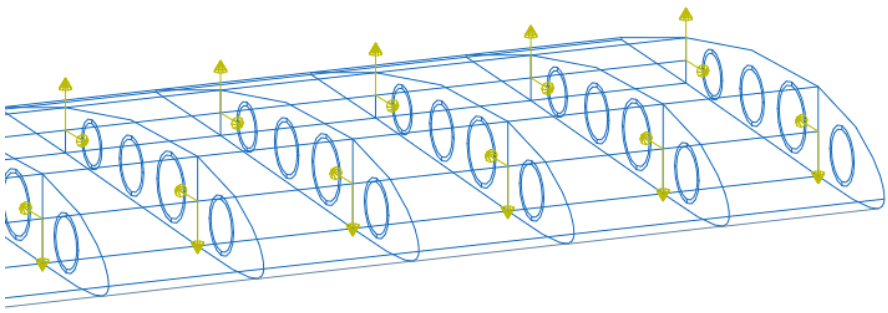

Figure 140 - Final aerodynamic loads in Finite Element Model.

6.2.5 Inertial Load Application

The inertial loads applied to the model stem from the structural weight of the wing. These loads account for the mass of the wing itself and are an important consideration in the analysis process. It's worth noting that these loads can vary with each cycle of the regression model construction due to updates in the wing's layup configuration. To calculate the inertial loads, the weight of each region is determined based on its area and the number of layers in the layup. This weight is then multiplied by the appropriate vertical and horizontal load factors to obtain the total inertial load for that specific region. These loads are automatically applied to the wing structure as part of the analysis. By considering the changing inertial loads based on the updated layup configuration, the model captures the evolving weight distribution and its

impact on the structural response. This approach enables a more accurate representation of the wing's behavior under different load conditions and helps in evaluating its performance and integrity.

In describing the assumptions adopted for this model, one key aspect is the consideration of splitting the half wing model in two independent bays within the wing structure. These bays serve as distinct sections, and the weight actualization is performed individually for each bay according to their layup. To accurately represent the weight distribution, the areal values of the main spar, secondary spar, upper skin, lower skin, and ribs of the root bay are enough to describe both bays, considering the rectangular geometry of the wing (constant chord). Still, it is important to highlight that this assumption is valid because of the areal relation between both bays, where the second bay (Tip Bay) is equal to two times the root bay. It means that the wing is divided into three equal parts where the first bay is 1/3 of the semi-span and the second bay is 2/3. These areal values are presented in the following Table 17 and the individual bay is the space between seven ribs, which is represented in Figure 141.

Table 17 - Areal values of the structural elements for 1/3 half wing

Element	Area [m^2]
Upper Skin	0.1308
Lower Skin	0.1258
Ribs	0.0411
Main Spar	0.0172
Sec. Spar	0.0087

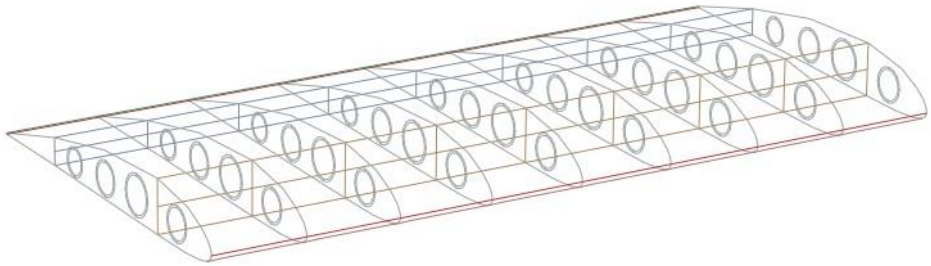

Figure 141 - Root Bay graphic representation.

For having the weight of the described bay 1 (root bay) in each cycle it is possible to appeal for the formulation described in Equation 43 and for bay 2 (tip bay) in Equation 44.

$$W_{bay1} = 9.81\rho_{CFRP}(A_{USkin}t_{US_i} + A_{LSkin}t_{LS_i} + A_{Ribs}t_{Ribs_i} + A_{MSpar}t_{MS_i} + A_{SSpar}t_{SS_i}) \quad (43)$$

$$W_{bay2} = 9.81\rho_{CFRP}2(A_{USkin}t_{US_i} + A_{LSkin}t_{LS_i} + A_{Ribs}t_{Ribs_i} + A_{MSpar}t_{MS_i} + A_{SSpar}t_{SS_i}) \quad (44)$$

where W_{bayk} is the weight of each bay, ρ_{CFRP} is the laminate specific mass and $A_{xx}t_{xx_i}$ is the fixed area of each structural element multiplied by its thickness in the cycle (i).

Once the weight for each iteration is determined, the next step involves establishing hypotheses for its application to the finite element model. Similar to the approach taken for the aerodynamic loads, the weight is distributed among the ribs within each bay. To achieve this, the total weight of a single bay is divided by eight in the case of the root bay and by sixteen for the tip bay, representing that each rib will bear a load corresponding to half of the rib spacing in each direction, with the rib itself being the center of this measurement. This hypothesis also considers that the rib shared between bays will carry half of its correspondent weight from one bay, as well as half of the weight from the adjacent bay's application. It is important to note that this weight has two components, the vertical inertial load and horizontal inertial load. These two components are obtained by multiplying the weight of the bay by the vertical load factor

(n_z) and the horizontal load factor (n_x). From all these assumptions it is possible to obtain the Vertical inertial load and Horizontal inertial load described in the formulation of Equation 45 and Equation 46, that are already multiplied by the safety factor of 1.5 and quality factor of 1.25.

$$IL_{vk} = 1.5 * 1.25 * \frac{WBay_k}{Nribsk} n_z \tag{45}$$

$$IL_{Hk} = 1.5 * 1.25 * \frac{WBay_k}{Nribsk} n_x \tag{46}$$

Where N_{ribsk} is the number of ribs in the bay *k*, it means eight for the root bay and sixteen to the tip bay.

It is known that the vertical load factor (n_z) for the specific load case has a value of 5.5. However, it is necessary to estimate the horizontal load factor (*nx*). For that it is used the formulation described in Figure 142, Equation 47 and Equation 48.

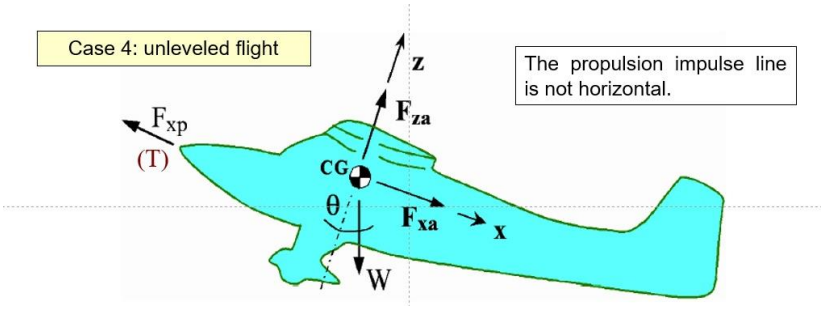

Figure 142 - Load Factors: Maneuver in Unleveled Flight.[67]

$$n_x = \frac{-T+F_{xa}}{w} \tag{47}$$

$$T = F_{xp}\cos(2°) \tag{48}$$

where the total weight of the aircraft, denoted as *W*, is measured as 235.44 N. Additionally, the horizontal component of drag, F_{xa}, has been calculated and amounts to 66.225 N. The thrust of the motor, denoted as F_{xp}, is determined to be 73.575 N, considering the propeller efficiency (testing data from the manufacturer [68]). These calculations yield a horizontal load factor of 0.031, which may seem atypical and possibly indicative of inconsistencies in drag estimation or due to the lightweight nature of the aircraft. Still, it is possible to include that the maximum load factor registered in the flight logs from the First Aircraft was around 1g. Nevertheless, it has been decided to proceed by adhering to the commonly accepted standard of a horizontal load factor (*nx*) for maneuvering of 1.5, as established by certain regulations.

Finally, the load corresponding to each rib is divided equally and applied to the regions of the main and secondary spar, as outlined in Equation 49 and Equation 50. Additionally, accounting for an angle of attack of 15°, the vertical and horizontal components of both inertial loads must be determined. This decomposition is visually represented in Figure 143, and its mathematical expressions are provided in Equation 49 to Equation 52.

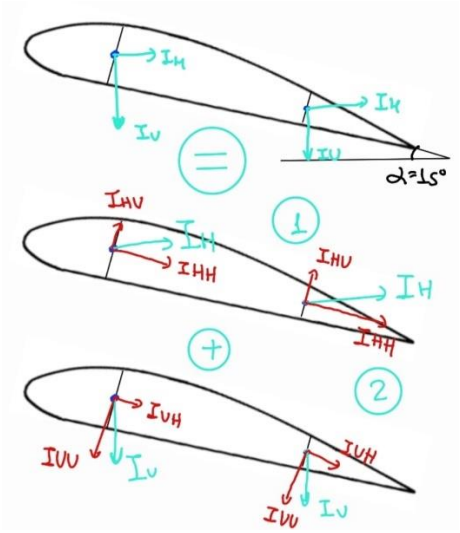

Figure 143 - Inertial loads decomposition.

$$I_{Hk} = \frac{IL_{Hk}}{2} \tag{49}$$

$$I_{Vk} = \frac{IL_{Vk}}{2} \tag{50}$$

$$1\begin{cases} I_{HV} = I_{H_k}\sin(15°) \\ I_{HH} = I_{H_k}\cos(15°) \end{cases} \tag{51}$$

$$2\begin{cases} I_{VV} = I_{V_k}\cos(15°) \\ I_{VH} = I_{V_k}\sin(15°) \end{cases} \tag{52}$$

The final load to be applied to each rib within a bay it is calculated by Equation 53 and Equation 54 and represented by Figure 144.

$$ILz_{bk} = I_{HV} + I_{VV} \tag{53}$$

$$ILx_{bk} = I_{HH} + I_{VH} \tag{54}$$

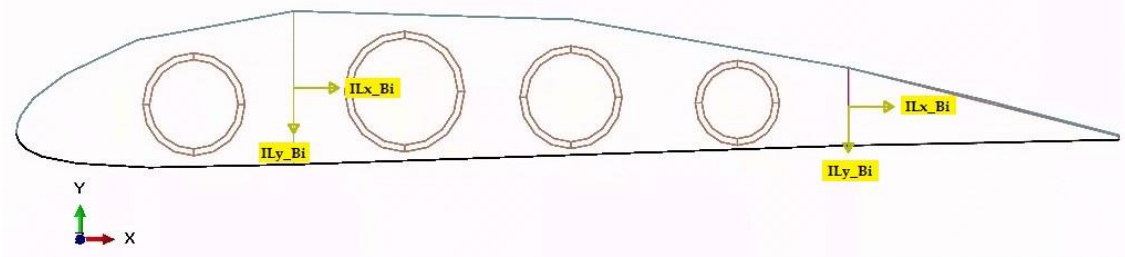

Figure 144 - Inertial load applied in each rib to the finite element model.

The distribution within the bay "k" is represented in Figure 145. It is important to note that the ribs located at the ends of each bay have a distinct load applied, which is represented by Equation 55.

$$ILz_{tiprib} = \frac{ILz_{b\,k}}{2} + \frac{ILz_{b\,k+1}}{2} \tag{55}$$

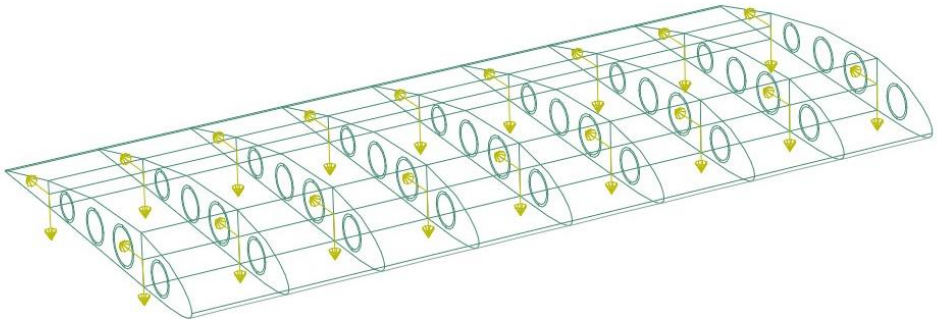

Figure 145 - Inertial loads applied to the bay "k" in finite element model.

6.2.6 Mesh Convergence

A mesh convergence analysis was conducted to determine the minimum number of elements required for the analysis, ensuring an optimal computational cost. The convergence analysis focused on stress values σ_{11} and σ_{22}, as well as the Tsai-Hill failure index, specifically in the element sets where relevant information will be obtained during post-processing.

Figure 146 presents the graphic Tsai-Hill by number of mesh elements.

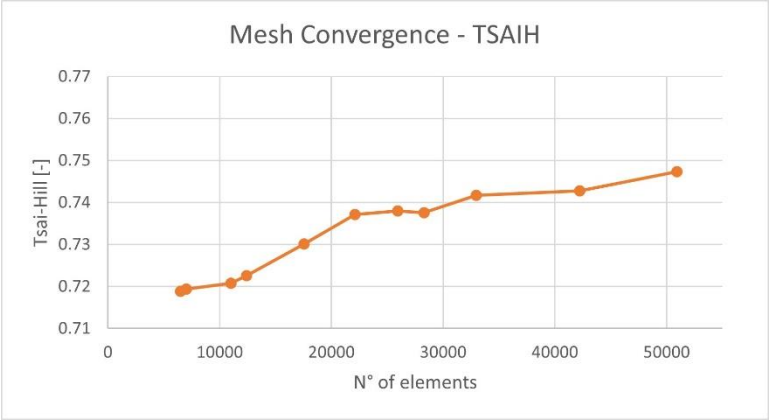

Figure 146 - Mesh convergence, Tsai-Hill vs N° of elements.

Figure 147 presents the graphic σ_{11} vs number of mesh elements.

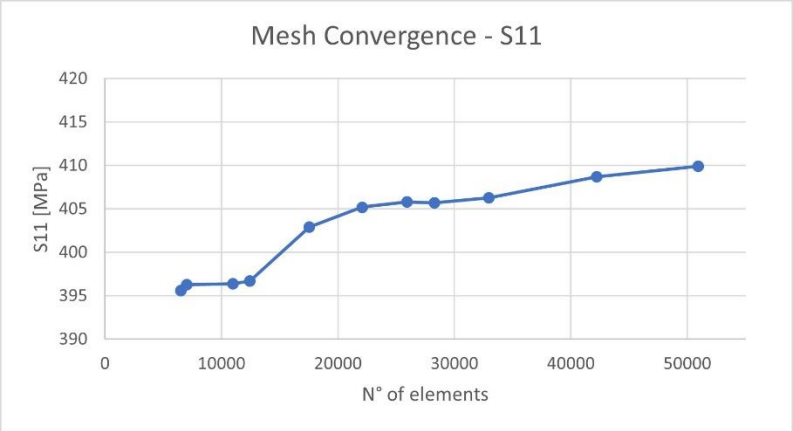

Figure 147 - Mesh convergence, S11 vs N° of elements.

Figure 148 presents the graphic σ_{22} vs number of mesh elements.

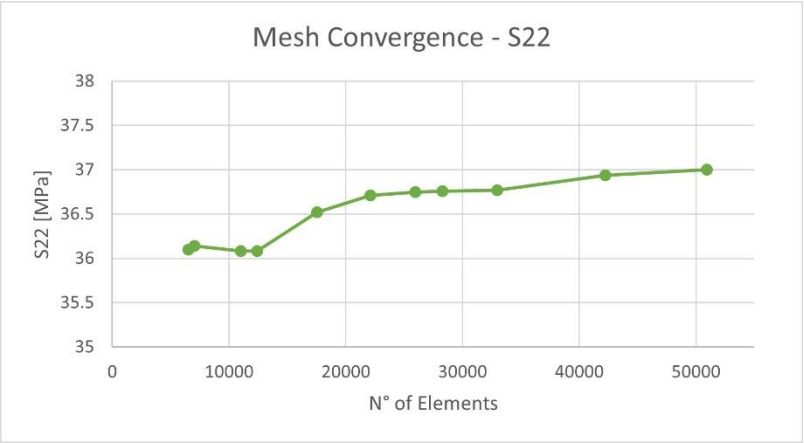

Figure 148 - Mesh convergence, S22 vs N° of elements.

From the mesh convergence analysis, it was possible to choose to proceed with a 42231 elements mesh, and its graphical representation is presented in Figure 149 and Figure 150.

Figure 149 - Finite element mesh, view 1.

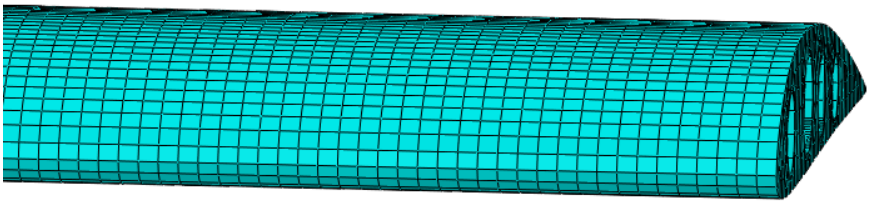

Figure 150 - Finite element mesh, view 2.

6.2.7 Deformed Shapes

To validate the functionality of the model, an analysis was conducted using a randomly assigned layup. This analysis aimed to verify the effectiveness of the boundary conditions, check for any disconnections between elements, and assess the expected displacement behavior. From Figure 151 to Figure 154, it is evident that the model is functioning well, confirming its reliability, and enabling further analysis to be carried out.

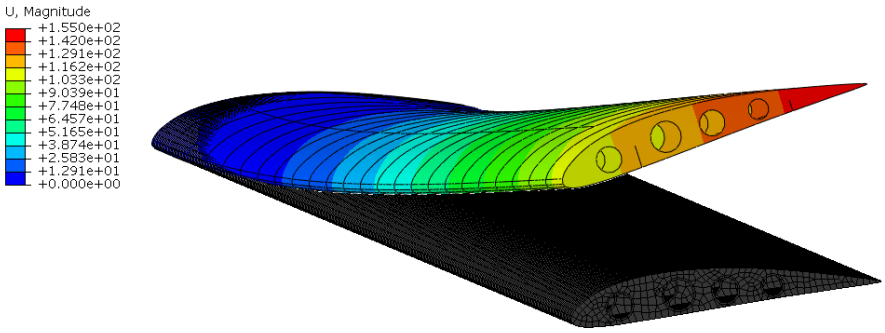

Figure 151 - Wing Finite Element Model deformed shape, view 1.

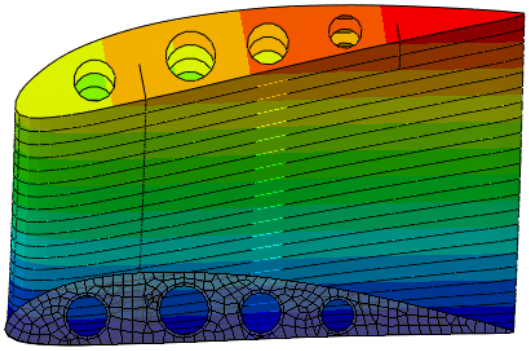

Figure 152 - Wing Finite Element Model deformed shape, view 2.

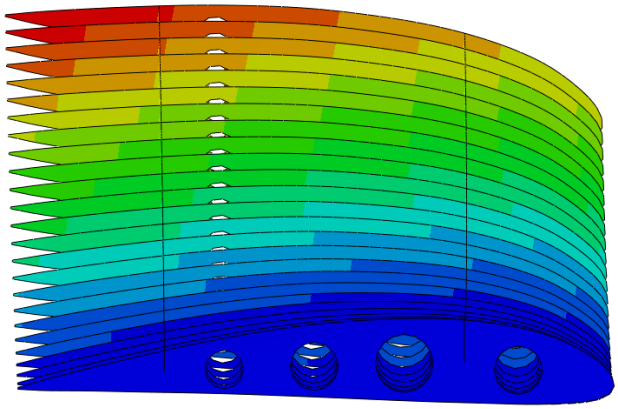

Figure 153 - Wing Finite Element Model deformed shape, view 3.

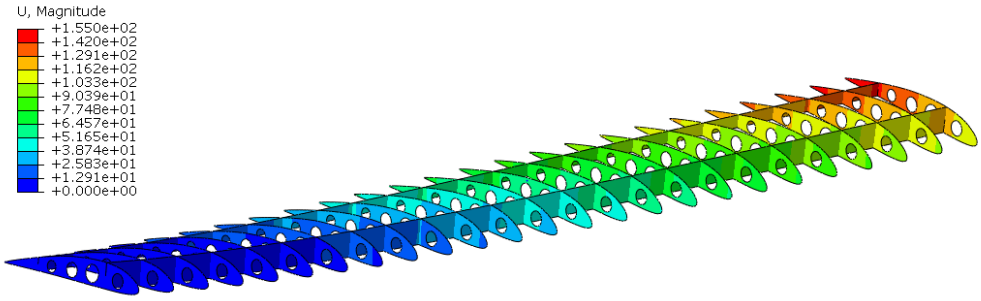

Figure 154 - Wing Finite Element Model deformed shape, view 4.

6.3 Skin - Optimization Tool application

6.3.1 Sampling

To establish an appropriate number of samples for performing regression in this type of problem, it is necessary to gradually increase the sample size and evaluate the regression performance until convergence is achieved in the results. In the case of analyzing skin, conducting approximately 2000 samples using the Latin hypercube design of experiments, while varying all 12 independent variables from 0 to 7, yielded favorable regression parameters. However, it was observed that the answers obtained were close to the lower boundaries, making it challenging for the regression to accurately distinguish failure layups. Therefore, strategic samples were gradually added in this region to improve the precision of identifying valid results. The additional samples included the following: 200 samples using the Latin Hypercube design of experiments, varying the independent variables from 0 to 2; 400 samples using the Latin Hypercube sampling from 0 to 3; and 12 samples with each section containing at least two zeros, with the variables ranging from 1 to 4. At this stage, it became evident that the answers were quasi-optimal, leading to the decision to include them in the training data to obtain a better approximation of this region. Consequently, an additional eight nearly functional solutions were incorporated. For the testing set, 200 separate iterations were performed using the Latin Hypercube design of experiments, with the 12 independent variables ranging from 0 to 7. The maximum Tsai-Hill vs the number of layers in each orientation and each section can be seen in Appendix B.

6.3.2 Gaussian Regression Parameters

For the purpose of Gaussian regression, an iterative process was carried out to determine the optimal values of the parameters Alpha, Upper boundary constant, and Lower boundary constant, with the aim of achieving the best R-squared and Average Mean Error metrics across all sections. The corresponding final metrics can be found in Table 18 and Table 19. The final parameter selections are outlined below:

- Alpha = 0.2: This specific value was chosen to introduce a higher degree of constraint on predictions, particularly when they are in close proximity to the training data. It results in predictions that tend to align closely with the values observed in the training set.
- Upper boundary constant = 6: This constant determines the upper limit of the prediction range, influencing the maximum value that predictions can attain.
- Lower boundary constant = 1e-10: This constant establishes the lower limit of the prediction range, ensuring that predictions do not approach zero.

These parameter choices were made to strike a balance between controlling the flexibility of predictions and maintaining a suitable prediction range.

Table 18 - R2, skin Gaussian regression.

#	0°-R2	90°-R2	45°-R2
Section 1	0.781	0.785	0.754
Section 2	0.886	0.885	0.863
Section 3	0.780	0.790	0.782
Section 4	0.765	0.768	0.763

Table 19 - AME, skin Gaussian Regression.

#	0°-AME	90°-AME	45°-AME
Section 1	0.142	0.138	0.116
Section 2	0.060	0.059	0.054
Section 3	0.108	0.106	0.100
Section 4	0.100	0.107	0.107

6.3.3 GA Parameters

Once the optimal parameters for Gaussian regression have been established, the next step involves iterating the parameters of the Genetic algorithm manually. The goal is to find valid results while utilizing computational resources as efficiently as possible. At this stage, it becomes possible to gain insights into the region of optimal results and make adjustments to save computational time. For instance, upon realizing that no variable would exceed 3 layers, the search range of the Genetic algorithm could be narrowed, and the number of bits reduced to 2. This adjustment in the search space, while maintaining the same population size, effectively increases the number of individuals explored without requiring additional computational resources. It should be noted that these modifications contribute to optimizing the search process and improving efficiency, allowing valid results to be obtained with reduced computational power. The final set of parameters used to achieve the optimal solution are described below:

- Population = 1000, representing the number of solutions analyzed by each iteration of the genetic algorithm.
- L = 2, representing the number of bits per variable
- Pc = 0.9, representing the fraction of population to crossover.
- Pm = 0.2, representing the fraction of population to be mutated.
- Pg = 0.2, representing the fraction of bits selected to mutation.
- Lambda = 1, representing the constraint penalty parameter.
- Consider error = True, this parameter adds the Average Mean Error obtained in the regression for each variable and adds to the failure index when evaluating the individual. This increases the failure index predicted and helps to avoid failing solutions that were not identified by the regression model.

6.4 Spars - Optimization Tool application

6.4.1 Sampling

In order to obtain the optimal solution, the decision was made to maintain the same number of 12 independent variables ranging from 0 to 7, following the approach used in the skin case. Considering the available computational time for sampling, a total of 2000 samples using the Latin hypercube design of experiments was chosen as the initial sample size. Similar to the previous case, this sample size yielded favorable regression metrics, but faced challenges in accurately predicting failures near the lower boundary condition. To address this, two additional sets of training data were included. The first set consisted of 200 samples with independent variables varying from 0 to 2, while the second set comprised 400 samples with independent variables varying from 0 to 3. The addition of these samples helped improve the

ability to identify valid solutions in proximity to the boundary. As with the previous case, the testing set was generated using a Latin hypercube design of experiments of 200 samples, encompassing the entire search space from 0 to 7 for all variables. The maximum Tsai-Hill vs the number of layers in each orientation and each section can be seen in Appendix C.

6.4.2 Gaussian Regression Parameters

For the purpose of Gaussian regression, an iterative process was carried out to determine the optimal values of the parameters Alpha, Upper boundary constant, and Lower boundary constant, with the aim of achieving the best R-squared and Average Mean Error metrics across all sections. The corresponding final metrics can be found in Table 20 and Table 21. The final parameter selections are outlined below:

- Alpha = 0.3: This specific value was chosen to introduce a higher degree of constraint on predictions, particularly when they are in close proximity to the training data. It results in predictions that tend to align closely with the values observed in the training set.
- Upper boundary constant = 4:
- Lower boundary constant = 1e-10:

These parameter choices were made to strike a balance between controlling the flexibility of predictions and maintaining a suitable prediction range.

Table 20 - R2, spars Gaussian regression.

#	0°-R2	90°-R2	45°-R2
Section 1	0.847	0.981	0.958
Section 2	0.963	0.968	0.959
Section 3	0.805	0.748	0.795
Section 4	0.860	0.826	0.876

Table 21 - AME, spars Gaussian regression.

#	0°-AME	90°-AME	45°-AME
Section 1	0.010	0.008	0.010
Section 2	0.008	0.015	0.015
Section 3	0.097	0.090	0.081
Section 4	0.062	0.060	0.048

6.4.4 GA Parameters

Similar to the previous case, during the process of finding optimal parameters to reduce computational time for optimization, it was observed that no variable would exceed 3 layers. Consequently, the search range of the Genetic algorithm could be narrowed, and the number of bits reduced to 2. This adjustment allowed for a more efficient exploration of the solution space. Additionally, further analysis revealed that after reducing the search space, maintaining the same population size as before would effectively increase the exploration capacity of the Genetic algorithm without requiring additional computational resources. The final set of parameters used to achieve the optimal solution are as follows:

- Population = 800, representing the number of solutions analyzed by each iteration of the genetic algorithm.
- L = 2, representing the number of bits per variable
- Pc = 0.9, representing the fraction of population to crossover.
- Pm = 0.2, representing the fraction of population to be mutated.
- Pg = 0.2, representing the fraction of bits selected to mutation.
- Lambda = 1, representing the constraint penalty parameter.
- Consider error = True. In this specific case the error was considered negative, which means that the Average Mean Error obtained in the regression for each variable is subtracted to the failure index when evaluating the individual. This reduces the failure index predicted.

6.5 Ribs - Optimization Tool application

6.5.1 Mesh refinement

The mesh generated for the finite model was optimized to study the skin and spars effectively, but it was found to be inadequate for studying the ribs. It is known that weight alleviation holes in the ribs can lead to stress concentrations in those regions. Consequently, it becomes important to refine the mesh specifically in those areas. To address this requirement, a structured mesh refinement was implemented in the designated region, consisting of approximately 120 mesh elements per hole. This refinement was aimed at capturing the detailed behavior and stress distribution in these rib regions. It is possible to visualize the described mesh in Figure 155 and Figure 156, which illustrate the improved mesh quality and resolution in that specific area.

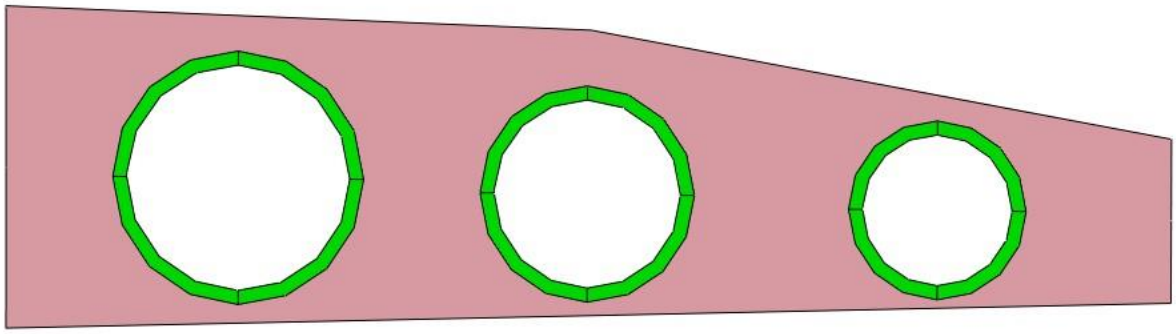

Figure 155 - Ribs, structured mesh around the holes.

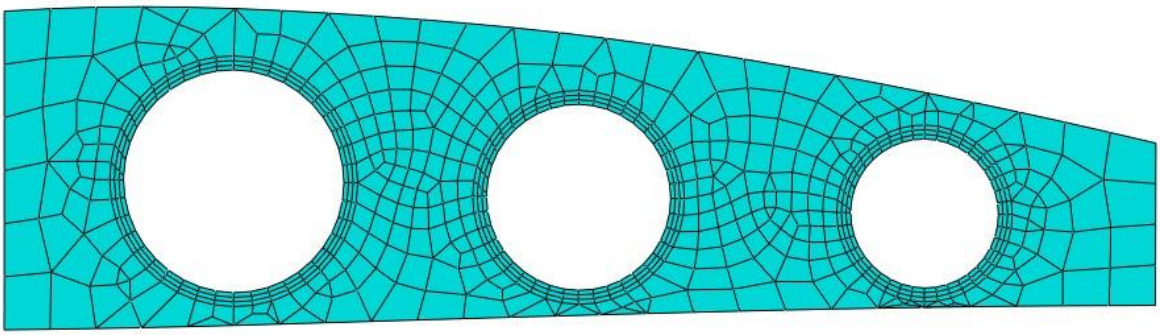

Figure 156 - Ribs mesh refinement

6.5.2 Sampling

Taking into account the insights gained from the previous cases, a preliminary manual study was conducted to determine the number of layers required to prevent failure in the composite layup. This study revealed that a genetic algorithm varying from 0 to 3 would be sufficient to obtain valid solutions. However, to achieve satisfactory results in the upper boundary region, a Latin hypercube design of experiments including six independent variables with 5 levels each, ranging from 0 to 4 was chosen. When considering the number of samples and balancing computational costs while aiming for a good regression performance, it was decided to maintain the training set size at 2000 samples. Despite the reduction in the number of independent variables, this choice was made to ensure an adequate representation of the problem space. Additionally, another independent Latin hypercube design set of 200 samples was generated for the testing set, providing a separate dataset to evaluate the performance of the regression model. The maximum Tsai-Hill vs the number of layers in each orientation and each section can be seen in Appendix D.

6.5.3 Gaussian Regression Parameters

For performing the regression, a manual iterative process was carried out to determine the optimal values of the parameters Alpha, Upper boundary constant, and Lower boundary constant, with the aim of achieving the best R-squared and Average Mean Error metrics across all sections. The corresponding final metrics can be found in Table 22 and Table 23. The final parameter selections are outlined below:

- Alpha = 0.1: This specific value was chosen to introduce a higher degree of constraint on predictions, particularly when they are near the training data. It results in predictions that tend to align closely with the values observed in the training set, when in their regions.
- Upper boundary constant = 4:
- Lower boundary constant = 1e-10:

These parameter choices were made to strike a balance between controlling the flexibility of predictions and maintaining a suitable prediction range.

Table 22 - R2, ribs Gaussian regression.

#	0°-R2	90°-R2	45°-R2
Section 1	0.967	0.940	0.957
Section 2	0.851	0.895	0.877

Table 23 - AME, ribs Gaussian regression

#	0°-AME	90°-AME	45°-AME
Section 1	0.032	0.033	0.032
Section 2	0.169	0.159	0.181

6.5.4 GA Parameters

At this specific case, and thanks to the previous study of possible solutions it was possible to start with a more optimal search range of the Genetic algorithm, with the number of bits

equals to 2, since the search comes from 0 to 3. The final set of parameters used to achieve the optimal solution are as follows:

- Population = 300, representing the number of solutions analyzed by each iteration of the genetic algorithm.
- L = 2, representing the number of bits per variable
- Pc = 0.9, representing the fraction of population to crossover.
- Pm = 0.2, representing the fraction of population to be mutated.
- Pg = 0.2, representing the fraction of bits selected to mutation.
- Lambda = 1, representing the constraint penalty parameter.
- Consider error = False, it means that the evaluated value will be directly retrieved from the prediction.

6.6 Results

6.6.1 Skin

In the skin case, the Genetic Algorithm successfully converged in 33 iterations, resulting in an optimized layup configuration detailed in Table 24. Observing the optimized layup, it is possible to notice that sections 1 and 2 share layers with the same orientations, as do sections 3 and 4. Additionally, the root sections have a higher number of layers, which aligns with the expectations given their critical role in the structure. The convergence of the Genetic Algorithm indicates that the layup achieved an optimal configuration, meeting the desired criteria and design objectives.

Table 24 - Skin, optimized layup.

#	0°-Number of Plies	90°-Number of Plies	45°-Number of Plies	Total Layers
Section 1	1	0	2	10
Section 2	1	0	1	6
Section 3	0	1	2	10
Section 4	0	2	1	8

In Figure 157, the ABAQUS graphical representation displays the distribution of the maximum Tsai-Hill values for all plies, while Table 25 provides the report extracted maximum value in each ply for each section. By examining both the graphical representation and the table, it is evident that there is no failure within the optimized area of the skin. Still, some sections do exhibit values of Tsai-Hill closer to the limit when compared to others. To further validate the optimization tool applied to the wing, manual attempts were made to reduce the number of layers. However, these attempts resulted in failure indexes greater than 1, indicating composite failure. This outcome reinforces the effectiveness and reliability of the optimization tool, demonstrating its ability to find an optimal layup configuration that meets the structural requirements of the wing.

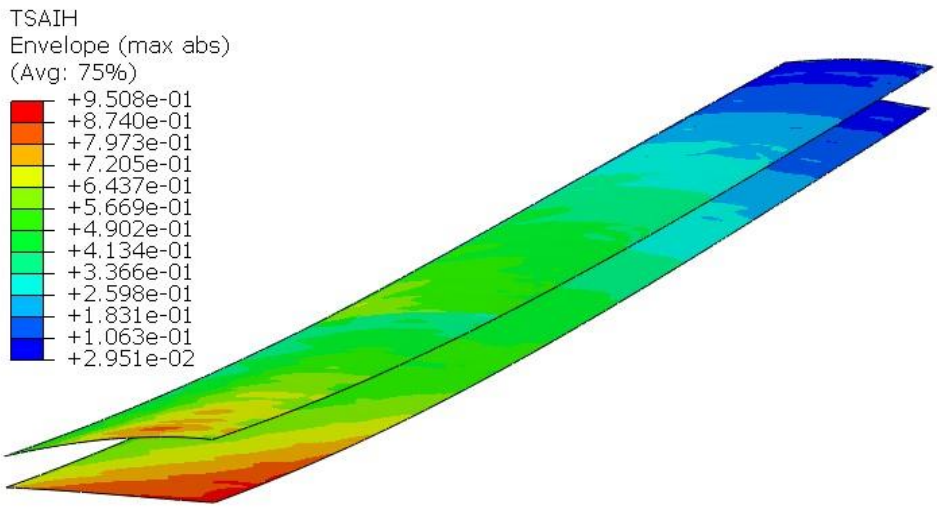

Figure 157 - Skin optimized regions

Table 25 - Skin, Tsai-Hill values with the optimized layup

#	Tsai-Hill 0°	Tsai-Hill 90°	Tsai-Hill 45°
Section 1	0.74	-	0.83
Section 2	0.66	-	0.56
Section 3	-	0.94	0.88
Section 4	-	0.58	0.58

The outcome of the skin weight optimization process yielded an optimized layup with a mass of 0.43 kg for the region under study. This optimized layup includes the total skin, encompassing the leading and trailing edges, resulting in a combined mass of 0.93 kg. It is important to emphasize that these weight values pertain to one wing side alone, as the calculation is based on a single wing of the aircraft.

6.6.2 Spars

In the spars case, the Genetic Algorithm successfully converged in 24 iterations, resulting in an optimized layup configuration detailed in Table 26. Similar to the previous case, the optimized layup shows that sections 1 and 2 share layers with the same orientations, as do sections 3 and 4. However, an interesting observation is that the main spar sections have a lower number of layers, contrary to expectations. This finding suggests that this load case, with its high pitching moment, is more critical for the secondary spar than for the main spar. This underscores the importance of conducting further analyses for multiple load cases in the V-n diagram. Additionally, it is important to highlight that although the layups have been optimized, the presented configurations have an unusually low number of layers, making their implementation in real applications challenging. This outcome arises due to the optimization order and may indicate a possible over-defined skin. To address this issue, it is possible to restart the analysis with the new final configurations iteratively until achieve convergence of results. If the layup still contains a low number of layers, there are two potential strategies: first, consider restarting the analysis by incorporating AIREX as a core material for a sandwich structure, or secondly, intentionally increase the number of layers in the layup. These steps will help refine the layup configuration to ensure both optimal performance and practical feasibility in real-world applications.

Table 26 - Spars, optimized layup.

#	0°- Number of Plies	90°- Number of Plies	45°- Number of Plies	Total Layers
Section 1	1	0	0	2
Section 2	1	0	0	2
Section 3	0	0	1	4
Section 4	0	0	1	4

Figure 158 presents the ABAQUS graphical representation displays the distribution of the maximum Tsai-Hill values for all plies, while Table 27 presents the report extracted maximum value in each ply for each section. From that it is possible to verify that there is no failure within the studied regions of the spars. In contrast to the previous case, the optimized layup for this scenario represents the minimum configuration, with 1 layer in symmetry for the first two sections and 1 layer of ±45-degrees in the 3rd and 4th sections. Due to this minimal layup, the only possible validation for the optimization was to attempt changing the orientation of the last two sections to 0 or 90 degrees. This change would potentially result in less weight, but the analysis revealed failure indexes greater than 1, indicating composite failure. his outcome reinforces the validity of the optimized results, as it demonstrates that the current layup configuration represents the most weight-optimized solution that still ensures structural integrity and performance requirements are met.

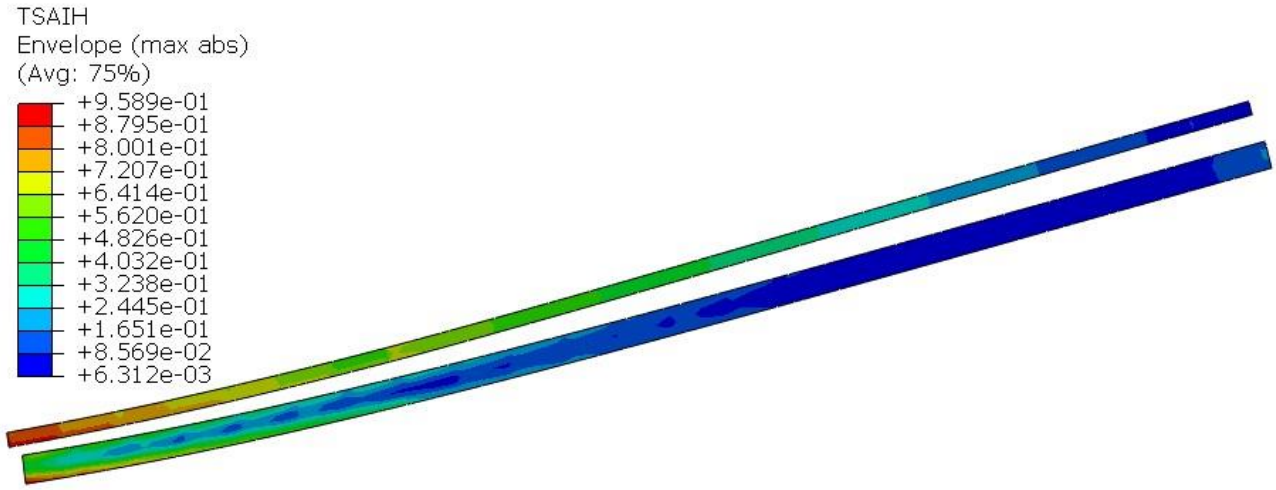

Figure 158 - Spars optimized regions.

Table 27 - Skin, Tsai-Hill values with the optimized layup.

#	Tsai-Hill 0°	Tsai-Hill 90°	Tsai-Hill 45°
Section 1	0.62	-	-
Section 2	0.26	-	-
Section 3	-	-	0.91
Section 4	-	-	0.65

The outcome of the spars weight optimization process yielded an optimized layup with a mass of 0.03 kg for the region under study. And both complete spars resulted in a combined mass of 0.032 kg. It is important to emphasize that these weight values pertain to one wing side

alone, as the calculation is based on a single wing of the aircraft. Still, it is crucial to acknowledge that the excessively low weight of the optimized layup may be attributed to an over defined skin configuration. This situation can be addressed by either changing the order of the structural elements' optimization, predefining an even more conservative spars when performing the optimization of the skin or by iteratively repeating the optimization process.

6.6.3 Ribs

In the ribs case, the Genetic Algorithm successfully converged in 8 iterations, resulting in an optimized layup configuration detailed in Table 28. It is worth recalling that this case, different from the previous, has only two different sections subjected to optimization. And it is interesting to observe that the tip panel section has a lower number of layers, contrary to expectations. This occurrence again can be a result of the high moment presented by this specific load case and again shows the importance of conducting further analyses for multiple load cases in the V-n diagram.

Table 28 - Ribs, optimized layup.

#	0°-Number of Plies	90°-Number of Plies	45°-Number of Plies	Total Layers
Section 1	1	0	1	6
Section 2	2	0	1	8

Figure 159 and Figure 160 presents the ABAQUS graphical representation of the distribution of the maximum Tsai-Hill values for all plies, while Table 29 provides the report extracted maximum failure index value in each ply for each section. From that, it is evident that there is no failure within the optimized area of the skin. Still, this specific case, which is also the most simplified one, exhibits values of Tsai-Hill closer to the limit when compared to others, providing evidence of the optimization's efficiency. Again, manual attempts were made to reduce the number of layers and change their orientations. However, these attempts resulted in failure indexes greater than 1, indicating composite failure.

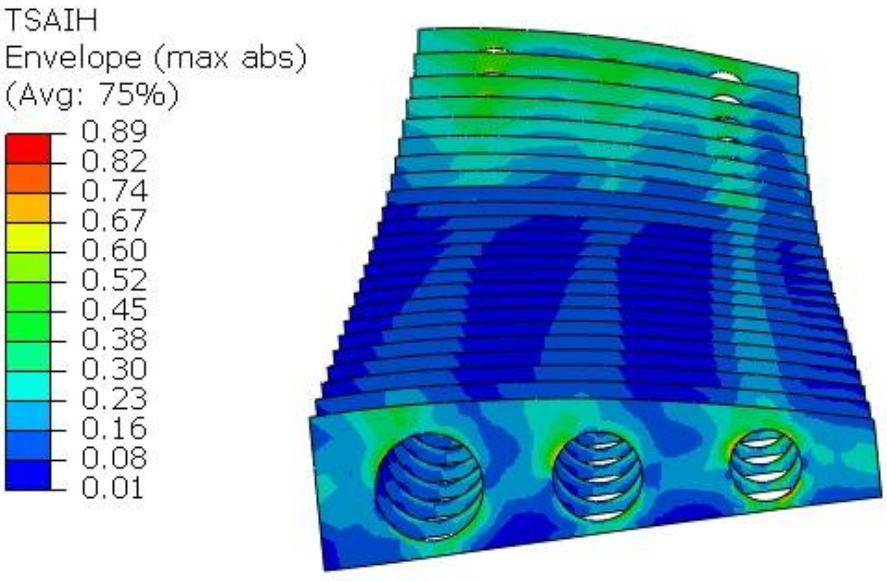

Figure 159 - Ribs optimized regions, root view.

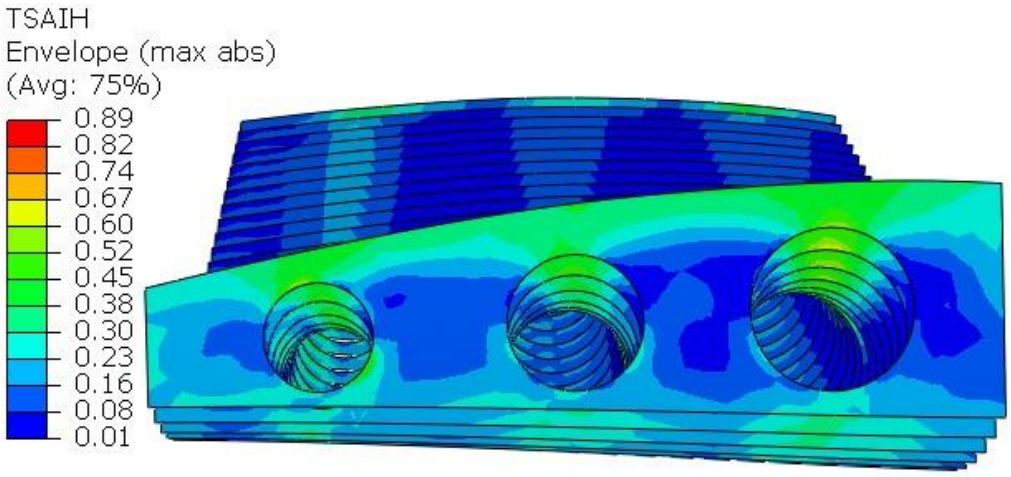

Figure 160 - Ribs optimized regions, tip view.

Table 29 - Ribs, Tsai-Hill values with the optimized layup.

#	Tsai-Hill 0°	Tsai-Hill 90°	Tsai-Hill 45°
Section 1	0.79	-	0.83
Section 2	0.82	-	0.90

The outcome of the spars weight optimization process yielded an optimized layup with a mass of 0.073 kg for the region under study. And a combined mass of 0.127 kg for all the complete ribs. It is important to highlight that these weight values pertain to one wing side alone. Still, it is worth noting that this simplification in the number of sections of optimization may represent a considerable loss in saving structural weight, and it should be considered different layups for the ribs in the tips of each panel. Another factor to be considered is that the low thickness of the ribs creates an impartibility on the manufacturing process of the wing, and it could be considered the inclusion of an AIREX core to increase the ribs thickness and consequently the gluing surface.

6.6.4 Complete Model

After completing one round of optimization for the structural elements separately, the complete wing structure was analyzed by joining all the layups obtained from the process. The results were presented after excluding the root boundary condition regions and the trailing edge, which present not realistic points of stress concentration. Figure 161 to Figure 163 show different views of the distribution of the maximum Tsai-Hill values of all layers.

From the ABAQUS extracted reports presenting values of Tsai-Hill, it was observed that the change in the layups for the structural elements analyzed separately did not cause failure of the previous structural elements in the optimization order. The occurrence of failure was the expected behavior, and the solution would be to carry out new rounds of optimization, fixing the new layups until convergence in results is achieved. However, in this specific case, that did not happen, and it can be attributed either to a good initial guess of the fixed assumed layups throughout the optimization process or to the conservative error adopted in the regression. This suggests that the flaw in performing precise predictions in the regression models could be used as an advantage when the error is known and controlled.

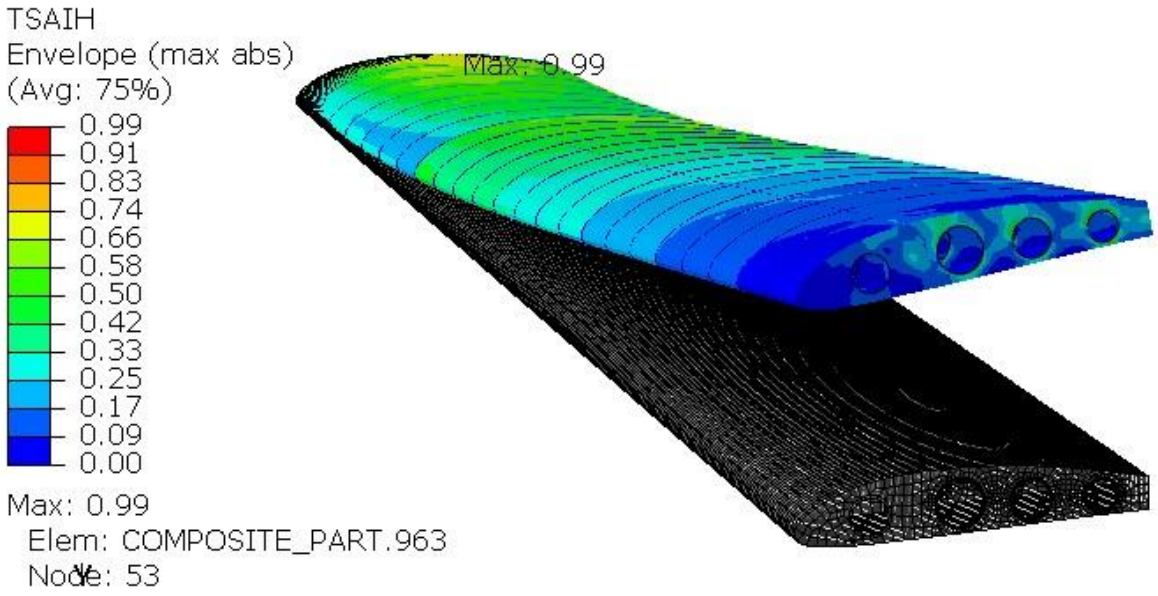

Figure 161 - Tsai-Hill, final optimized wing for the chosen load case. Tip view.

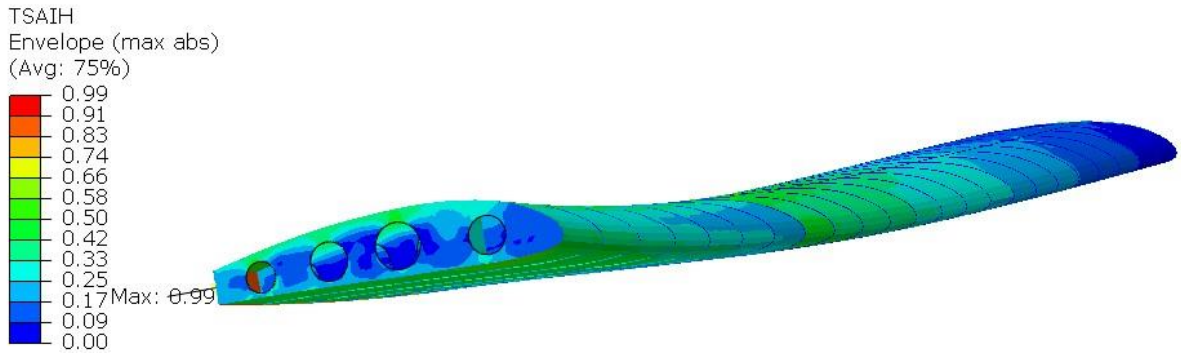

Figure 162 - Tsai-Hill, final optimized wing for the chosen load case. Root view.

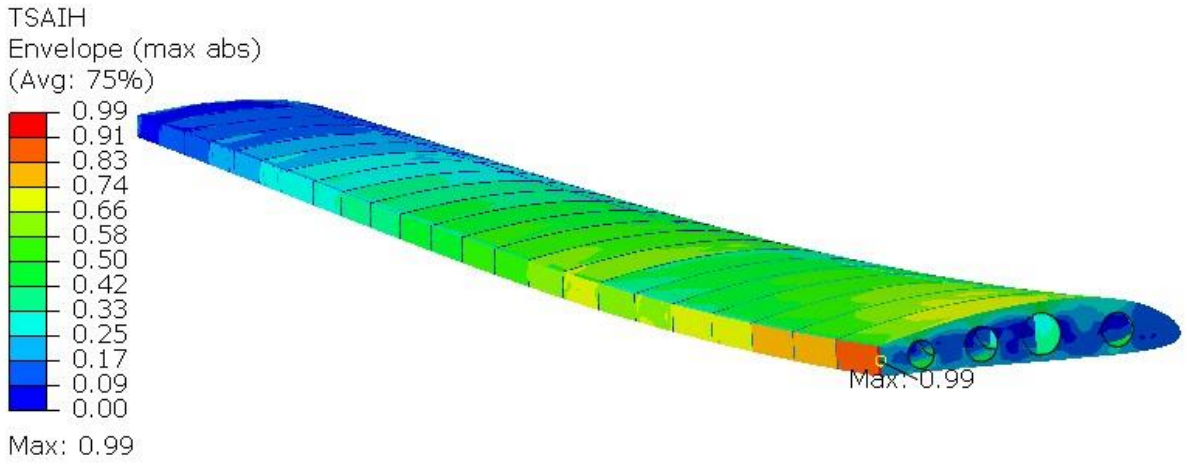

Figure 163 - Tsai-Hill, final optimized wing for the chosen load case. Back view.

Despite not being any optimization constraint, it is possible to present Figure 164 that shows the maximum vertical displacement of the wing tip with the final layup for this case. The maximum displacement was 0.2 m, representing around 13% of the semi-span. It is important to note that there were no stiffness constraint considerations for this optimization process, but it would be interesting to include them for the actual application of the wing.

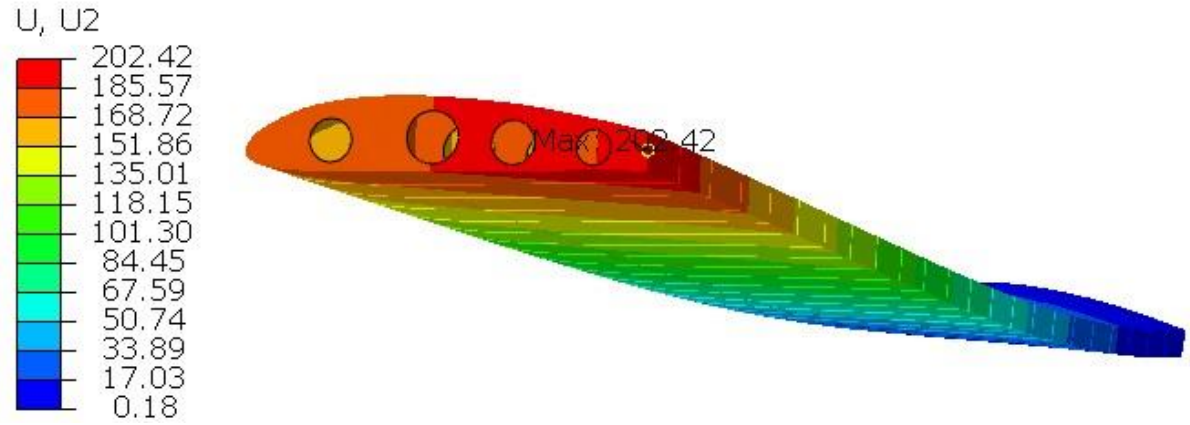

Figure 164 - Deformed Shape U2, final optimized wing for the chosen load case

Finally, it is possible to present the total weight of the optimized wing for the specific load case. For the one described iteration, it was possible to find a mass of 0.55 kg when not considering the leading and trailing edges, as well as the first bay. However, when considering the whole structure, where the layup of the leading and trailing edges is over-defined since it was considered the same as their skin region, it was possible to find a total mass of 1.09 kg for the semi-span of the wing. This means that the total mass of the CFRP wing structure would be around 2.18 kg. This value represents 9% of the maximum takeoff weight of the airplane and 18.5% of the considered structural weight. According to historical data, normally the wing represents around 20% of the structural weight, which can indicate that the wing for this specific load case is optimized.

Another interesting comparison is to take the total mass of the First aircraft (prototype), which is around 9 kg, and the total measured wing mass, which is 2.54 kg. From that, it is possible to see that despite the second aircraft having around 270% of the weight of the first prototype, with the optimization tool, it has the potential to optimize its wing resulting in a 14% lighter structure when compared to the first wing, even with the major increment of weight. It is worth saying that both wings have the same dimensions. It is important to recall that the obtained final weight for the studied wing structure is the result of one optimization iteration and of one load case. It means that for proceeding with its manufacturing it would be necessary to iterate the described process and to analyze several other load cases.

7. Conclusions and Future Work

This work was conducted in the context of the development of a fixed-wing UAV to be used for medical supplements delivery in remote areas of Asia, especially in the mountain regions of Nepal, where the terrain access is complicated and can even take several days. The medical UAV is one of the humanitarian projects from SYSTEC Lab, C2SR Lab of the Electrical Engineering Department of FEUP, whose head is professor António Pedro Rodrigues Aguiar. In addition, it is possible to highlight that the focus of this work was the development and applicability of a computational tool capable of optimizing the wing composite structure of the Medical UAV with customizable constraints, allowing the structural weight reduction and consequently having an increased performance or payload weight for completing the assigned task more effectively.

This work started by successfully developing a first aircraft prototype, which included the full sizing, design, manufacturing, and test flight of the mentioned aircraft, helping to validate methodologies and allowing to retrieve information for the improvement of the next model. It is also important to recall that one of the main objectives of the mentioned prototype is to retrieve real flight logs from the flight in the real design environment which will allow an even more optimized final product.

After the completion of the phase of the flight tests of the First Aircraft Prototype, the project evolved to the sizing of the expected final product, which was not the focus of this work, however, plays an important hole to proceed with the structural development of its wing. After this step, it was possible to obtain the shape of the wing of the 24 kg MTOW airplane in which 5 kg will be used as payload. From here and understanding the importance of an optimized weight structure, it started the development of the optimization tool.

The custom optimization tool aimed to minimize the weight of the composite material wing, incorporating a Genetic Algorithm for optimization and interfacing with the finite element software ABAQUS to establish a surrogate model. This surrogate model acted as a constraint based on the Tsai-Hill failure index. The development of the surrogate model involved a Design of Experiments (DoE) using the Latin Hypercube Sampling (LHS) technique to generate well-defined samples for training a regression model using the scikit-learn Python library's Gaussian regression. In summary, the optimization tool generated samples using LHS, trained the regression model, and evaluated the Tsai-Hill failure index for each individual in the genetic algorithm's population through the regression model. This approach proved effective, particularly for a lower number of independent sections and variables. Therefore, when applying the tool to the new wing structure, the analysis was conducted separately for each type of structural element, aiming to minimize the number of independent variables.

The optimization process began after arbitrary fixing the wing’s topology and choosing CFRP as the material to be used. Also, it was necessary to pre-define the possible orientations of the fibers being chosen in the four classical orientations (0°, 90°, 45°, and -45°). Still, it is worth mentioning that for manufacturing constraints, as the First Aircraft (prototype), it was chosen to proceed with two different types of panels: the central panel of 1 meter and two panels of 1 meter each. This assumption also allowed to simplify the number of optimization sections and reduce the independent variables. By considering four different sections of skin, four independent sections including both spars, and two independent sections including the ribs optimized separately, it was possible to obtain a failure-free, 2.16 kg, optimized wing for the single load case, representing a critical point on the V-n diagram.

For future work and to finalize the wing analysis for manufacturing, it is essential to evaluate multiple load cases represented by different points on the V-n diagram. Additionally, it is necessary to include aerodynamic constraints on the structural analysis to avoid undesired phenomena when flying. Beyond that, the optimization tool being applied separately for each

group of structural elements forces it to become an iterative process. This means that the same process would need to be repeated until achieving convergence of results and a potentially improved balance in the thickness of the structural elements. The presented results indicate that the optimal spars have small thickness, which could be a sign of over defined skins. This occurrence could be minimized by repeating the optimization process iteratively and by the implementation of sandwich structures with AIREX as core material.

An additional avenue to explore involves leveraging greater computational power to optimize all structural elements simultaneously, supported by an increased number of samples for the regression and employing a more powerful regression method like Neural Networks. The increased computational capability enables the creation of more detailed and optimized models, with reduced simplifications.

Finally, it is of paramount importance to highlight the vast potential of exploring various failure criteria, as doing so allows for a significantly more comprehensive analysis of composite failure. This expanded examination provides a deeper understanding of the structural integrity and failure mechanisms within the composite materials, contributing to enhanced safety and design considerations.

In conclusion, this work has successfully achieved its objectives, including the complete development of the First Aircraft prototype and the successful development and application of a highly customizable computational tool to minimize the structural weight of the wing for the Medical UAV, optimizing both number of plies and their orientation. The result of this work is an optimized structure that is predicted to be within or even below the minimum structural weight projected by historical data for the studied load case. Furthermore, the customizable nature of the computational tool allows for easy adaptation to accommodate different constraints and explore more advanced computational resources. This flexibility opens the door for further optimization efforts, enabling the exploration of various scenarios and design considerations, ultimately contributing to the development of even more efficient and lightweight structures for future UAV projects.

8. References

[1] C. C. Bitter *et al.*, "A Short-Term Medical Mission in Rural Nepal: Chief Complaints, Medications Dispensed, and Unmet Health Needs," *Cureus*, vol. 13, no. 6, Jun. 2021, doi: 10.7759/CUREUS.15427.

[2] "Nepal: Poor in remote villages struggle to access health care - Nepal | ReliefWeb." https://reliefweb.int/report/nepal/nepal-poor-remote-villages-struggle-access-health-care (accessed Sep. 22, 2023).

[3] "Atendimento médico a índios na Amazônia representa desafio para aviação - Força Aérea Brasileira." https://www.fab.mil.br/noticias/mostra/22658/ (accessed Sep. 22, 2023).

[4] M. Mayes and A. Uk, "Drone Implementation: Regulatory Barrier CORE View metadata, citation and similar papers at core", Accessed: Sep. 22, 2023. [Online]. Available: https://digitalcommons.georgiasouthern.edu/honors-theses

[5] M. A. Boon, A. P. Drijfhout, and S. Tesfamichael, "Comparison of a fixed-wing and multi-rotor UAV for environmental mapping applications: A case study," *International Archives of the Photogrammetry, Remote Sensing and Spatial Information Sciences - ISPRS Archives*, vol. 42, no. 2W6, pp. 47–54, Aug. 2017, doi: 10.5194/ISPRS-ARCHIVES-XLII-2-W6-47-2017.

[6] A. Misra *et al.*, "A Review on Vertical Take-Off and Landing (VTOL) Tilt-Rotor and Tilt Wing Unmanned Aerial Vehicles (UAVs)," 2022, doi: 10.1155/2022/1803638.

[7] "Zipline Instant Delivery & Logistics." https://www.flyzipline.com/ (accessed Jun. 15, 2023).

[8] "Matternet." https://mttr.net/ (accessed Jun. 15, 2023).

[9] "Wing." https://wing.com/ (accessed Jun. 15, 2023).

[10] "G-1 MKII – Vayuaerospace." https://vayuaerospace.com/g-1-mkii (accessed Jun. 15, 2023).

[11] Michael C.Y. Niu, *Composite Airframe Structures*, 1° Edition. 1992.

[12] Federal Aviation Administration, "FAR 25: Airworthiness Standards: Transport Category Airplanes."

[13] European Aviation Safety Agency, "CS-25: Certification specifications for large aeroplanes."

[14] Z. Zhuguo, Z. Yingchun, and O. Xupo, "Study on key certification issues of composite airframe structures for commercial transport airplane," *Procedia Eng*, vol. 17, pp. 247–257, 2011, doi: 10.1016/J.PROENG.2011.10.026.

[15] Federal Aviation Administration, "Advisory Circular (AC) 20-107B Composite Aircraft Structures." 2010.

[16] Adrian P. Mouritz, *Introduction to aerospace materials*. Woodhead Publishing Limited, 2012.

[17] G. Kretsis, "A review of the tensile, compressive, flexural and shear properties of hybrid fibre-reinforced plastics," *Composites*, vol. 18, no. 1, pp. 13–23, 1987, doi: 10.1016/0010-4361(87)90003-6.

[18] M. Raci Aydin, V. Acar, F. Cakir, Ö. Gündoğdu, and H. Akbulut, "Comparative dynamic analysis of carbon, aramid and glass fiber reinforced interply and intraply hybrid

composites," *Compos Struct*, vol. 291, p. 115595, Jul. 2022, doi: 10.1016/J.COMPSTRUCT.2022.115595.

[19] J. K. ; M. D. B. ; M. Y. W. Kim, "Drop-weight impact damage tolerance of CFRP with rubber-modified epoxy matrix.," *Composites*, 1993.

[20] D. ; S. Y. B. Hull, "Damage mechanism charaterizatioin in composite damage tolerance investigations.," *Compos. Struct*, 1993.

[21] W. J. ; M. J. Cantwell, "The impact resistance of composite materials-a review.," *Composites*, 1991.

[22] H. T. P. K. S. O. A. W. M. Tehrania. Nekoda van de Werken, "Additively manufactured carbon fiber-reinforced composites: State of the art and perspective," *Elsevier*, 2020.

[23] D. , & C. T. W. Hull, " An Introduction to Composite Materials.," 1996.

[24] A. R. Melro, P. Camanho, A. Arteiro, G. Catalanotti, and M. Vogler, "Numerical modelling of failure in advanced composite materials," *Numerical Modelling of Failure in Advanced Composite Materials*, pp. 1–541, Aug. 2015, doi: 10.1016/C2014-0-02677-9.

[25] C. T. Sun, B. J. Quinn, and J. Tao, "COMPARATIVE EVALUATION OF FAILURE ANALYSIS METHODS FOR COMPOSITE LAMINATES 13. Type of Report and Period Covered AAR-431 Unclassified Unclassified," 1996, Accessed: Sep. 22, 2023. [Online]. Available: www.tc.faa.gov/its/act141/reportpage.html

[26] Daniel et al., *Engineering Mechanics of Composite Materials*. New York, 1994.

[27] Tsai, *Theory of Composites Design*. Stanford, 2008.

[28] M. P. , S. O. Bendsøe, *Topology optimization: Theory, methods and applications*, 2nd ed. 2003.

[29] R. Le Riche and R. T. Haftka, "Improved genetic algorithm for minimum thickness composite laminate design," *Composites Engineering*, vol. 5, no. 2, pp. 143–161, Jan. 1995, doi: 10.1016/0961-9526(95)90710-S.

[30] R. H. Lopez, M. A. Luersen, and E. S. Cursi, "Optimization of laminated composites considering different failure criteria," *Compos B Eng*, vol. 40, no. 8, pp. 731–740, Dec. 2009, doi: 10.1016/J.COMPOSITESB.2009.05.007.

[31] T. S. B. B. Mark Tuttle, "SIMPLIFYING CERTIFICATION OF DISCONTINUOUS COMPOSITE MATERIAL FORMS FOR PRIMARY AIRCRAFT STRUCTURES".

[32] Michael Smith, "ABAQUS/Standard User's Manual," vol. 2020. Dassault Systemes Simulia Corp, United states, 2020.

[33] "Abaqus - Mechanical and Civil Engineering Simulation." https://www.3ds.com/products-services/simulia/products/abaqus/ (accessed Jun. 19, 2023).

[34] "Isight & SIMULIA Execution Engine | Dassault Systèmes®." https://www.3ds.com/products-services/simulia/products/isight-simulia-execution-engine/ (accessed Jun. 19, 2023).

[35] "Optimization-enabled Structural Analysis | Altair OptiStruct." https://altair.com/optistruct (accessed Jun. 19, 2023).

[36] "Ansys optiSLang | Process Integration & Design Optimization Software." https://www.ansys.com/products/connect/ansys-optislang (accessed Jun. 19, 2023).

[37] X. S. Yang, *Nature-Inspired Optimization Algorithms*. Elsevier, 2020. doi: 10.1016/B978-0-12-821986-7.00002-0.

[38] C. A. C. António, "Otimização de Sistemas em Engenharia - Fundamentos e algoritmos para o projeto ótimo," 2020, Accessed: Jun. 13, 2023. [Online]. Available: https://repositorio-aberto.up.pt/handle/10216/132356

[39] J. H. Holland, "Adaptation in Natural and Artificial Systems: An Introductory Analysis with Applications to Biology, Control, and Artificial Intelligence," *Adaptation in Natural and Artificial Systems*, Jan. 1992, doi: 10.7551/MITPRESS/1090.001.0001.

[40] A. I. J. Forrester, A. Sóbester, and A. J. Keane, "Engineering Design via Surrogate Modelling," *Engineering Design via Surrogate Modelling*, Jul. 2008, doi: 10.1002/9780470770801.

[41] L. W. Condra, "Reliability Improvement with Design of Experiment," *Reliability Improvement with Design of Experiments*, May 2018, doi: 10.1201/9781482270846.

[42] J. Antoy, "Design of Experiments for Engineers and Scientists: Second Edition," *Design of Experiments for Engineers and Scientists: Second Edition*, pp. 1–672, 2014, doi: 10.1016/C2012-0-03558-2.

[43] F. A. C. Viana, "A Tutorial on Latin Hypercube Design of Experiments," *Qual Reliab Eng Int*, vol. 32, no. 5, pp. 1975–1985, Jul. 2016, doi: 10.1002/QRE.1924.

[44] L. Pronzato and W. G. Müller, "Design of computer experiments: space filling and beyond," *Statistics and Computing 2011 22:3*, vol. 22, no. 3, pp. 681–701, Apr. 2011, doi: 10.1007/S11222-011-9242-3.

[45] D. Freedman, "Statistical models : theory and practice," p. 442, 2009, Accessed: Jun. 20, 2023. [Online]. Available: https://www.worldcat.org/title/586163317

[46] G. James, D. Witten, T. Hastie, and R. Tibshirani, "An Introduction to Statistical Learning," 2021, doi: 10.1007/978-1-0716-1418-1.

[47] "scikit-learn: machine learning in Python — scikit-learn 1.2.2 documentation." https://scikit-learn.org/stable/ (accessed Jun. 20, 2023).

[48] "1.1. Linear Models — scikit-learn 1.2.2 documentation." https://scikit-learn.org/stable/modules/linear_model.html# (accessed Jun. 20, 2023).

[49] "sklearn.preprocessing.PolynomialFeatures — scikit-learn 1.2.2 documentation." https://scikit-learn.org/stable/modules/generated/sklearn.preprocessing.PolynomialFeatures.html (accessed Jun. 20, 2023).

[50] "sklearn.linear_model.Lasso — scikit-learn 1.2.2 documentation." https://scikit-learn.org/stable/modules/generated/sklearn.linear_model.Lasso.html (accessed Jun. 20, 2023).

[51] J. Friedman, T. Hastie, and R. Tibshirani, "Regularization Paths for Generalized Linear Models via Coordinate Descent," *J Stat Softw*, vol. 33, no. 1, pp. 1–22, Feb. 2010, doi: 10.18637/JSS.V033.I01.

[52] S. J. Kim, K. Koh, M. Lustig, S. Boyd, and D. Gorinevsky, "An interior-point method for large-scale ℓ1-regularized least squares," *IEEE Journal on Selected Topics in Signal Processing*, vol. 1, no. 4, pp. 606–617, Dec. 2007, doi: 10.1109/JSTSP.2007.910971.

[53] R. M. Rifkin and R. A. Lippert, "massachusetts institute of technology Notes on Regularized Least Squares," 2007, Accessed: Jun. 20, 2023. [Online]. Available: www.csail.mit.edu

[54] "sklearn.linear_model.Ridge — scikit-learn 1.2.2 documentation." https://scikit-learn.org/stable/modules/generated/sklearn.linear_model.Ridge.html (accessed Jun. 20, 2023).

[55] "sklearn.linear_model.ElasticNet — scikit-learn 1.2.2 documentation." https://scikit-learn.org/stable/modules/generated/sklearn.linear_model.ElasticNet.html (accessed Jun. 20, 2023).

[56] "1.7. Gaussian Processes — scikit-learn 1.2.2 documentation." https://scikit-learn.org/stable/modules/gaussian_process.html#gaussian-process-regression-gpr (accessed Jun. 20, 2023).

[57] C. E. Rasmussen and C. K. I. Williams, "Gaussian Processes for Machine Learning", Accessed: Jun. 20, 2023. [Online]. Available: www.GaussianProcess.org/gpml

[58] "Kernel Cookbook." https://www.cs.toronto.edu/~duvenaud/cookbook/ (accessed Jun. 20, 2023).

[59] D. Raymer, "Aircraft Design: A Conceptual Approach, Sixth Edition," *Aircraft Design: A Conceptual Approach, Sixth Edition*, Sep. 2018, doi: 10.2514/4.104909.

[60] "Airfoil plotter (goe398-il)." http://airfoiltools.com/plotter/index (accessed Jun. 20, 2023).

[61] "Easy Access Rules for Very Light Aeroplanes (CS-VLA) - initial issue & amendment 1 - Available in pdf & XML format | EASA." https://www.easa.europa.eu/en/document-library/easy-access-rules/easy-access-rules-very-light-aeroplanes-cs-vla (accessed Jun. 20, 2023).

[62] "GOE 398 AIRFOIL (goe398-il)." http://airfoiltools.com/airfoil/details?airfoil=goe398-il (accessed Jun. 20, 2023).

[63] "doepy · PyPI." https://pypi.org/project/doepy/ (accessed Jun. 20, 2023).

[64] "sqlite3 — DB-API 2.0 interface for SQLite databases — Python 3.11.4 documentation." https://docs.python.org/3/library/sqlite3.html (accessed Jun. 20, 2023).

[65] Dr. Volnei Tita, Dr. Frederico Danzi, and Dr. Carolina Silva, " Booklet 1_Fundaments_2021_v3_Type 2." 2021.

[66] Dr. Volnei Tita, Dr. Carolina Silva, and Dr. Federico Danzi, "Booklet V8 - Wing-box structural analysis."

[67] Prof. Dr. Volnei Tita, "Loading in aeronautical structures: Fundaments. Lecture Slides of Fundaments of Aeronautical Design. FEUP."

[68] "T-MOTOR Store-Official Store for T-motor drone motor,ESC,Propeller." https://store.tmotor.com/ (accessed Jun. 27, 2023).

APPENDIX A: Wingbox testing model – maximum Tsai-Hill value vs number of layers for each ply orientation in each section.

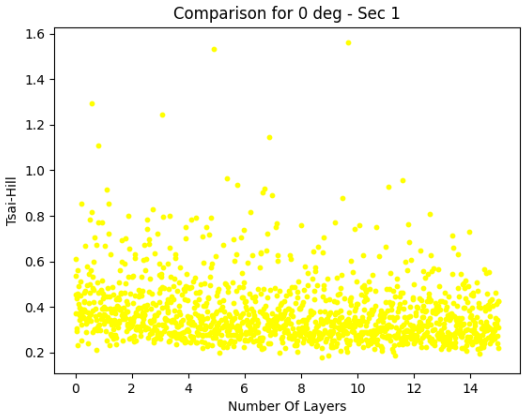

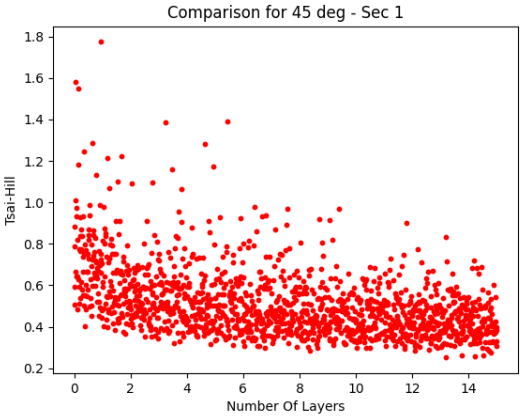

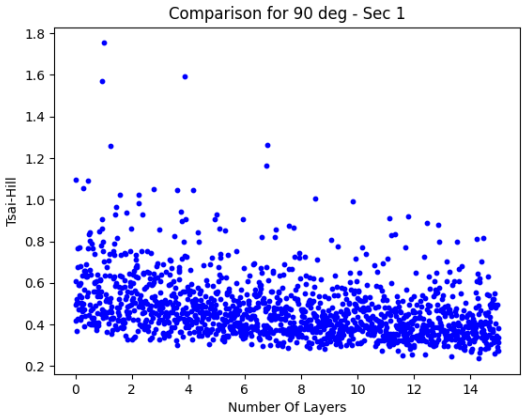

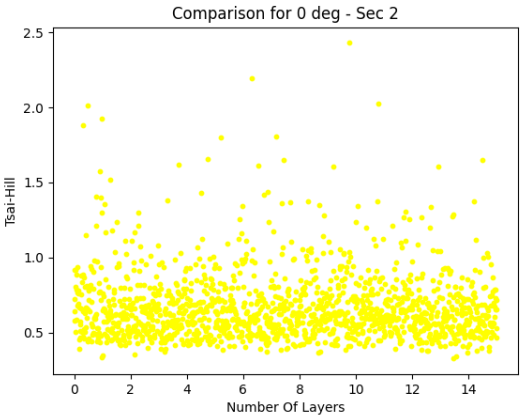

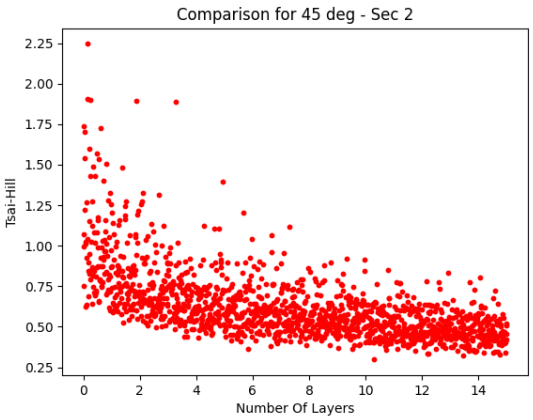

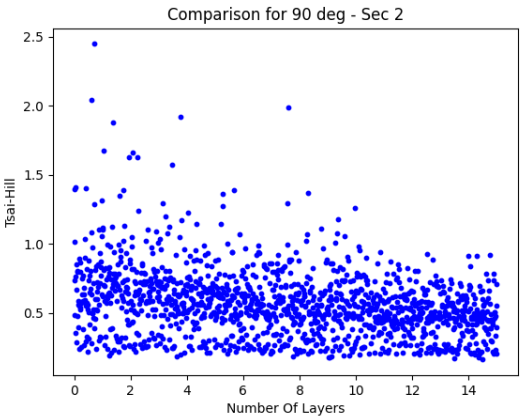

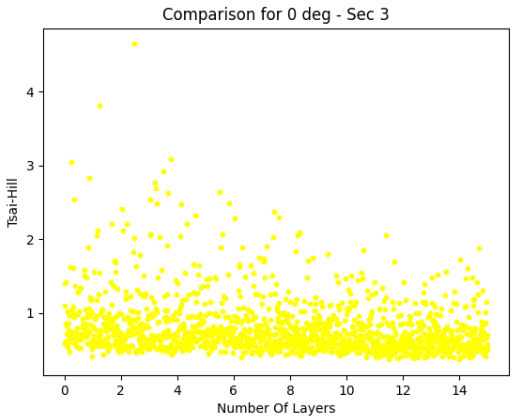

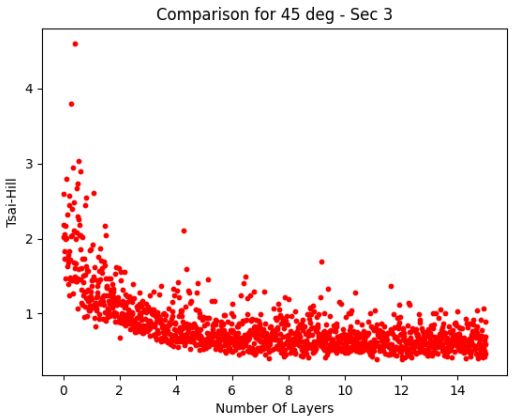

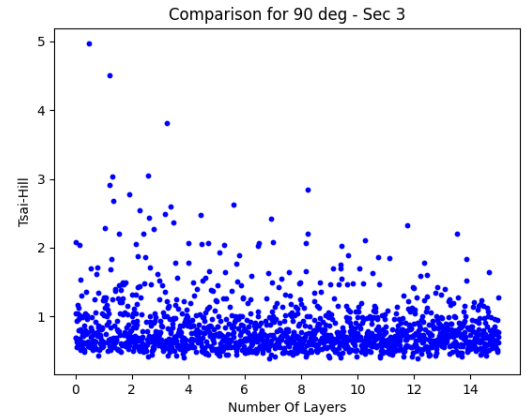
Comparison for 90 deg - Sec 3
Tsai-Hill
Number Of Layers

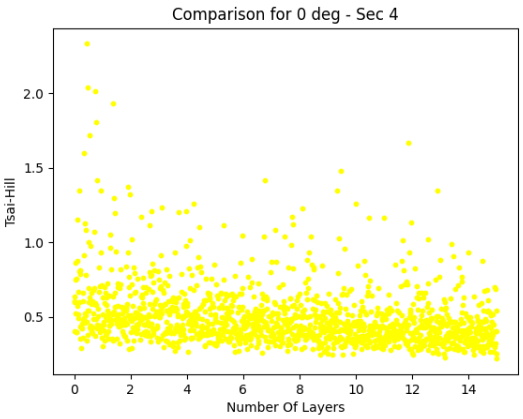
Comparison for 0 deg - Sec 4
Tsai-Hill
Number Of Layers

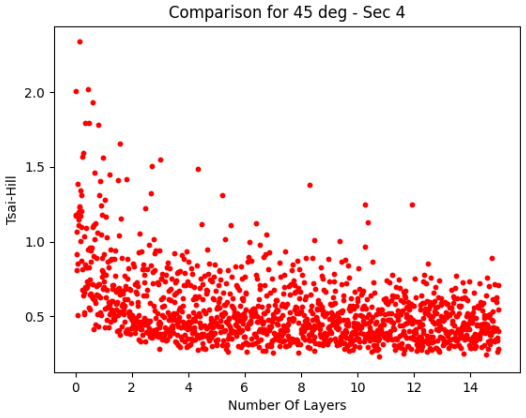
Comparison for 45 deg - Sec 4
Tsai-Hill
Number Of Layers

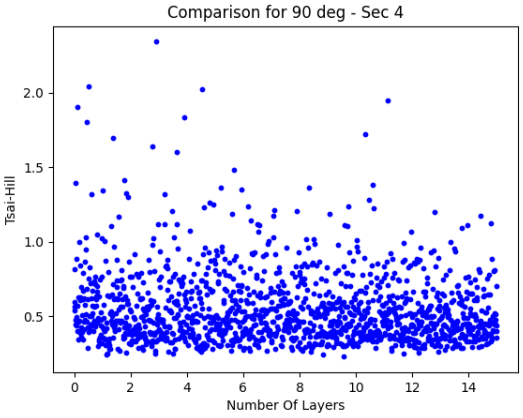
Comparison for 90 deg - Sec 4
Tsai-Hill
Number Of Layers

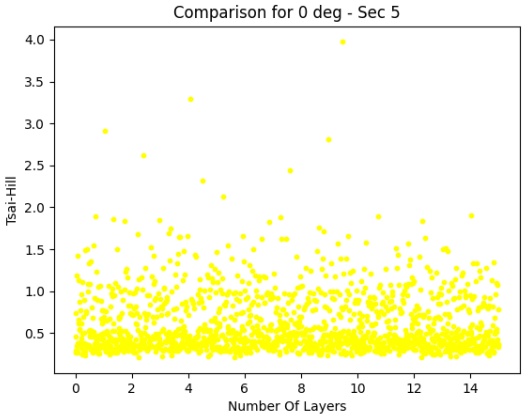
Comparison for 0 deg - Sec 5
Tsai-Hill
Number Of Layers

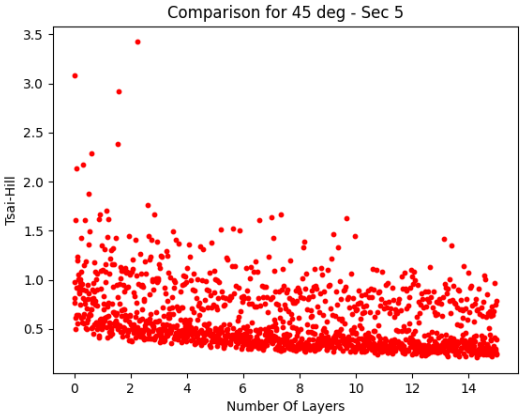
Comparison for 45 deg - Sec 5
Tsai-Hill
Number Of Layers

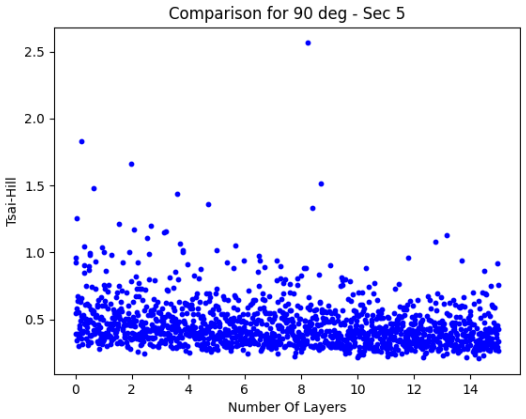
Comparison for 90 deg - Sec 5
Tsai-Hill
Number Of Layers

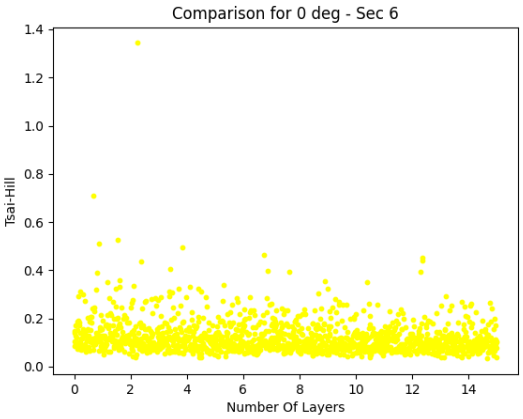
Comparison for 0 deg - Sec 6
Tsai-Hill
Number Of Layers

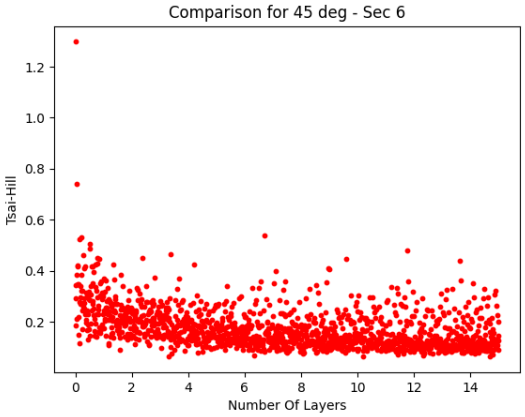
Comparison for 45 deg - Sec 6
Tsai-Hill
Number Of Layers
0.2
0.4
0.6
0.8
1.0
1.2
0
2
4
6
8
10
12
14

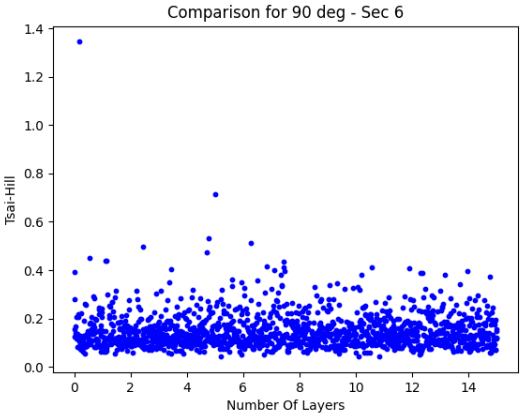
Comparison for 90 deg - Sec 6
Tsai-Hill
Number Of Layers
0.0
0.2
0.4
0.6
0.8
1.0
1.2
1.4
0
2
4
6
8
10
12
14

APPENDIX B: Skin – maximum Tsai-Hill value vs number of layers for each ply orientation in each section.

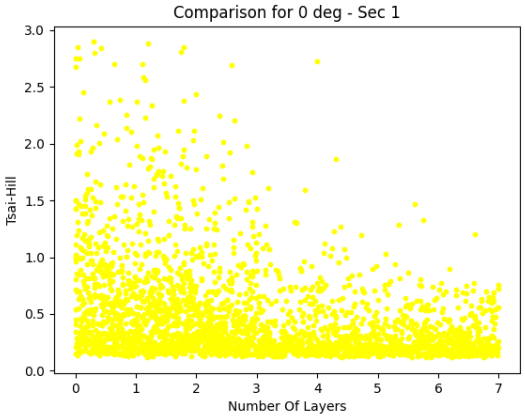

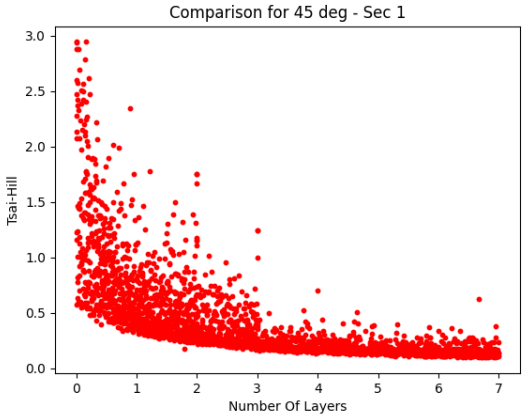

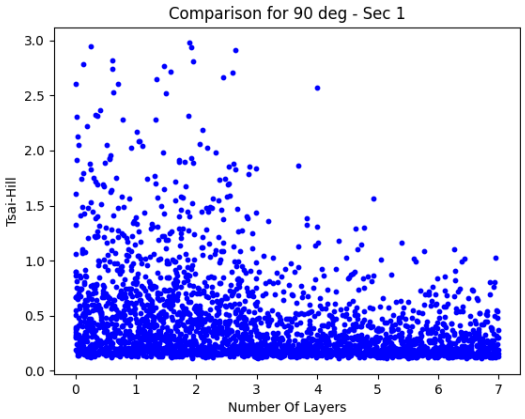

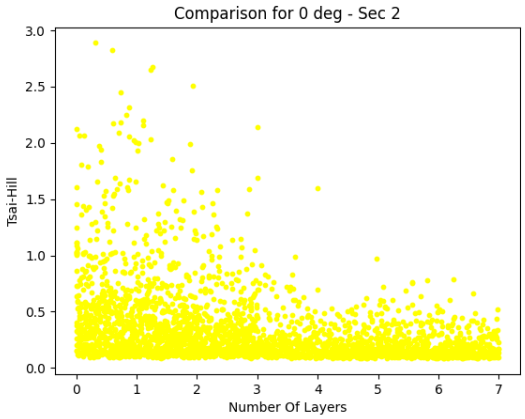

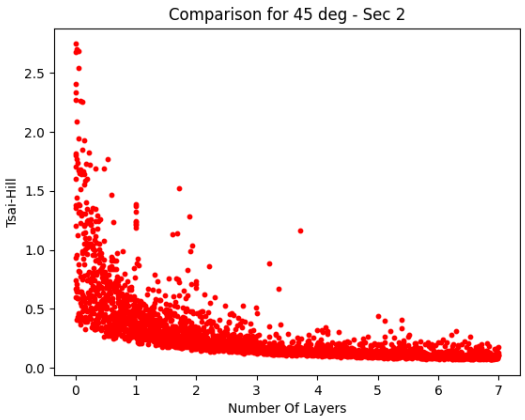

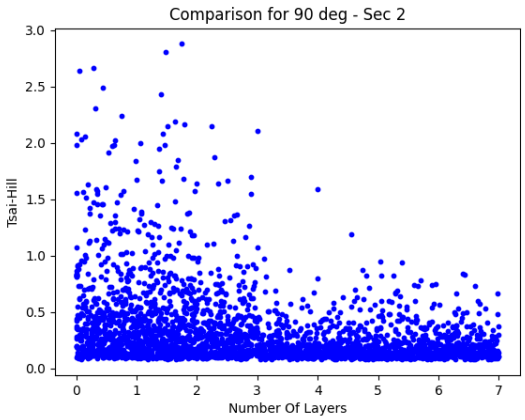

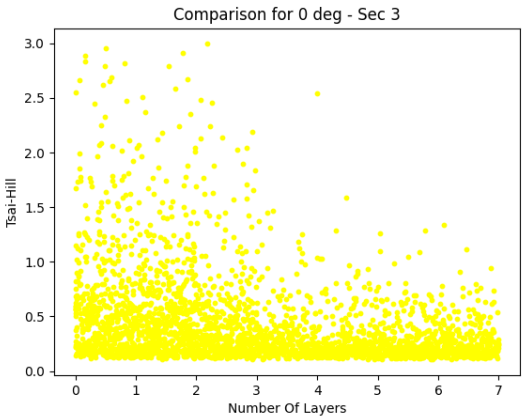

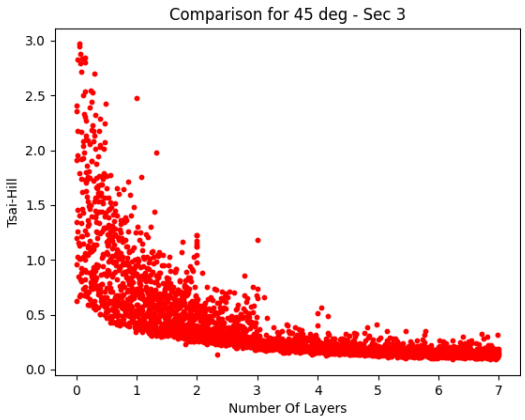

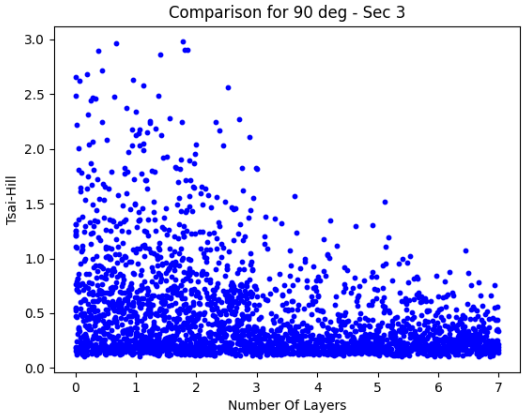
Comparison for 90 deg - Sec 3
Tsai-Hill
Number Of Layers

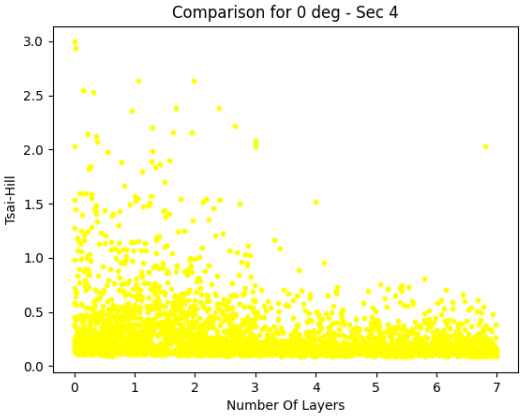
Comparison for 0 deg - Sec 4
Tsai-Hill
Number Of Layers

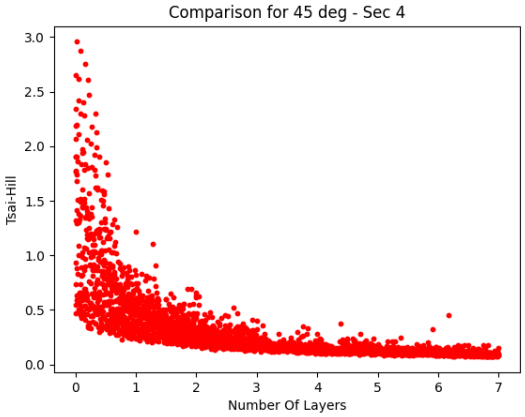
Comparison for 45 deg - Sec 4
Tsai-Hill
Number Of Layers

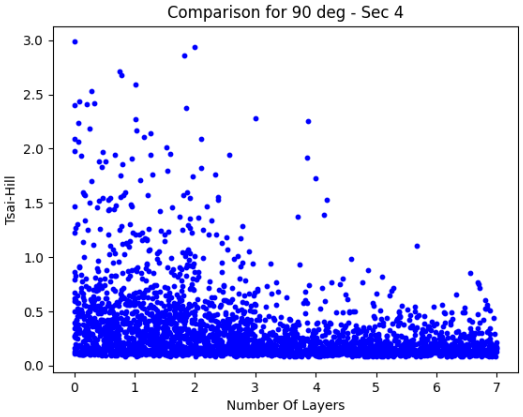
Comparison for 90 deg - Sec 4
Tsai-Hill
Number Of Layers

APPENDIX C: Spars – maximum Tsai-Hill value vs number of layers for each ply orientation in each section.

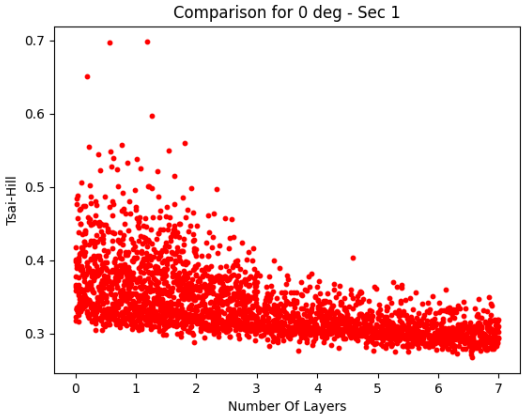

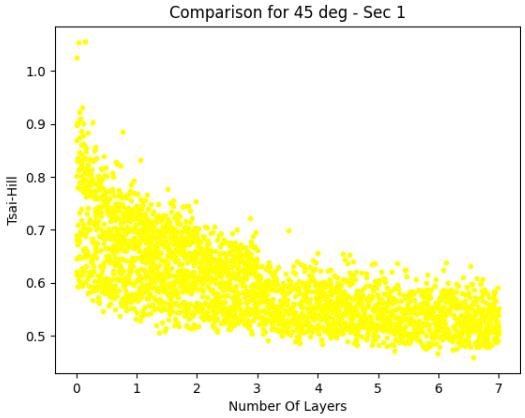

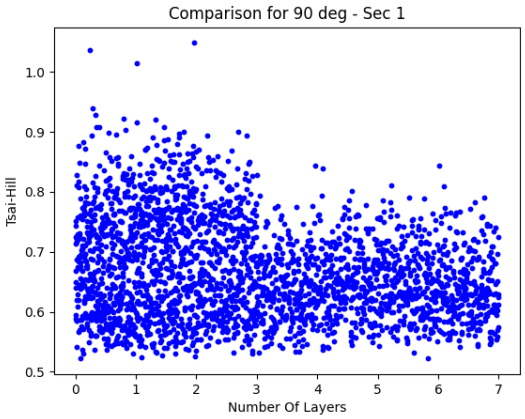

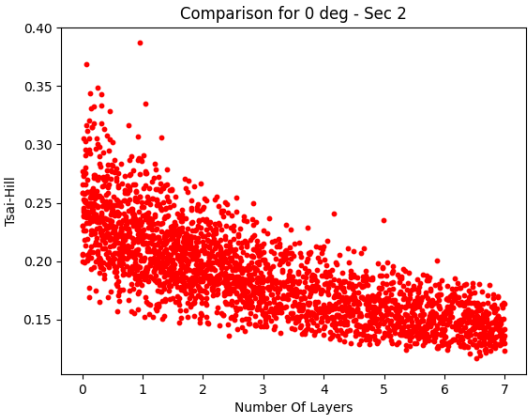

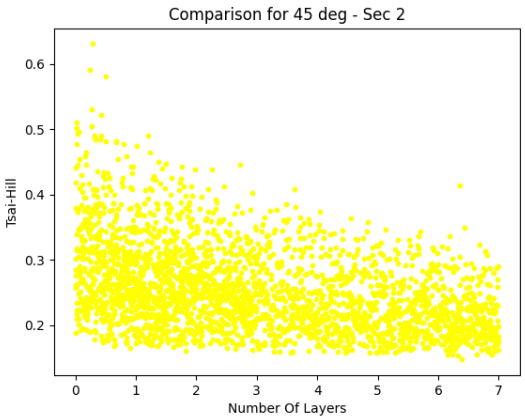

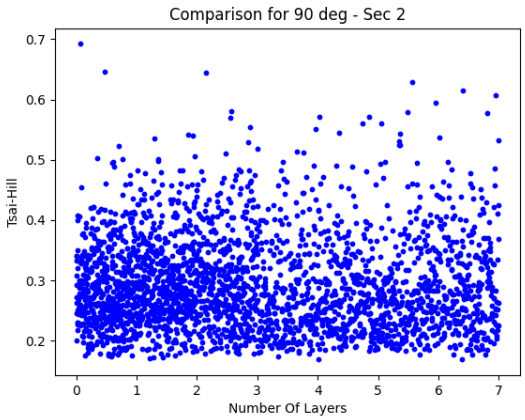

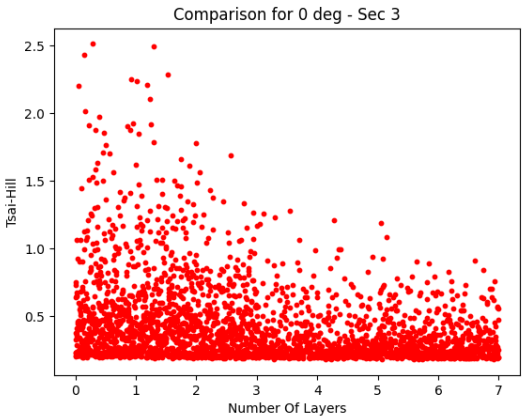

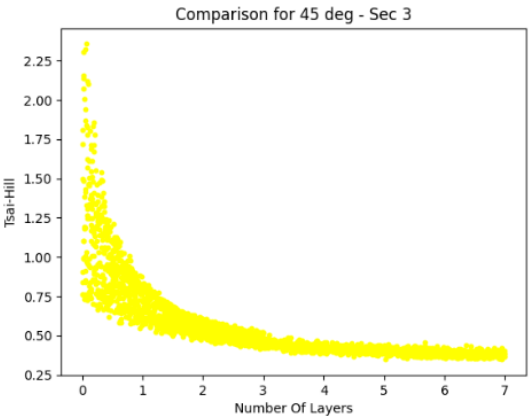

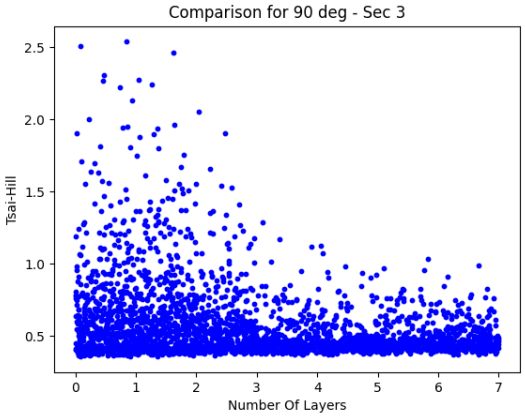
Comparison for 90 deg - Sec 3
Tsai-Hill
Number Of Layers

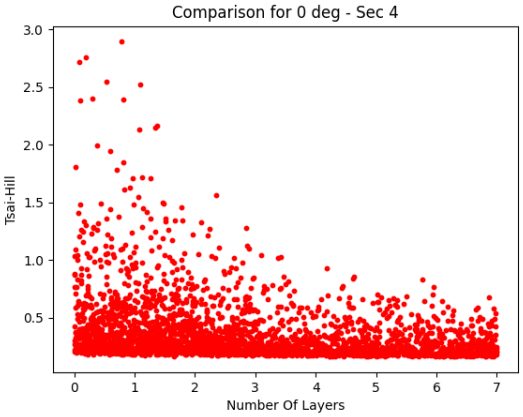
Comparison for 0 deg - Sec 4
Tsai-Hill
Number Of Layers

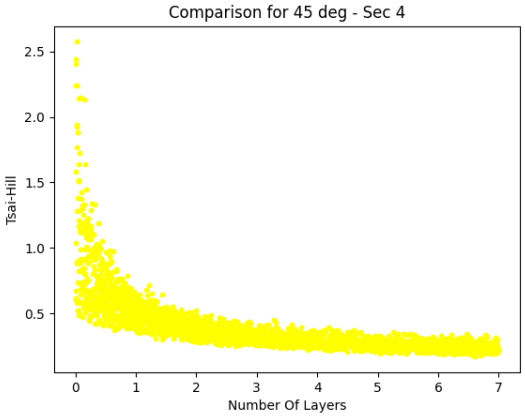
Comparison for 45 deg - Sec 4
Tsai-Hill
Number Of Layers

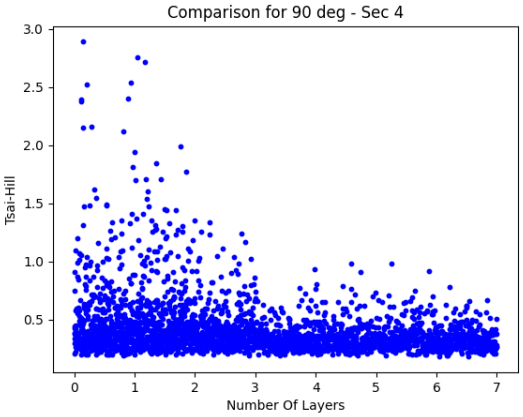
Comparison for 90 deg - Sec 4
Tsai-Hill
Number Of Layers

APPENDIX D: Ribs – maximum Tsai-Hill value vs number of layers for each ply orientation in each section.